„Plasmoscope: Automated Spectroscopy of Single Nanoparticles”

Dissertation
zur Erlangung des Grades
„Doktor der Naturwissenschaften”
im Promotionsfach Chemie

Am Fachbereich Chemie, Pharmazie und Geowissenschaften der
Johannes Gutenberg-Universität Mainz

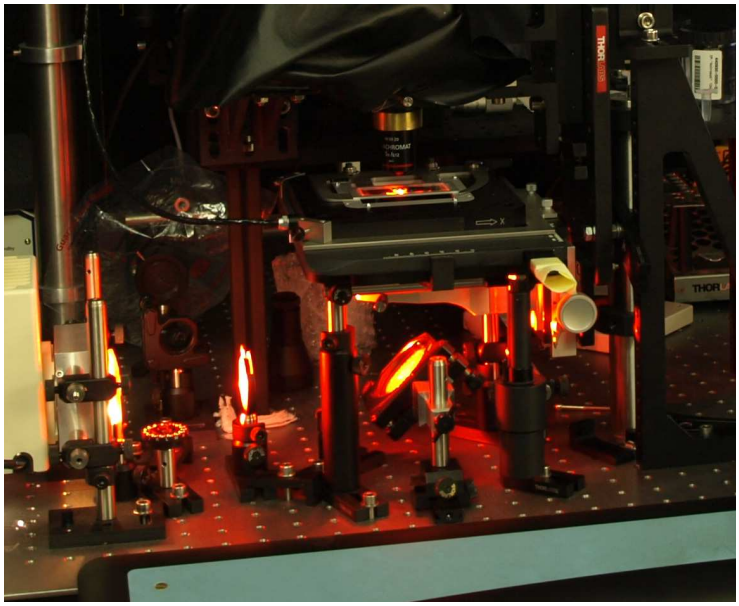

Arpad Jakab
geb. in Budapest

Mainz, 2011

Tag der mündlichen Prüfung: 26.7.2011[*]

[*] D77 Mainzer Dissertation

Only if you achieve your measurements can you measure your achievments

Scientific Publications

Most of the content of this thesis has been published in peer reviewed scientific journals:

1. *"Plasmonic focusing reduces ensemble linewidth of silver-coated gold nanorods"* Becker, J. and Zins, I. and Jakab, A. and Khalavka, Y. and Schubert, O. and Sonnichsen, C. **NANO LETTERS, 2008, 8, 1719-1723**

2. *"Tuning plasmonic proper- ties by alloying copper into gold nanorods"* Henkel, A and Jakab, A and Brunklaus, G and Soennichsen, C. **JOURNAL OF PHYSICAL CHEMISTRY C, 2009, 113, 2200-2204**

3. *"Light-Controlled One-Sided Growth of Large Plasmonic Gold Domains on Quantum Rods Observed on the Single Particle Level"* Carbone, L. and Jakab, A. and Khalavka, Y. and Sönnichsen, C. **NANO LETTERS, 2009, 9, 3710-3714**

4. *"The optimal aspect ratio of gold nanorods for plasmonic bio-sensing"* Becker, J. and Trugler, A. and Jakab, A. and Hohenester, U. and Sonnichsen, C. **PLASMONICS, 2010, 5, 161-167**

5. *"Highly Sensitive Plasmonic Silver Nanorods"* Jakab, A. and Khalavka, Y. and Becker, J. and Trugler, A. and Rosman, C and Hohenester, U. and Sonnichsen, C. **ACS NANO, 2011, under revision**

Abstract

Plasmons are the collective resonant oscillations of the conductive electrons. Excited by light, localized plasmons in single subwavelength sized nanoparticles are promising candidates for future micro-scale sensors due to the strong dependency of the resonance on externally controllable parameters like the optical properties of the surrounding medium and the electric charging of the nanoparticles themselves. The extremely high scattering efficiency of the localized plasmon makes single nanoparticles easily observable with appropriate microscopic setups.

The requirement of collecting a statistically relevant number of data points in a short time and the emerging relevance of plasmonic (especially gold) nanoparticles for medical applications called for an automatized microscope that can measure in the previously only partially accessed biological window of 650 to $900nm$. I introduce in this work the *Plasmoscope* that has been designed and built to fulfill the mentioned requirements (i) with the insertion of an adjustable vertical slit placed into the entrance plane of the spectrometer that overlaps with the image plane of the microscope and (ii) by a precision positioning stage to scan the sample through this narrow window. This idea's realization avoids optical elements that absorb in the near infra red spectrum.

Using the *Plasmoscope* I conduct a careful investigation of the plasmonic sensitivity, the resonance shift upon changing the surrounding medium of gold and silver single nanoparticles. The sensitivity is a basic measure of how well nanoparticles are able to detect smallest refractive index changes in their vicinity (like concentration variations), therefore it has an immense importance to understand what other parameters influences the sensitivity. I show that silver nanorods have a higher sensitivity than gold ones in the biological window, and that the sensitivity increases with thicknesses. I provide a theoretical discussion of the underlying physical processes, identify the material parameters that impact the sensitivity, and derive mathematical expressions to model the system. In another approach I present experimental data supporting the theoretical finding that gold nanorods with an length/width (aspect) ratio of 3 to 4 yield the best performance for sensing schemes that are based on the figure of merit (sensitivity divided by linewidth). Reliable sensor applications require a robust reversibility, restoring the initial conditions after sensing must result in shift back to the initial resonance position which is investigated on gold and silver nanorods.

The plasmon resonance wavelength depends also on intrinsic material parameters: electron density, background polarizability, and the relaxation time. Based on my experimental results I show that copper-gold alloy nanorods possess a red shifted resonance compared to pure gold nanorods of similar shape and size, furthermore, that the linewidth varies with the alloy's stoichiometric composition. The dependency of linewidth on material composition is also examined on silver coated and uncoated gold nanorods.

Semiconductor nanoparticles are candidates for efficient photovoltaic devices. The energy conversion requires charge separation that is measured experimentally with the *Plasmoscope*. I measure the growth dynamics by time tracing the scattered intensity of the light-driven growth of the gold domain on single semiconductor nanoparticles in a gold ion solution.

Contents

List of Tables

List of Figures

Chapter 1

Introduction

Nanotechnology and nanoscience has become the buzzword among the scientific community as well as among the high-tech crowd. What is about it that makes it so popular? Driven by the miniaturization and integration of electronic circuits for the computer industry, in the in the 90's of the last century engineers and scientists were forced to enter a lengthscale of material engineering where classical description of matter intermixed with quantum mechanics. Moving to smaller and smaller scales, new physical effects emerge that may open up new routes towards future technological or biological applications. Electronic and consequently optical properties may deviate if the electrons are squeezed into a volume that approaches or falls below a critical measurement like exciton Bohr-radius in semiconductors or the penetration depth of light in noble metals. Mechanical and chemical properties can be considerably altered with nano-scaled structuring of materials due to increased surface to volume ratio. The route of reaching nano-scaled materials through miniaturization is called the *top-down* concept. The opposite route, the so called *bottom-up* concept attempts to assemble single molecules into a supramolecular entity in a defined manner. Prominent methods of nanostructure fabrication applying the top-down concept are various forms of optical or electron beam lithography, template based sputtering technologies, ion beam milling or atomic force microscope assisted assembly, whereas examples for the bottom-up concept are DNA-engineering, molecular self assembly or porous template methods. The emerging discipline of nanotechnology has brought physics, chemistry and biology together and offers a number of opportunities in (bio)sensing, medicine, integrated circuits, data storage, or energy conversion both from fundamental and application point of view .

Since the most direct and highly evolved sensory link between human and environment is the visual perception, attempts of optical observation of nanoscaled objects were and still are a major area of research. Furthermore, most of the natural phenomena that originate from nanoscaled structures have optical character (photonic bandgap materials, antireflection coatings, photochemistry, marking or signal processing). The first scientific observation of plasmonic nanoparticles was reported by Faraday in the middle of the 19th century who observed various colors of gold colloids. Mie's and Gans' theoretical works explained these colors by relating the colors to resonant oscillations of the conduction electrons. Zsigmondy succeded to observe *single gold nanoparticles* in the beginning of the 20th century with his so called *ultra microscope* that utilized the extraordinary strong scattering of these tiny objects to visualize them. Since then a vast amount of technological and scientific advances have led to ever smarter ways to overcome the resolution limitations.

In this work I will present advances on the field of plasmonic and semiconductor nanoparticles. The growth of the field *Plasmonics* is reflected in the major boost that was given to this field by the development of surface plasmon resonance based sensors in the early '90-s. Plasmonic applications

received a significant role especially in the area of biodetection. Recently, metallic nanostructures drew broad attention for their ability to guide or manipulate light at the nanoscale. Raman scattering can be significantly enhanced with localized surface plasmons where advantage is being taken in converting excitation light into highly focused electromagnetic modes of radiation at so called "hot spots" of nanostructures. [Campion & Kambhampati, 1998] Other exciting milestones of plasmonic nanostructure research of the early days were the discovery of extraordinary high optical transmission through subwavelength metal apertures [Ebbesen et al., 1998] and the suggestion by Pendry [Pendry, 2000] that plasmonic thin films can act as perfect lenses overcoming the diffraction limit.

If bulk metal and semiconductor get into contact and set under voltage bias, current rectification can be observed. The tendency of the Fermi-levels to reach equipotential causes an electronic band bending (depletion layer) that is employed for various semiconductor devices. This band bending gets an interesting twist if the size of semiconductor falls below the dimension of the depletion layer. Thanks to the electronic level quantization, low dimensional semiconductor electron systems such as nanocrystals or quantum dots have drawn much interest in the last 30 years. Since their discovery large steps have been made in chemical synthesis reducing the polydispersity and increasing shape and size control. Applications in biology as robust fluorescence markers are already common practice, but also a promising future is forecasted on the field of photovoltaic devices, light emitting diodes and quantum computing. Multicomponent nanoparticles are expected to play a significant role towards engineered functional materials. Combining semiconductor with noble metal nanoparticles could unite semiconductor bandgap engineering methods with plasmon design that could open up new routes for the optoelectronic or the photovoltaic industry.

The observation of single nanoparticles bears an exceptional experimental importance since it brings advantages in multiple areas: (1) complete elimination of the inhomogeneous spectral broadening, thus accurate observation of linewidth that is linked to intrinsic material parameters (2) direct observation of the resonance wavelength thus additional information regarding effects that are linked to single particle resonances, (3) possibility to link spectrum and geometry using additional microscopy tools like TEM or SEM, and (4) possibility to measure polarization dependent response.

The small size of the nanoparticles poses some hurdles for the researcher to optically investigate single nanoparticles. But thanks to their efficient scattering, it is possible to observe them in an optical microscope with special illumination methods: plasmonic nanoparticles can be visualized by means of dark field illumination whereas fluorescent nanoparticles can be seen with appropriate filter sets. The most common realization of single particle microscopic systems consists of a microscope with a pinhole placed into the image plane. The single particle was manually positioned to a location that it could be imaged onto the pinhole and the spectrometer behind the pinhole detected the spectrum. The demand to improve this cumbersome and time consuming method in terms of throughput resulted in the development of a series of automatized single particle spectroscopic setups at our group: FastSPS [Becker et al., 2007] that utilized a spatially addressable liquid crystal based shutter to select single particles and measure their spectra, thus rendering the particle positioning needless. An other realization, called RotPol [Schubert et al., 2008] utilized a variable wavelength interference filter to spectrally image the sample. Both these mentioned setups have a spectral cut-off at 700 nm due to technological limitations, furthermore these devices were lacking a high enough sensitivity to observe weak signals. In this work I will introduce a new concept to automatically measure a large number of single nanoparticles and report experimental results that couldn't have been obtained with other existing setups. I named our new spectroscopic setup *Plasmoscope* in honor to its first intended purpose to measure plasmonic nanoparticles, but as it will be presented, it is also capable to measure fluorescent nanoparticles.

In Chapter 2 I will give an introduction into the topic of optical properties of metals and semi-

conductors with focus on properties that originate in nanoscaled dimensions. I will discuss aspects of the propagation of electromagnetic waves in lossy materials, introduce the complex dielectric function and Drude's concept of metallic conductivity. Certain highly conductive metals like noble metals exhibit resonant conduction electron oscillations that can couple to optical fields on the boundary between metal and dielectrics. These oscillations, called plasmons, are discussed in detail. I introduce the localized surface plasmon polaritons, or simply particle plasmons, present the basic model thereof, and following with a summary of parameters that influence the spectral characteristics of plasmons. Then I shift to semiconductor nanoparticles as a prominent group of fluorescent quantum emitters. The small size of these nanoparticles results in a confinement that leads to low dimensional, as in our cases to 0 (quantum dots) or 1 (quantum rods) dimensional, electron systems. I will overview the consequences of the quantized electronic states like blinking and size dependent fluorescence spectrum. On the example of rod like semiconductor heterostructures I will explain how band alignment types can lead to electron delocalization in the conduction band. Then I will discuss the effects of the nanoscaled dimensions on the characteristics of semiconductor-metal contacts leading to Fermi-level equilibration.

In Chapter 3 I will introduce the experimental setup, the Plasmoscope, that was built to automatically measure single particle spectra. The system consisting of a micropositioning stage, a microscope, an imaging spectrometer and a cooled back illuminated CCD camera overcame limitations of previously developed systems in terms of spectral range and sensitivity. After investigating parameters that limit the resolution and contrast, I will list methods that have been invented and used to surpass these limits. Treating special aspects of single particle spectroscopy, I will elaborate the system design of the Plasmoscope. This concept is based on a scanning principle utilizing parallelization possibilities provided by an imaging spectrometer. The scanning principle allows for imaging nanoparticles onto a narrow slit at the entrance of the imaging spectrometer. Since this narrow slit does not spectrally influence the passing light, it offers the advantage to examine spectral areas where previous setups failed. A measurement-scan produces large amount of data that needs further postprocessing to extract the single particle spectrum. I will explore two methods that were developed to find single particle signals in the recorded data and introduce the spectrum extraction procedure.

Chapter 4 I will investigate how silver coating gold nanorods reduces the ensemble plasmon linewidth by changing the relation connecting particle shape and plasmon resonance wavelength. This change, my collaugues termed 'plasmonic focusing', leads to less variation of resonance wavelengths for the same particle size distribution. We also observe single particle plasmon resonance linewidths and compare the resonances at the same wavelengths, thus we will be able to understand how and why a coated particle displays a weaker damping than an uncoated at the same resonance wavelength. We attempt to entangle the contributions of single particle linewidth and plasmonic focusing for the observed ensemble linewidth changes using TEM assisted particle size distribution characterization and the particle shape and plasmon resonance relation. I will discuss in detail the surprising result that single particle plasmon resonance linewidth narrowing at a given resonance wavelength does not contribute to the ensemble linewidth narrowing due to a blue shift of the resonance of each single particle.

Since material parameters play a dominant role in defining the characteristics of plasmon resonances we submerge deeper into this subject and explore in Chapter 5 how the presence of copper in the growth solution has a pronounced effect on the spectral characteristic of the resulting nanocrystals. In contrast to spherical copper particles, our rod-shaped nanocrystals show a strong plasmon resonance and the copper content varies the plasmon resonance frequency and the plasmonic linewidth. Optical single particle plasmon-line-width observations show reduced plasmon damping at specific copper contents corresponding to stoichiometric particle compositions supporting the assumption that the DC-conductivity of the alloy influences the plasmon damping.

I also give a detailed explanation why does the more gentle slope of the real part of the dielectric function of the disordered copper-gold alloy lead to a red shift of the plasmon resonance.

Recently, plasmon resonance has been employed for optical nanoscopic sensing schemes. In Chapter 6, by means of simulations and experiments, we investigate which aspect ratio (AR) of gold nanorods is ideal for plasmonic sensing by employing various measures for 'ideal' behavior. There are several different quantities that describe the performance of a plasmonic structure for sensing applications on a single particle level – and all of them have their merits for certain applications. We will discuss the most important of them, the plasmonic sensitivity to refractive index change (shift of the plasmon resonance maximum upon surrounding refractive index change), introduce various forms of 'figures of merit' – and present their dependency on nanorods' geometry utilizing Boundary Element Method (BEM) calculations for spherically capped gold rods and experimental results obtained with the single particle dark-field scattering spectroscopy setups, Plasmoscope and FastSPS. Using the Drude model for metallic conductivity at optical frequencies and the quasi-static approximation for localized surface plasmon polaritos, I derive an expression for the sensitivity.

Staying with sensitivity capability investigations of plasmonic nanoparticles, in Chapter 7 we present experimental evidence - backed with Boundary-Elements-Method simulations - of increased single particle plasmonic sensitivity found at silver nanorods compared to gold nanorods with similar aspect ratios. I use the Drude-model of optical properties of metals together with the quasi-static-approximation for localized surface plasmons to express the sensitivity in wavelength units as a function of the resonance wavelength and Drude's material parameters, I investigate how the different contribution of the bound electrons to the dielectric response of silver and gold at optical frequencies impacts the plasmonic sensitivity. I discuss the applicability of noble metal nanorods for plasmonic sensing purposes by inspecting the reversibility of the nanorod sensors upon repeated cycles of environment changes.

Finally, in Chapter 8 we enter the realms of hybrid nanoparticles. Hybrid nanoparticles are nano-sized particles that are composed not only of different elements but also of functional or passive parts that posses different physical properties, like compositions of semiconductor nanoparticles and plasmonic noble metal domains. In this chapter I elaborate on the topic of growing gold domains on CdSe/CdS heterostructured quantum rods. Using the Plasmoscope I present experimental observations of growth of gold domains on single quantum rods. Finally, I will investigate possibilities of photocharging the gold domain and thus by increasing the electron density the shifting of the plasmon resonance wavelength.

In the concluding chapter a compact summary will highlight the results of this thesis.

Chapter 2

Nano-Optics of Metals and Semiconductors

Visible light covers the most fascinating spectrum of the electromagnetic radiation. This is due to the fact that the energy of photons of the visible light lies in the energy range of electronic transitions in matter. Spectrally selective absorption and scattering gives us the beauty of color which carries important additional information for the visual sensing that wouldn't be accessible by a purely monochromatic sensing scheme. This is probably the main reason why our eyes are adapted to be sensitive to the visible spectrum.

The major topic of this work is the optical spectroscopy of noble metal or semiconductor nanoparticles. Noble metals and semiconductors exhibit highly interesting properties at visible optical frequencies, which go beyond bulk electronic transitions. Bulk material properties (like atomic transition energy levels) are intrinsic and not or only slightly varying with the dimension of the matter, but as soon the area of the surface becomes comparable with the volume - and that happens when the particles reach sizes around 10-100 nm - confinement effects start to emerge leading to size- (and shape-) dependent optical properties. This opens up nearly infinite amount of ways to engineer materials and tune them to any requirements. Going to even smaller scales we arrive at single atoms or molecules or aggregates which possess also a lot of surprising properties, but they are - from the engineering point of view - still beyond the possibilities of the current material micro-processing technologies and therefore only bottom up (wet chemical) methods exists to produce these whereas larger nano-objects are often by top down methods (e.g. lithography).

The interaction of metals and semiconductors with light is largely dominated by the quasi-free conduction electrons. The band gap between conduction and valence bands in semiconductors is also a dominating factor and as we will also see here high energy valence bands in metals play also important roles in the optical response in the visible spectral region. Our most often investigated noble metals: Gold, Silver and Copper have all similar electronic configurations leading to similar optical response. One of the prominent interactions of these materials with light is the collective conduction electron oscillation, which is considered as a quasiparticle and is called plasmon. In case of semiconductor nanoparticles (also called quantum dots, QD) the prominent interaction with light is the creation of excitons, which is a quasiparticle consisting of an electron in the conduction band and a hole in the valence band. In subsequent chapters we will extensively elaborate the factors that influence the energy of these quasiparticles.

2.1 Electromagnetic radiation in the presence of polarizable media

To understand the properties of nano-scaled noble metal particles it is mostly enough to look at the Drude-Sommerfeld theory of metals. This theory is based purely on classical physics treatment of metals using concepts that were elaborated for the Maxwell-Equations. So before we take on the Drude-Sommerfeld theory we first consider the classical Maxwell-Equations that describe the time dependent electromagnetic field in presence of media. This introduction follows Chapter 2 of Novotny's and Hechts' Principles of Nano-Optics [Lukas Novotny, 2007] which presents a comprehensive introduction into the foundation of electromagnetic theory with special focus on nano-optics. After elaborating the basic equations of propagating light in matter we will turn our focus to the electronic properties of noble metals and semiconductors. We will especially concentrate on consequences of free electrons in crystals, so that we can understand many of the peculiar optical properties of the discussed materials. In certain cases when nano-objects get very small (single molecules) or when quantization effects are not negligible (quantum dots) it is necessary to adopt the quantum mechanical description.

2.1.1 The time dependent Maxwell-Equations

The interaction of the time dependent electromagnetic field with matter is defined by the time dependent Maxwell-Equations.

$$\nabla \times \mathbf{E}(\mathbf{r},t) = -\frac{\partial \mathbf{B}(\mathbf{r},t)}{\partial t} \tag{2.1}$$

$$\nabla \times \mathbf{H}(\mathbf{r},t) = \frac{\partial \mathbf{D}(\mathbf{r},t)}{\partial t} + \mathbf{j}(\mathbf{r},t) \tag{2.2}$$

$$\nabla \cdot \mathbf{D}(\mathbf{r},t) = \rho(\mathbf{r},t) \tag{2.3}$$

$$\nabla \cdot \mathbf{B}(\mathbf{r},t) = 0 \tag{2.4}$$

Where $\mathbf{E}$ denotes the external electric field, $\mathbf{D}$ the electric displacement, $\mathbf{H}$ the magnetic field, $\mathbf{B}$ the magnetic induction, $\mathbf{j}$ the current density and ρ the charge density. Bold letters represent vectorial quantities. The current density, electric displacement and the magnetic field are quantities that represent the effects of the electromagnetic field in matter after considering the superposition of the incoming fields and their influenced electromagnetic changes in matter such as charge separation and charge current. This influence can be of various kind both linear and non-linear. The incoming electromagnetic field causes the bound and unbound charge carriers to follow the external electromagnetic forces until they establish a new equilibrium of forces. This rearrangement of charges creates an internal electric polarisation that is represented by:

$$\mathbf{P}(\mathbf{r},t) = \varepsilon_0 \chi_e(\mathbf{r},t)\mathbf{E}(\mathbf{r},t) \tag{2.5}$$

During the rearrangement of charges currents arise, which is denoted by $\mathbf{j}(\mathbf{r},t)$, the current density:

$$\mathbf{j}(\mathbf{r},t) = \sigma \mathbf{E}(\mathbf{r},t) \tag{2.6}$$

Currents induce internal magnetic fields represented by the magnetisation:

$$\mathbf{M}(\mathbf{r},t) = \chi_m(\mathbf{r},t)\mathbf{H}(\mathbf{r},t) \tag{2.7}$$

Three material parameters have been introduced here: the electric and magnetic susceptibility, χ_e and χ_m and the electric conductivity, σ. These parameters are functions of position and time. The positional dependence is usually neglected since most of the problems can be piecewise decomposed to domains of homogenous media. On the other hand, the temporal dependence must be considered carefully as it is the reason for the frequency dependence of χ_e, $\chi_m$and σ and other parameters derived from these. Frequency dependency of the conductivity is a dominant influence in the optics of metals and we will discuss it later.

The superposition of external and internal fields yields thus for the electric displacement:

$$\begin{aligned}\mathbf{D}(\mathbf{r},t) &= \varepsilon_0\mathbf{E}(\mathbf{r},t)+\mathbf{P}(\mathbf{r},t)\\ &= \varepsilon_0\mathbf{E}(\mathbf{r},t)+\varepsilon_0\chi_e\mathbf{E}(\mathbf{r},t)\\ &= \varepsilon_0(1+\chi_e)\mathbf{E}(\mathbf{r},t)\\ &= \varepsilon_0\varepsilon E(\mathbf{r},t)\end{aligned} \tag{2.8}$$

with

$$\varepsilon = (1+\chi_e) \tag{2.9}$$

And similarly for the magnetic induction:

$$\begin{aligned}\mathbf{B}(\mathbf{r},t) &= \mu_0\mathbf{H}(\mathbf{r},t)+\mu_0\mathbf{M}(\mathbf{r},t)\\ &= \mu_0\mathbf{H}(\mathbf{r},t)+\mu_0\chi_m\mathbf{H}(\mathbf{r},t)\\ &= \mu_0(1+\chi_m)\mathbf{H}(\mathbf{r},t)\\ &= \mu_0\mu\mathbf{H}(\mathbf{r},t)\end{aligned} \tag{2.10}$$

and

$$\mu = (1+\chi_m) \tag{2.11}$$

With $\varepsilon_0 = 8.8542\cdot 10^{-12}As/Vm$ (vacuum permittivity) and $\mu_0 = 4\pi\cdot 10^{-7}Vs/Am$ (vacuum permeability). Equations (2.9 and 2.11) define the material parameters ε (dielectric or permittivity function) and μ (magnetic permeability function). These material parameters summarize all of the microscopic processes that influence the response of matter under the influence of electromegnetic field. Since most of the materials have negligible magnetic response at the frequency of the visible light the magnetic permeability is assumed to be 1. This implicates that for most of the time we will use only the electric field if we refer to light.

2.1.2 Electromagnetic wave in matter - the index of refraction

In chapter 2.1.1 I have stated the Maxwell-Equations. The Maxwell-Equations have a large number of solutions but one solution for which we interested is the solution of a propagating nondispersive wave (that is the wave form does not change with time in a reference system that moves with the wave). The simplest such solution is the time harmonic plane wave that can be obtained when we apply $\nabla\times$ to 2.1 and equate the right side with 2.2 while assuming that the medium is not conductive, $\mathbf{j}=0$ and does not contain free charges, $\rho=0$:

$$\nabla\times(\nabla\times\mathbf{E}) = -\mu\mu_0\frac{\partial}{\partial t}(\nabla\times\mathbf{H}) = -\mu\mu_0\varepsilon\varepsilon_0\frac{\partial^2}{\partial t^2}\mathbf{E} \tag{2.12}$$

Using the differencial vector operator identity: $\nabla \times (\nabla \times \mathbf{E}) = \nabla (\nabla \cdot \mathbf{E}) - \nabla^2 \mathbf{E}$ and 2.3, 2.12 becomes

$$\nabla^2 \mathbf{E} = \mu\mu_0\varepsilon\varepsilon_0 \frac{\partial^2}{\partial t^2}\mathbf{E} \tag{2.13}$$

which is the wave equation for a time harmonic wave that propagates with the velocity (*phase velocity*) of

$$c = 1/\sqrt{\mu\mu_0\varepsilon\varepsilon_0} \tag{2.14}$$

In vacuum where $\varepsilon = \mu = 1$ this velocity is $c_0 = 2.9979 \cdot 10^8 \frac{m}{s}$. Since in matter the speed of light is reduced by a ratio that is called the *index of refraction* $c = c_0/n$ we obtain the definition:

$$n = \sqrt{\varepsilon\mu} \tag{2.15}$$

Often, at optical frequencies the magnetic permeability approaches one,$\mu = 1$, so the index of refraction is conveniently defined as $n = \sqrt{\varepsilon}$. If $\varepsilon, \mu \geq 0$ one has to choose the positive square root to obtain the refractive index, whereas for negative values $\varepsilon, \mu \leq 0$ the boundary condition for the Maxwell-Equations at material interfaces require to take the negative square root. The implications of the negative refractive index lead to some very peculiar optical phenomena like perfect lensing with subwavelength resolution [Pendry, 2000]. The refractive index becomes the more important material parameter if the wave propagation is considered, whereas the dielectric function is commonly used if the Maxwell-Equations are considered.

The wave equation 2.13 can be fulfilled by numerous functions, the simplest that has a wide range of applications is the plane wave solution. To describe wave packages or other non-harmonic waveforms they have to be decomposed into a series of plane waves (Fourier decomposition), $\mathbf{E}(\mathbf{r}, t) = \int_{-\infty}^{\infty} \hat{\mathbf{E}}(\mathbf{r}, \omega) \exp(-i\omega t) d\omega$ with $\hat{\mathbf{E}}(\mathbf{r}, \omega) = \int_{-\infty}^{\infty} \mathbf{E}(\mathbf{k}, \omega) \exp(i\mathbf{kr}) d\mathbf{k}$. This enables us significant simplifications without sacrificing the generality of the theory.

The electric and magnetic field of a monochromatic (consisting only one frequency component, ω), propagating (in direction of $\mathbf{k}$) plane wave can be written as:

$$\mathbf{E}(\mathbf{r}, t) = Re\left\{\mathbf{E}_0 \exp(i(\mathbf{kr} - \omega t))\right\} \tag{2.16}$$

$$\mathbf{B}(\mathbf{r}, t) = Re\left\{\mathbf{B}_0(\mathbf{r}) \exp(i(\mathbf{kr} - \omega t))\right\} \tag{2.17}$$

Entering 2.16 and 2.17 in the time dependent Maxwell-Equations 2.1 to 2.4 in presence of polarizable media but not conductive media $\mathbf{j} = 0$, $\rho = 0$ we obtain the spectral representation of the the Maxwell-Equations:

$$\mathbf{k} \times \mathbf{E}(\mathbf{r}) = \omega \mathbf{B} \tag{2.18}$$

$$\mathbf{k} \times \mathbf{H}(\mathbf{r}) = -\omega \mathbf{D} \tag{2.19}$$

$$\mathbf{k} \cdot \mathbf{D}(\mathbf{r}) = 0 \tag{2.20}$$

$$\mathbf{k} \cdot \mathbf{B}(\mathbf{r}) = 0 \tag{2.21}$$

From these equation we can see that $\mathbf{E}$ and $\mathbf{H}$ and $\mathbf{k}$ are mutually orthogonal to each other and that the amplitudes of the electric field and the magnetic induction are proportional to each other: $E = Bc$ where the factor if the speed of light in medium $c = c_0/n$.

2.1.3 The complex dielectric function and complex refraction index

Until this point the media we have been discussing were all non-conductive materials, thus we could set the current density and the free charge density to zero, $\mathbf{j} = 0$, $\rho = 0$. Since in this work we are dealing with optical response of object mainly composed of noble metals we need to elaborate the situation when the medium is conductive, that is $\mathbf{j} \neq 0$ and $\rho \neq 0$. Let's consider Ampere's Law,2.2 including the current density term: $\nabla \times \mathbf{H}(\mathbf{r}, t) = \frac{\partial \mathbf{D}(\mathbf{r},t)}{\partial t} + \mathbf{j}(\mathbf{r}, t)$. Replacing $\mathbf{D}$ with $\mathbf{D} = \varepsilon_0 \varepsilon \mathbf{E}$ and $\mathbf{j}$ with $\mathbf{j} = \sigma \mathbf{E}$ and remembering that $\mathbf{E}$ is the electric field component of a plane wave thus the differential operators $\nabla\times$ and $\frac{\partial}{\partial t}$ can be replaced by $\mathbf{k}\times$and $-i\omega$ respectively we obtain the equation:

$$\mathbf{k} \times \mathbf{H} = -i\varepsilon_0 \mathbf{E} \omega \left(\varepsilon + i \frac{\sigma(\omega)}{\omega \varepsilon_0} \right) \tag{2.22}$$

Where the term

$$\varepsilon + i \frac{\sigma(\omega)}{\omega \varepsilon_0} = \hat{\varepsilon}(\omega) \tag{2.23}$$

is commonly named as the *complex dielectric function* where the imaginary part accounts for the energy dissipation of the oscillating electric field in the medium. In this work we will refer on $\hat{\varepsilon}$ by simply writing ε and will implicitly assume that it is a complex number. As can be seen, the conductivity - or the forced movement of the free charge carriers - contributes to the dielectric function, although its contribution decreases with increasing frequency which indicates that at high frequencies the difference between bound and free charge carriers becomes less obvious.

The consequence of the dielectric function $\varepsilon(\omega)$ becoming complex is that the refractive index also becomes complex:

$$\hat{n} = n + i\kappa = \sqrt{\varepsilon} \tag{2.24}$$

thus

$$Re\left[\varepsilon\right] = n^2 - \kappa^2 \tag{2.25}$$

$$Im\left[\varepsilon\right] = -i2n\kappa \tag{2.26}$$

2.1.4 The electric current and Drude's theory of conductivity

Since in this work the materials which we are mostly concerned with are noble metals we need to have a closer look into the physics of light matter interactions in presence of free charge carriers. In Chapter 2.1.1 we have introduced electromagnetic quantities that describe the electromagnetic field in matter that interacts with charged particles like electrons and ions. In general two types of electrons are present in a medium:

1. freely moving charges like conduction electrons in metals and doped semiconductors or ions in electrolytic solutions

2. bound charges whose motion is confined to the vicinity of a resting position by some binding force

If an electric field is applied the freely moving carriers will travel following the electric field, this produces electric current and leads to the electric conductivity. The bound electrons will only be

displaced from their resting position resulting in electric and magnetic polarization of the medium. We present here a summary of Drude's model based on Chapter 1 of Ashcroft's and Mermin's highly recopmmended lecture book on solid state physics [Ashcroft, 1976].

The simple model of electrical conductivity presented here was developed by Paul Drude at of the beginning of the 20th century. For a conduction electron with charge e being in an electric field $\mathbf{E}$ and experiencing friction ζ the equation of motion is:

$$m\frac{d\mathbf{v}}{dt} + \zeta\mathbf{v} = e\mathbf{E} \tag{2.27}$$

The friction term ζv accounts for the influence of the ionic core and other conduction electrons. Neglecting the thermally induced random motion with velocity, v_0 that does not result in any macroscopic current, we can define the current density as:

$$\mathbf{j}(t,\mathbf{x}) = en\mathbf{v}_{drift}(t,\mathbf{x}) \tag{2.28}$$

where n is the electron concentration (number of electrons per unit volume), $\mathbf{v}_{drift}$ is the *drift velocity* of the conduction electrons that is an average velocity superimposed over the random motion, v_0. Using 2.28 in 2.27 we obtain the *generalized Ohm's law*:

$$\frac{\partial}{\partial t}\mathbf{j} + \frac{\zeta}{m}\mathbf{j} = \frac{ne^2}{m}\mathbf{E} \tag{2.29}$$

For static electric field $\mathbf{E}_0$ as the driving force we get the stationary solution:

$$\mathbf{j}(\mathbf{x}) = \frac{ne^2}{\zeta}\mathbf{E}_0(\mathbf{x}) = \sigma_0\mathbf{E}_0(\mathbf{x}) \tag{2.30}$$

with σ_0 as the *direct current conductivity.*

To express the friction term with parameters of the Drude-model we need to introduce the *relaxation time* τ. Basically this is the average timescale that is elapsing between two collisions of the accelerated electron. The acceleration is $\mathbf{a} = e\mathbf{E}/m$, after time t the velocity of the electron is $\mathbf{v} = \mathbf{a}t + \mathbf{v}_0$. In time average the direction of the random motion changes, thus v_0 averages out to zero. We define the *relaxation time* τ, by

$$\tau : \mathbf{v_{drift}} = \mathbf{a}\cdot\tau = e\mathbf{E}\tau/m \tag{2.31}$$

Now equating 2.28 with 2.30 and using 2.31 we get an expression for the DC-conductivity:

$$ne\mathbf{v}_{drift} = \frac{ne^2\mathbf{E}\tau}{m} = \mathbf{j} = \sigma_0\mathbf{E}$$

$$\sigma_0 = \frac{ne^2\tau}{m} \tag{2.32}$$

The frequency dependent conductivity, $\sigma(\omega)$ can be expressed if we enter a time harmonic driving force with $e\mathbf{E}(t) = \mathbf{E}_0\exp(-i\omega t)$ into 2.29. We receive the solution:

$$\mathbf{j} = \sigma(\omega)\mathbf{E} = \frac{\sigma_0}{1 - i\omega\tau}\mathbf{E}$$

with:

$$\sigma(\omega) = \frac{\sigma_0}{1 - i\omega\tau} \tag{2.33}$$

	Au	Ag	Cu
electron density n/nm^3	59	57.6	84.5
DC conductivity, $\sigma_0/\left[10^7(\Omega m)^{-1}\right]$	4.9	6.6	6.5
effective mass m^*/m_e	0.99	0.96	1.49
bulk plasmon energy $\hbar\omega_p/eV$	9.1	9.1	8.8
relaxation time τ/fs	30	40	27

Table 2.1: Drude parameters of noble metals. DC conductivity σ_0 and electron density n from [Kopitzki, 1993], effective mass m^* from [Johnson & Christy, 1972] and the relaxation time τ from [Ashcroft, 1976].

If the frequency of the electromagnetic field approaches zero, $\omega \to 0$ the ac-conductivity reverts into the dc-conductivity. The ac-conductivity is a complex quantity that indicates the phase shift between the current and the temporally changing driving force.

Entering 2.33 into 2.23 we can express the dielectric function of a metal in terms of basic material parameters, such as the electron density, n and the relaxation time, τ.

$$\varepsilon(\omega) = \varepsilon - \frac{\sigma_0}{\varepsilon_0 \cdot (i\omega + \omega^2\tau)} = \varepsilon - \frac{ne^2\tau}{\varepsilon_0 m \cdot (i\omega + \omega^2\tau)} = \varepsilon - \frac{\omega_p^2}{\omega^2} \cdot \frac{1}{i/\omega\tau + 1} \tag{2.34}$$

where $\omega_p = \sqrt{ne^2/\varepsilon_0 m}$ is the *plasma frequency*. Introducing $\gamma = 1/\tau$, the scattering rate of the conduction electrons, we can express 2.34 as:

$$\varepsilon(\omega) = \varepsilon - \frac{\omega_p^2}{\omega^2 + \gamma^2} + i\frac{\omega_p^2\gamma}{\omega^3 + \omega\gamma^2} \tag{2.35}$$

The plasma frequency plays a crucial role in the theory of wave-like excitations of the conduction electrons and it turns out that this is the frequency of the eigenmode of the conduction electron density oscillations in bulk. This bulk conduction electron density oscillation is called *volume plasmon*. The volume plasmon depends only on the electron density and the effective mass as material dependent parameters and describes the behaviour of conduction electrons under oscillation. See Table 2.1 for a list of Drude parameters of the most common metals used in this work. See Chapter 2.2 for more elaborated discussion of plasmons.

For noble metals at optical frequencies where $\omega \approx 500THz$ and with $\tau \approx 30fs$ relaxation time we have $\omega\tau = 15000 \gg 1$, and 2.34 reduces to:

$$\varepsilon(\omega) = \varepsilon_\infty - \frac{\omega_p^2}{\omega^2} \tag{2.36}$$

Thus in the visible range the dielectric function of noble metals is mainly real.

2.1.5 Energy of light

So far we worked out the formalism that describes the electromagnetic wave in lossy media. With the Maxwell-Equations one can derive the temporal evolution of the electromagnetic field is certain initial and boundary conditions are known. Now we turn our attention to the focal point of the light matter interaction: the energy transfer. When light enters a dissipative medium energy is transferred to the medium. Since the knowledge of the amount of transferred energy is of crucial importance for a number of applications (photo-resists for lithography, temperature stress of biological samples, non-linear processes, speed of photo-reactions) it is important to understand the characteristics of energy transfer of light.

First, we start with the energy density of the electric field:

$$w_e = \frac{1}{2}\mathbf{D}\cdot\mathbf{E} \tag{2.37}$$

the energy density of the magnetic field:

$$w_m = \frac{1}{2}\mathbf{B}\cdot\mathbf{H} \tag{2.38}$$

Thus the entire energy density of the electromagnetic field is:

$$w = w_e + w_m = \frac{1}{2}\left(\mathbf{D}\cdot\mathbf{E} + \mathbf{B}\cdot\mathbf{H}\right) = \frac{1}{2}(\varepsilon\varepsilon_0 E^2 + \mu\mu_0 H^2) \tag{2.39}$$

Remembering from chapter 2.1.2 that the electric field and the magnetic induction are perpendicular to each other and to the propagation direction and their magnitudes are linked through the relation:

$$E = Bc \tag{2.40}$$

Using 2.40 and the identity for the speed of light in media $c = 1/\sqrt{\varepsilon\varepsilon_0\mu\mu_0}$ we can further simplify the formula for the energy density:

$$w = \frac{1}{2}(\varepsilon\varepsilon_0 E^2 + \mu\mu_0 H^2) = \frac{1}{2}\left[\varepsilon\varepsilon_0 E^2 + E^2/(\mu\mu_0 c^2)\right] = \varepsilon\varepsilon_0 E^2 \tag{2.41}$$

The transported electromagnetic power through a unit surface, A and at time t, is $P(t) = \frac{\Delta W(t)}{\Delta t} = \frac{w(t)Ac\Delta t}{\Delta t} = w(t)Ac$ thus the intensity (power per unit surface) is:

$$S(t) = w(t)c = \varepsilon\varepsilon_0 E(t)^2 c \tag{2.42}$$

The experimentally measured quantity is the time averaged intensity that averaged over large number of periods is (using $\overline{\sin^2(\omega t)} = 1/2$):

$$I = \overline{S} = \varepsilon\varepsilon_0 c E^2 \overline{\sin^2(\omega t)} = \frac{1}{2}\varepsilon\varepsilon_0 c E^2 \tag{2.43}$$

2.1.6 Attenuation of the electromagnetic wave in dispersive media

Due to incuring losses along its propagation, the electromagnetic wave can only travel a certain distance in a conductor. The penetration depth is defined by the length after which the intensity ($I = E\cdot E^*$) decays to 1/e-th of its value at the surface. The penetration depth at low frequencies is called *skin depth*. Skin depth played an important role in engineering of radio wave transmission technologies. For up to the radio wave frequency regime the classic formula for skin depth applies:

$$\delta_0 = \sqrt{\frac{\varepsilon_0 c\lambda}{\pi\sigma(\lambda)}} \tag{2.44}$$

This formula is based on assumptions of the Ohmic-law, thus only valid if the mean free path, l of the conduction electron is shorter than the distance over which the intensity of the electric field changes considerably, in words of the skin effect this distance is the skin depth, $l \ll \delta_0$. In other cases (like for microwave frequencies at very low

	$v_F \cdot 10^8 cm/s$	$\tau[fs]$	$l[nm]$
Cu	1.57	27	42.4
Au	1.40	30	42.0
Ag	1.39	40	55.6

Table 2.2: Fermi velocities v_F, Drude relaxation times τ, and mean free path $l = v_F\tau$ of Copper, Gold, and Silver. Values for v_F and τ taken from [Ashcroft, 1976].

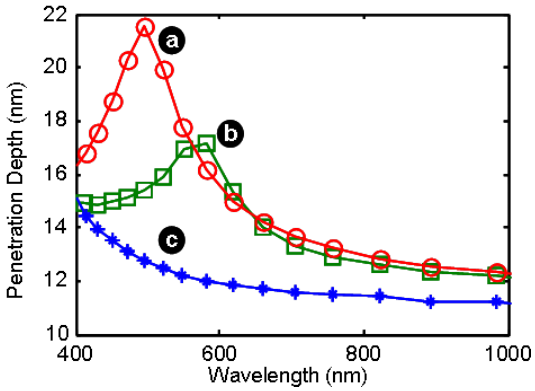

Figure 2.1: Optical penetration depth of gold (a), copper (b), and silver (c).

temperatures where the mean free path reaches lengths of up to $1cm$, or for optical frequencies where $\delta_0 = 2nm$ and $l \approx 45nm$) the condition is not fulfilled. In Table 2.2 we list the Fermi-velocities, relaxation times, and mean free path for noble metals. As it can be seen, since the mean free path is considerably larger than the classical skin depth we need to approach the attenuation of light in metals from an other direction.

The penetration depth of the electromagnetic field at optical frequencies can be estimated from the measured values of the complex refractive index, $\hat{n} = n + i\kappa$. While the real part is responsible to describe the speed change, the imaginary part describes the attenuation of the electromagnetic wave. Using $k = k_0\hat{n}$ as the wave vector in the medium:

$$E(x) = E_0 \exp i\,(kx - \omega t) = E_0 \exp i\,(k_0 n x - \omega t) \exp\,(-k_0 \kappa x) \tag{2.45}$$

The intensity of light in medium is thus:

$$I(x) = E(x)E^*(x) = E_0^2 \exp\,(-2k_0 \kappa x) \tag{2.46}$$

According to 2.46 the intensity of the electromagnetic wave is exponentially decreasing with the distance from the surface, and the rate of the decrease is characterized with the penetration length, δ_λ. The penetration depth can be expressed as a function of the wavelenght and the extinction coefficient where we use $k_0 = 2\pi/\lambda_0$, with λ_0 the wavelength of light in vacuum:

$$\delta_\lambda = \frac{\lambda}{4\pi\kappa(\lambda)} \tag{2.47}$$

In Figure 2.1 the penetration length is plotted versus the wavelength using refractive index data from [Johnson & Christy, 1972] where the refractive indices were obtained from reflectivity measurements on bulk materials. The penetration depth is following the characteristic free electron behavior of increasing transparency up to a threshold where additional excitations from the d-band alter the trend.

2.2 Surface plasmons

Conduction electron density oscillations are called plasmons. A density fluctuation that is propagating as a longitudinal wave through the bulk of the metal is termed as *volume plasmon* and

through its relation to the conduction electron density it is an important material parameter widely used in physics of metals. Under certain circumstances when the energy and momentum conservation condition is met, a surface wave of conduction electrons emerges that is called *surface plasmon* or *surface plasmon polariton* (SPP). The formulation of "surface plasmon polaritons" is the more exact term, because the energy of the wave is only partially stored in the metal in form of plasmons, the other part is contained in the surrounding dielectricum in form of polaritons. Surface plasmon polaritons are generated by interactions of metals with light whereas volume plasmons can not be generated by light due to the volume plasmon's longitudinal character. We can distinguish between two sub-classes of surface plasmon polaritons depending on the level of confinement. Propagating electron density oscillations are called *propagating surface plasmon polaritons* (PSPP), whereas electron density oscillations that are localized to a single nanoparticle and thus are not propagating are called *localized surface plasmon polaritons* (LSPP) or *particle plasmons*. In the subsequent sub-chapters we will provide an introduction into the optical properties of noble metals and, as a consequence thereof, into the charcteristics of LSPPs.

2.2.1 Optical properties of noble metals

The optical properties of metals are predominantly influenced by the conduction electrons and in certain cases (like the noble metals) by bound electrons located in bands that are close to the Fermi-surface. If a photon hits the metal, it is either reflected, absorbed or (if the metal is thin enough) transmitted. As it is known from the electromagnetic theory the spectral characteristics of the reflectivity depend on the dielectric function of the metal, which in turn depends strongly on the frequency dependent conductivity. Thus if a reflection from a metal surface appears colored, it means that there are abrupt changes in the conductivity in the visible range, which in turn is an indication of the onset additional mechanisms on top of the free electron reflectivity. There are two signature porperties of noble metals: (1) copper and gold are known for their yellowish appearance, whereas silver has a metallic brilliance, (2) all noble metals exhibit a strong plasmon resonance (coherent oscillations of the conduction electrons) although it is worth mentioning that this is not exclusively limited to noble metals.

Noble metals are monovalent metals (similarly to alkali metals), their electromagnetic properties are dominated by an electronic structure with a single valence electron occupying an s-orbital (Cu: $[Ar]3d^{10}4s^1$, Ag: $[Kr]4d^{10}5s^1$, Au: $[Xe]5d^{10}6s^1$). In this regards noble metals are very similar to alkali metals except the existence of the filled d-orbitals right below the s-orbitals. The Fermi-surface approaches a spherical shape thus noble metals can be very well described with the free electron model as long as the d-band structure doesn't play any significant role. At excitation energies above $2eV$ for gold, and copper and above $4eV$ for silver, d-band electrons alter the free electron behavior modeled by the Drude-theory . The larger energy gap between Fermi-level and d-band explains also why is silver not yellow. The yellow color of gold and copper is a consequence of the increased absorbance in the green-blue region that is caused by additional absorption pathways above $2eV$ ($620nm$) by means of interband excitations of d-band electrons into the conduction band, whereas for silver the interband absorbtion happens in the UV-region invisible to the human eye.

2.2.2 Localized surface plasmon polaritos (LSPP)

The incident light that is interacting with the noble metal nanoparticle will be either scattered or absorbed. In case of scattering the optically excited electrons recombine radiatively, in case of absorption the electrons recombine through a series of non-radiative steps. The merit of these two optical properties are characterized by the wavelength dependent optical scattering and absorption

cross-sections, C_{sca} and C_{abs} [Bohren & Huffman, 1983]:

$$C_{sca}(\lambda) = \frac{8\pi^3 n(\lambda)^4 |\alpha(\lambda)|^2}{3\varepsilon_0^2 \lambda^4} \tag{2.48}$$

$$C_{abs}(\lambda) = \frac{2\pi n(\lambda) \cdot Im\{\alpha(\lambda)\}}{\varepsilon_0 \lambda} \tag{2.49}$$

Where we have two wavelength, λ dependent parameters, $n(\lambda)$ the refractive index of the embedding medium and $\alpha(\lambda)$, the polarizability of the nanoparticle. ε_0 is the vacuum permittivity. The optical cross-section indicates the efficiency of the optical interaction between the nano-particle and the incident light with $C = P/I_0$ where P is the scattered or absorbed energy per unit time (power) and I_0 is the incident intensity (energy per unit area and unit time) . In case of an assymmetrically shaped nanoparticle the interaction can vary considerably in dependence on the orientation relative to the incident light. In [Becker, 2010], Chapter 2.2.2 an extensive derivation of the polarizaibility in the framework of the *quasi static approximation, QSA* is given. QSA assumes that the size of the nanoparticle in the propagation direction of the incident light compared to the wavelength in the particle is small and that the electromagnetic field penetrates the particle, therefore at a given time the electric field in the lengthscale of the nanoparticle can be considered to be constant. The assumption of the penetration of the electromagnetic field needs closer investigation since it is known that moving charges can screen out the electromagnetic field. This screening is the most effective if the electric conductivity is high which is the case for noble metals. The penetration depth in noble metals at frequencies of the visible light reaches $10-20nm$ (see Figure 2.1). Since the commonly used nanoparticles have diameters in the range of $10-30nm$, light penetrates deep into the nanoparticle, thus we can apply QSA to describe light-nanoparticle interactions with a good approximation. The polarizability α along a given axis i of an prolate shaped object within the quasi-static approximation is given by :

$$\alpha_i = V\epsilon_0 \frac{\epsilon_r - 1}{1 + L_i(\epsilon_r - 1)} \tag{2.50}$$

Where V is the volume of the particle, ϵ_r is the relative dielectric function defined as: $\epsilon_r = \epsilon_{NP}/\epsilon_m$ with ϵ_{NP} the dielectric function of the nanoparticle and ϵ_m the embedding medium, and L_i is called the depolarization factor along the axis, i. It is instructional to realize that the polarization is proportional to the volume of the particle. Consequently, according to 2.48 and 2.49 the scattering crossection depends quadratically on the volume whereas, in contrast, the absorption depends only linearly. This difference will be found to be at the root of experimental difficulties measuring scattering spectra of small nanoparticles. The depolarization factor is an indicator of how strongly the geometric shape of the particle is affecting the ability to obtain the most optimal polarization. The most optimal polariazation is that of an infinitely long rod oriented along the given axis. In case of prolate shaped particles with aspect ratio, $AR = a/b$ where a is the long axis and b the short axis, the depolarization factor along the long axis, a is [Osborn, 1945]:

$$L_a = \frac{1}{AR^2 - 1} \cdot \left[\frac{AR}{2 \cdot (AR^2 - 1)^{1/2}} \cdot \ln\left(\frac{AR + (AR^2 - 1)^{1/2}}{AR - (AR^2 - 1)^{1/2}} \right) - 1 \right] \tag{2.51}$$

This expression can be approximated by following expression for $AR \leq 8$ with an error of $<5\%$ [Sönnichsen, 2001]:

$$L_a = (1 + AR)^{-1.6} \tag{2.52}$$

Using a spheroid to simulate spectra of nanorods is enough if one wants to see tendencies, but for exact predictions a more accurate model is needed. The most comprehensive solution can be obtained by numerical simulations of the Maxwell-equations (2.1to 2.4). Such methods are DDA [DRAINE & FLATAU, 1994], BEM [Hohenester & Krenn, 2005, de Abajo & Howie, 2002] or FDTD [YEE, 1966].

The polarizability, α reaches maximum at wavelengths where the denominator approaches its minimum. This is the condition for the resonant oscillation of the electron cloud which is called *Localized Surface Plasmon Polariton (LSPP).* The resonance wavelength of noble metal nanoparticles lies in the visible range due to their material parameters (mainly due to their high conductivity). The exact location depends on various parameters, like *shape, volume, interparticle distance, optical properties of the surrounding material and electric charge* that will be discussed next.

2.2.3 Spectral dependency of LSPPs

The resonance position of LSPP is very sensitive to a large number of parameters that can be grouped into internal and external parameters. Internal parameters are those that can be controlled during nanoparticle synthesis and affect physical parameters of the nanoparticle, whereas external parameters are controlled by changing the environmental conditions (we disregard chemical reactions on nanoparticles which would belong to both groups). The group of *internal parameters* consist of: shape, volume and material composition, the group of *external parameters* are interparticle distance, optical properties of the surrounding material and electric charge. The list below is summarizing the basic influences that the aforementioned parameters have on the spectrum:

Internal parameters

1. *shape* - this is probably the most complicated parameter to describe since it can have various forms of influences in varoius degrees. Basically the more elongated the particle get the more red-shifted the spectrum goes. The elongated shape supports a higher polarizability thus a lower resonance frequency. An other view of the problem is in form of a model of a nanorod as an LC-circuit, where increased elongation increases both capacitance and inductance [Huang et al., 2009]. The curvature of edges has also a significant effect on the spectrum. Usually a higher curvature leads to a red shift of the resonance [Prescott & Mulvaney, 2008]. Increased number of symmetry axes lead to multiple plasmon excitation where the resonance shift tendencies need to be examined from case to case.
2. *volume* - increasing volume leads to a size that exceeds the limits where only a dipole excitation needs to be considered. At larger sizes multipole oscillations are possible, and retardation effects (spatially inhomogeneous electric field inside of the particle) lead to a red shift of the dipole excitation.
3. *material composition* - material parameters play a significant role in influencing the resonance position. High conductivity is an essential requirement for distinct LSPP resonances, thus only well conductive materials were reported to exhibit such excitations. Traditional plasmonic materials are copper, silver and gold, but [Blaber et al., 2009] discusses sodium, potassium and aluminum as other potential plasmonic materials. They find that, Na and K have very good conductivity and exhibit high quality plasmonic resonances in the visible range, whereas aluminum shows LSPPs in the UV regime but with a bad quality due to high intraband damping.

External parameters

1. *interparticle distance* - increasing interparticle distance of spheres leads to weakening plasmon coupling which results in a blue shift of the resonance towards the single particle resonance[Jain et al., 2007]. Interparticle distance and configuration of nanorods is more complicated since besides the distance the relative orientation of the nanoparticles, and the illumination polarization play also a significant role [Slaughter et al., 2010][Funston et al., 2009].
2. *optical properties of the surrounding material* - this well explored area plays a significant role in the growing interest in plasmonic nanoparticles for sensor applications. With increasing refractive index of the embedding medium the resonance wavelength shifts to the red due to the increased polarizability of the nanoparticle (see Equation 2.50).
3. *electric charge* - the LSPP resonance frequency is proportional to the bulk plasma frequency that is a fundamental material parameter of metals reflecting the density and the effective mass of the conduction electrons. Since negative charging increases the electron density thus the bulk plasma frequency, the resonance frequency of LSPPs shift also towards blue [Mulvaney et al., 2006].

2.2.4 Linewidth dependency of LSPPs

The plasmon resonance corresponds to a coherent oscillation of the conduction electrons of the particle. This oscillation dephases by various processes, such as scattering of electrons into empty levels in the conduction band, and electron– phonon coupling. The linewidth, as defined for oscillators, is the width of the resonance peak at half height with reference to the maximum as full height, thus it is often abreviated as FWHM (Full Width at Half Maximum). This certainly assumes that the basis of the peak is at zero. The linewidth, ΔE is related to the life-time of the oscillation, τ through Fourier transformation, with the temporal decay of the oscillation resulting in a linewidth greater than zero. The life-time of the oscillation depends on the bulk relaxation time τ_b and two more factors. One is the influence of the confinement of the conduction electrons into a region with dimensions smaller than the mean free path, l, the other is the coupling of the oscillating electrons to their own dipol fields that leads to radiation. The nano-confinement of the conduction electrons leads to an increasing damping with shrinking dimensions, whereas the radiation causes increased damping with growing volume. These damping mechanisms happen with different frequencies, and the sum of these frequencies yields the total frequency of damping mechanisms [Hu et al., 2008]:

$$\Gamma = \frac{1}{\tau_b} + \frac{v_F}{l} + \frac{\hbar \kappa V}{2}$$

where v_F is the Fermi-velocity, V is the volume and κ is the coupling factor to the radiation field.

At excitation energies of $2eV$ for gold and copper as well as at $4eV$ for silver additional bulk damping mechanisms surface that are absent at lower energies. These damping mechanisms originate from d-band electrons that are located below the half filled s-band (which is the conduction band). The d-band electrons enter the conduction band hence leaving a positively charged holes which act as additional scattering centers and increasing the damping.

2.3 Quantum emitters

As discussed earlier, the interaction of light with nanometer sized structures is the core subject of nano-optics. With shrinking particle sizes the laws of quantum mechanics become apparent in

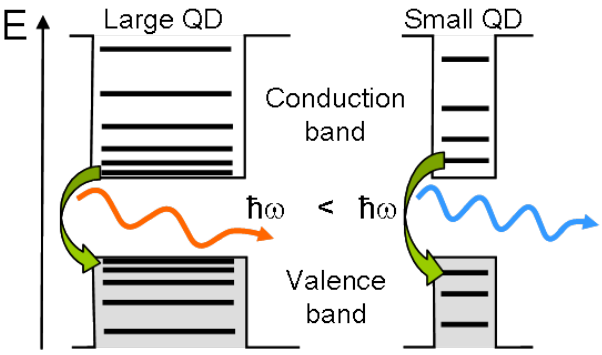

Figure 2.2: Nanocrystal quantum dots illuminated by UV-light emit light at a wavelength that depends on the size of the band gap. This behavior can be modelled quite well with quantum mechanical treatment of a particle in a box. According to this model the band gap, E_G itself grows with shrinking nanoparticle size, L: $E_G \sim 1/L^2$. The spacing between two consecutive state increases with shrinking quantum dot size.

their interaction with light. Continuous scattering and absorption of light will be supplemented or even replaced by the quantum mechanical approach of resonant interaction where the photon energy hits the energy difference of discrete internal electronic energy levels. In atoms, molecules and nanoparticles, like semiconductor nano-crystals and other quantum confined systems, the resonances are found at optical frequencies. Currently there are two large groups of quantum emitters that are intensively investigated: fluorescent molceules and semiconductor nanocrystals. Fluorescent molecules (a.k.a. dyes) are widely used substances in immunohistochemistry to color specific areas of the tissue. Quantum dots (Qdots) can be viewed as artificial atoms intermediate between molecular and bulk forms of matter. Given their photostability and their bright luminescence tunable in the entire range of the visible spectrum, they have been proven to be useful as biological labels [Bruchez et al., 1998], sensors [Medintz et al., 2003], laser [Klimov et al., 2000] and single photon sources [Michler et al., 2000].

A typical semiconductor nanoparticles employed as QDots are composed of an inorganic core of II-VI, III-V, IV semiconductors or carbon nanotubes surrounded by a passivating layer. This passivating layer is usually composed of organic materials but recently a vast field of core-shell systems have emerged. In order to improve the stability of the semiconductor nanoparticle against oxidation and to increase the quantum yield, an inorganic shell of semiconductor material with larger band-gap is deposited on the surface like CdSe/CdS or CdSe/ZnS nanoparticles (see Chapter 8). The properties and functional behavior of these core-shell compund semiconductor nanoparticles depend largely on the electron affinity (χ) defined as the energy between the conduction band edge and the vacuum level, and the band gap (E_g) defined as the energy difference betwee valence band edge and conduction band edge. These and some other significant parameters are listed in Table 2.3 for II-VI semiconductors.

In the next chapters we will introduce low dimensional (0D or 1D) semiconductor nanoparticles and discuss some fundamental properties thereof, then we will introduce the phenomena of nanoparticle blinking that has an important consequence on the experimental applicability of these objects.

2.3.1 0-Dimensional Semiconductor Nanoparticles - Quantum Dots

Semiconductor nanoparticles are also known as colloidal quantum dots. Various experiments show that colloidal solutions of the same semiconductor nanoparticles exhibit strikingly different colors when the size of the nanoparticles was varied. This phenomenon is called quantum confinement effect and is attributed to the size dependent energy gap of the semiconductor nanoparticles.

If light hits the semiconductor nano-particle the electron in the valence band is excited into the conduction band. There is a weak bond between the remaining hole and the excited electron

Material Property	ZnS	ZnO	ZnSe	ZnTe	CdS	CdSe	CdTe
Bulk energy gap at $300K$ (eV)	3.68/3.91	3.4	2.71/–	2.39	2.50	1.75	1.48
Structure	ZB/WZ	WZ	ZB/WZ	ZB	WZ	WZ	ZB
Electron affinity χ (eV)	n.d.a.	n.d.a.	4.09	3.53	4.79	4.95	4.28
Effective mass (m^*/m_0)	–0.40	–0.27	0.21	0.2	0.21	0.13	0.11
Exciton binding energy (meV)	36	60	21	10	30.5	15	12
Static dielectric const. ε	8.6	8.65	9.2	9.3	8.6	9.5	2.27
Exciton Bohr radius (nm)	-	-	2.32	2.46	2.17	3.87	1.09

Table 2.3: Selected physical parameters of II-VI semiconductor materials. Data taken from reference [Kasap & Capper, 2006]. (WB=Zinc-blende, WZ=Wurzit)

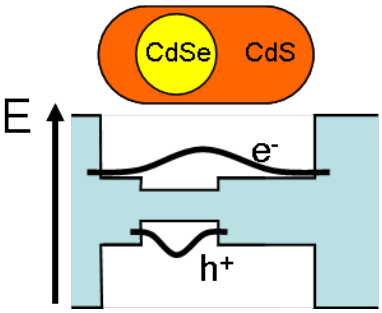

Figure 2.3: Electron delocalization in CdSe/CdS quantum rod composite. The type-I band alignment creates a potential minimum for both electron and hole in the CdSe core. The electron potential minimum is not deep enough to confine the electron thus the electron remains delocalized over the whole CdS domain whereas the hole confinement still holds. (The probability density of the hole is plotted in reversed orientation - it is getting larger towards the down direction).

thus these two are creating a quasi-particle called exciton. The excitons can be described by a hydrogen-like Hamiltonian and have a characteristic radius (Bohr-radius, see Table 2.3) that is usually similar or larger than the dimension of the semiconductor nano-particle. Once the size of a semiconductor nanoparticles approaches the limit of the Bohr-radius of the exciton, the energy gap and the band to band emission energy increases leading to an overall blue shifted spectral response. [?][?]A simple potential box model explaining the shift of the luminescence wavelength is shown in the Figure 2.2. In bulk crystals, each electron band consists of a continuum of electron states. However, the energy spacing of electron states increases with decreasing QD size, and therefore the energy spectrum of an electron band approaches a set of discrete lines in nanocrystals.

The most often used semiconductor nanoparticles are wide-bandgap II–VI (CdSe) or III-V (GaAs) compounds. They are often being applied to optoelectronic devices, especially light-emitting devices in the short-wavelength region of visible light, because of their direct gap and suitable bandgap energies.

2.3.2 1-Dimensional Semiconductor Nanoparticles - Quantum Rods

Recent developments in synthesis of II-VI semiconductors have resulted in fabrication of core-shell semiconductor nanoparticles, where the nearly spherical core is covered by an elongated shell composed of a semiconductor material with larger bandgap (see Chapter 8). These particles are often referred to as *quantum rods* Typical aspect ratios of 1:4 can be reached with lengths ranging between 15 and $20nm$. As an example for SC-nanoparticles with mixed dimensionality we can mention CdSe/CdS nanoparticles where the hole wave function is localized in the CdSe core (zero dimensional confinement) and the electron wave function is spread into the shell of CdS (one dimensional confinement) as illustrated on Figure 2.3. Besides the already observed surface passivation of the core, the elongated shaped outer shell brings some further advantages: (1) increased absorption cross-section, (2) lowered influence of surface charges that usually lead to

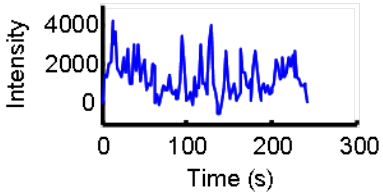

Figure 2.4: Measured intensity time trace of a blinking CdSe/CdS quantum rod. The temporal resolution is 1s.

fluorescence quenching, (3) enhanced quantum confined stark effect, (4) effective bandgap reduction [Muller et al., 2005] and (5) polarized emission [Hu et al., 2001].

2.3.3 Semiconductor Nanoparticle Blinking

Single semiconductor nanoparticles fluorescence signal goes alternately on and off under continous excitation (see Figure 2.4 for a typical intensity time trace). The particle switches between a fluorescent emission state and a dark state with random time intervals between the two states. This property, called fluorescence intermittency, is characteristic of the observation of single isolated qdots. The random switch between emitting and nonemitting states is a result of Auger transient ionization of the nanoparticle. If two excitons are created simultanously in the particle, the emitted energy of the first recombing pair powers the electron or hole of the other exciton into a surface trap. In such a case a permament ionization prohibits the radiative recombination of the subsequent excitons since the permanent dipol drives the electron or hole to a non-radiative Auger-type non-radiative recombination pathway through closely spaced surface states. Consequently, the average 'on' time reduces with increasing intensity [Nirmal et al., 1996]. As soon the particle returns to the neutral state, the pathway of radiative recombination is not obstacled anymore and the particle shows normal fluorescence.

2.3.4 Nanoscale Shottky Contact - Fermi Level Equilibration

When a semiconductor gets in contact with a metal surface, it undergoes Fermi level equilibration. For a bulk single crystal semiconductor the conduction and valence bands bend to form a charged region (depletion layer) as illustrated on the left side of Figure 2.5. The depletion layer which is dependent on the carrier density, can extend up to a few microns. This band bending acts as a rectifier, when such a semiconductor-metal junction is subjected to bandgap excitation, the band bending (Shottky-barrier) rectifies the flow of photoexcited charge carriers and produces photocurrent. On the other hand, in case of a nanoscale semiconductor-metal hybrid where the diameter of a semiconductor nanoparticle is significantly smaller than that of the depletion layer, there is no significant depletion layer within the semiconductor nanoparticle to hinder electron transfer (Figure 2.5, right side). As a result of this size limitation the bands remain flat across the particle and the charge separation is governed by the Fermi level equilibration. Consequently gold nanoparticles can store certain number of electrons. Since the photoelectron accumulation increases the Fermi level of the metal, the resultant Fermi level of the hybrid shifts closer to the conduction band of the semiconductor. It is important to recognize that the excess electron density is stored overwhelmingly on the metal domains because the Helmholtz (double layer) capacitance of the metal-solution interface is much higher than the capacity of the semiconductor/metal interface in the nanoparticle, even under accumulation. Hence, the Fermi level within the semiconductor nanoparticle will remain near the bottom of the conduction band. Additionally, as long as only a few electrons reside on the semiconductor nanoparticle, there will be no significant shift in the position of the band edges of the semiconductor nanoparticle due to the quantum confinement Stark-effect.

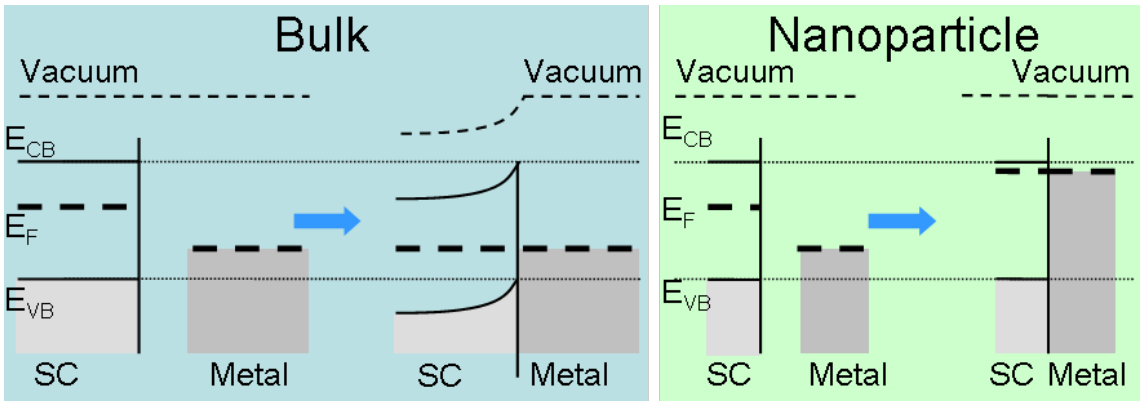

Figure 2.5: Fermi level equilibration. *Left side:* Bulk metal-(n-type)semiconductor contact. The chemical potential (Fermi-level) of bulk semiconductor is per definition in the middle of the valence band and the conduction band plus an energy difference in the order of k_bT. If the two bulk materials are in contact, the photoexcited electrons close to the contact quickly migrate to empty states in the metal conduction band due to the lower potentional energy in the metal. The charge separation creates a voltage bias over a so called depletion region in the semiconductor where the bands are bended up due to the low charge carrier density (thus there is no depletion region in the metal). The length of the depletion region reaches several microns. In equilibrium, further photoexcited electrons are driven away from the depletion region in the direction opposite to the metal and photocurrent arises. *Right side:* Nanocrystal metal-(n-type)semiconductor contact. Without contact the Fermi-levels are like in the bulk case. When both nanocrystals are in contact the photoexcited electrons migrate to the metal domain lifting the metal Fermi-level up to the semiconductor conduction band endge.

Chapter 3

Automated Scanning Single Particle Spectroscopy

Nanoparticle ensemble spectroscopy usually exhibits many dominant characteristics of nanoparticles, but due to inhomogenous broadening the observer gets little to no information about the single particle properties. Since the ultimate goal is to employ single nanoparticles for sensing applications beacause of their strong spectral dependency on the surrounding dielectric medium, efforts have been intensified over the past decade to learn more about parameters that influence the spectral response of single nanoparticles.

3.1 Nanoscale Optical Microscopy - Short Overview

Observing nanoscale structures by optical microscopy requires highly sofisticated contrast and resolution enhancement techniques since the strucutures are often significantly smaller than the wavelength of the visible light. The average size of electric circuits on a silicon chip is apporoaching dimensions well below 100 nm [Lithography, 2010], noble metal nanoparticles usually exhibit their most interesting novel property: the size confinment effect at sizes below 100 nm. Often such small structures have a very small scattering crossections that makes them hard to detect at all. Thus there are two key parameters of the microscope that need to be improved:

1. Resolution
2. Contrast

In following we will discuss the fundamental problem that limits optical resolution and list various methods that have been developed to increase resolution and contrast.

Resolution Enhancement

The resolving power of a microscope is described by:

$$d_{Rh} = \frac{1.22 \cdot \lambda}{NA_{cond} + NA_{obj}} \tag{3.1}$$

$$d_{Sw} = \frac{0.95 \cdot \lambda}{NA_{cond} + NA_{obj}} \tag{3.2}$$

Where NA_{cond} and NA_{obj} is the numerical aperture of the condenser and objective, respectively. The numerical aperture is defined by: $NA = n \cdot \sin(\alpha)$, where n is the index of refraction of the medium above the condenser and α is the half opening angle of the condenser with respect to the optical axis. λ is the wavelength of the illuminating light (Vis: $400nm$ (blue) to $700nm$ (red), NIR: $700nm$ to $1000nm$. The number of 1.22 stems from the definition created by *Rayleigh,* who defined the distinguishability of two point sources by placing the central maximum of the diffraction pattern of the one source right at the first minimum of the other, whereas 0.95 defines the minimum distance between two points where any intensity difference could be detected along the line connecting the two intensity maxima (proposed by *Sparrow*). Thus d is the smallest distance between two point sources that still can be distinguished. Both, 3.1 and 3.2 implicitly assume that $NA_{cond} \leq NA_{obj}$, otherwise the formula would give an irrational result for $NA_{obj} = 0$. As we will discuss briefly, the impact of NA_{cond} on the resolution is quite complex in case of $NA_{cond} > NA_{obj}$.

It is important to stress here that the reason that the high numerical aperture of the objective improves the resolution is that the larger numerical aperture enables the objective to capture high spatial frequencies which carry the fine details of the illuminated object. On the other hand the impact of a large numerical aperture of the condenser on the resolution is less intuitive. [Hopkins & Barham, 1950] showed that increasing NA_{cond} generally improves the resolution which reaches its lowest value at $NA_{cond}/NA_{obj} = 1.5$ but even at a ratio of 1 the resolution already approaches the optimum value very well, therefore it is best practice to use $NA_{cond} = NA_{obj}$ for most of the cases unless it is explicitly not possible. Such a case emerges if one uses the dark field microscopic technique (see section below discussing contrast enhancement improvements) where $min(NA_{cond}) > NA_{obj}$ because the illumination is not intended to enter the objective directly.

Besides increasing the numerical aperture of the objective there are other resolution enhancement methods that are frequently used:

1. *Solid immersion lens (SIL)* - using a small hemisphere with a high refractive index n_{SIL} attached to the surface above the area that needs enhanced resolution increases the NA of the microscope with a factor of at least by n_{SIL}. Using lenses made of GaP n_{SIL} can reach values up to 3.4 [MANSFIELD & KINO, 1990].
2. *Confocal Arrangement* - (this is a contrast improving technique, too) is a scanning microscopy method that using a small pinhole located at the optical axis in the image plane, thus only the signal originating from the focal plane (a.k.a conjugated detection plane) at the optical axis is being imaged, other signals are blocked. Thus if using high NA-objectives, where the focal plane has a very small thickness (sub-wavelength), sub-wavelength resolution can be obtained in the vertical direction. The lateral resolution remains still diffraction limited.
3. *Stimulated Emission Depletion (STED) microscopy* - is a scanning microscopy method that employs the stimulated depletion of fluorescent dyes at high laser intensities in an antigaussian depleting laser beam, lateral resolutions well below the wavelength of the illumination have been reached.
4. *Superresolution Microscopy (PALM, FPALM, STORM) microscopy* - based on the sequential localization of photo-switchable fluorescent probes that are switching stochastically between on and off states. Each diffraction limited spot can be fitted to find its centroid position allowing thus a resolution of a couple nanometers.

Contrast Enhancement

Contrast improvements help to reduce the signal to noise ratio that often overshadows the maximal achievable resolution. The most commonly used contrast improvement methods are:

1. *Dark Field Microscopy* - the illumination is shaped into a hollow conical form centered around

the optical axis and pointing to the object. The inclination of the inner surface of the hollow cone has a larger numerical aperture than the objective, thus no direct illumination enters the objective. But any scattering object that alters the direction of the light becomes visible above a dark background.

2. *Spatial-Modulation Spectroscopy* - developed for the observation of single nonluminescent objects such as very small (sizes below $15nm$) metallic nanoparticles, and uses a technique based on spatial modulation of the position of the studied particle and lock-in detection of the absorption of an incident laser beam.
3. *Differential Interference* - uses the phase difference of slightly displaced beams with peripedicular polarizations. The phase difference caused by materials with different refractive indices results in an interference pattern at the image plane. *Photothermal Imaging* uses this technique while employing the refractive index change induced by the heat that is generated by the nanoparticle when absorbing light.
4. *Confocal Arrangement* - (this is a resolution improving technique, too) is a scanning microscopy method that using a small pinhole located at the optical axis in the image plane, thus only the signal originating from the focal plane (a.k.a conjugated detection plane) at the optical axis is being imaged, other signals are blocked, and resulting in a drastic reduction of background noise.
5. *Fluorescent Microscopy* - in contrast to conventional bright field microscopy contrast mehtods using stains, this method uses fluorescent dyes to visualize certain areas of the sample. The excitation light is blocked with spectral filters and the Stokes-shifted emission of the dyes is observed. Fluorescent microscope produces a coloful image over a black background.
6. *2-Photon Microscopy* - high intensity laser beam is focused on the sample, and due to two-photon absorption a high energy photon is emitted. Since the illumination can be blocked with filters a high contrast image can be formed without using dyes. This method is preferably used with biological tissues, where the excitation is in the near-IR (biologic window) and the emission is in the blue.
7. *Raman Scattering Microscopy* - for the spontaneous Raman scattering, a laser excites the molecule from the ground state to a virtual energy state then the molecule spontaneously relaxes into a rotational or vibrational state. The difference in energy between the original state and this new state leads to a shift in the emitted photon's frequency away from the excitation frequency, and by blocking the illumination wavelength with a filter only the Raman-active molecules become visible.
8. *Coherent Anti-Stokes Raman scattering CARS* - a very sophisticated method employing two pulsed lasers that can be tuned. One laser excites the electron into a virtual state that is quickly deexcited by the stimulus of the second laser then the first laser excites the electron into an other virtual state from which it relaxes spontaneously into the ground state. If the frequency difference of the two pumping lasers match a vibrational mode an increased Anti-Stokes-shifted signal is detected resulting in a bond-specific fingerprint of the sample. This method is especially beneficial for samples where dye-molecules would significantly alter the system and it does not suffer from fluorescence background like the traditional Raman-Scattering Microscopy since it is an Anti-Stokes process.

3.2 Single Particle Spectroscopy

Since the emergence of single particle spectroscopy several methods have been developed to observe properties of single nanoparticles. One direction of improvements have been to increase sensitivity and precision like photothermal imaging [Boyer et al., 2002] and spatial modulation spectroscopy

[Arbouet et al., 2004] to measure even such small nanoparticles, where the scattering efficiency sinks into the noise level. Other methods use optical fibers instead of microscope objectives to collect the scattered light of a single particle [Kalkbrenner et al., 2004]. The other direction is to improve the throughput of spectroscopic instruments [Becker et al., 2007] in order to increase the number of measured particles. Having measured a high number of particles enables the experimentator to apply statistical analysis to identify trends of single particle spectrum properties [Becker et al., 2008].

Basically, for increasing the throughput the main task is to separate the spectra of point sources located in the entrance plane of the spectrometer. If two point sources are on the same line along which their signal is angularly dispesed to create the spectra, their spectra will overlap in the image plane of the spectrometer. Thus the task is to develop an automatized (or user-interaction free) method that can separate the spectra of these point sources. We list here two approaches to solve such a task:

1. *Spatial Multiplexing:* Stores the image of the sample at each wavelength. Each pixel of the CCD-camera is acting as a channel carrying the spectral information of the fraction of the image at the entrance plane that is imaged onto the pixel. There are two ways to scan through a wavelength range: either the illumination or the detection is wavelength selective. In case of elastic processes these two methods are equivalent.
2. *Wavelength Multiplexing:* Stores the spectral image of a narrow (ideally infinitely narrow) strip of the sample. Again, there are two ways to realize this intention: either by using a spatially addressable intensity modulator (or shutter since we only need on/off states) in the entrance plane or by a fixed slit in the entrance plane but with variably positioned microscope image (or the image content is variable), thus each frame contains the full spectral information of a narrow fraction of the sample. Each pixel of the CCD-camera is acting as a channel carrying the intensity information of the sample for a given wavelength along a lateral dimension that is defined by the orientation of the spectrometer. Our microscope setup that is described later is employing this last method.

Earlier attempts (FastSPS [Becker et al., 2007] and RotPol [Schubert et al., 2008]) of accelerating the single particle spectroscopy have resulted in significant success: the number of measured particles per run grew from ca. 30 up to over 100, and the time taken for one run reduced from 2 hours to 10-20 minutes. FastSPS uses a spatially addressable liquid crystal pixel array modulator (wavelength multiplexing), on the other hand as a realized example of spatial multiplexing, RotPol uses a tunable wavelength filter between microscope and spectrometer.

3.3 Improving Sensitivity and Spectral Range: Automated Scanning Single Particle Microscope

The increased throughput obtained by introducing computer controlled intensity or spectrum modulating optical elements comes with certain limitations. First of all, the most constraining limitation is the spectral cut-off that only allows a spectral measurement up to 700 nm. This spectral cut-off is a critical limitation in observing single nanoparticles since projected applications of noble-metal nanoparticles include biological marking, and there is an urgent need to push the resonance wavelength of the nanoparticles more into the near infra red where the absorption by hemoglobin and water reaches a minimum. The mentioned spectral range is called therapeutic window or optical window and starts at $650nm$ and ends at $900nm$ [Weissleder, 2001].

To overcome the spectral limitations of previous spectroscopy setups we needed to find a method that does not include any optical elements that significantly absorb in the visible and the near infra-

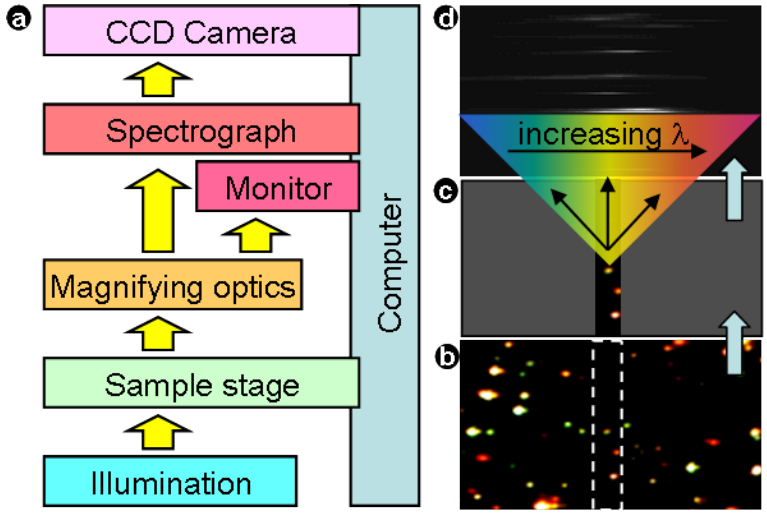

Figure 3.1: *Left:* System design chart (a) of the Automated Scanning Single Particle Microscope. The *yellow arrow* indicates the principal path of the light. *Right:* Spectrum creation using an entrance slit in the imaging plane of the microscope. The magnified image of the sample (b) is projected onto the entrance slit of the spectrometer cutting out a narrow vertical strip from the image (c), this strip is then spectrally dispersed inside of the spectrometer and imaged onto the exit image plane where a CCD camera is located (d). The slit size here is not to scale, in practical applications it is narrower.

red, thus we chose placing a vertical slit at the entrance plane of the spectrometer. The slit itself blocks every part of image except of a narrow vertical slit where the transmission is undisturbed. Using a slit is not new, since in the beginning days single particle spectroscopy setups were all using a slit with variable width. The only drawback of this method is that it is very cumbersome to align the region of interest of the sample in the region of the field of view that is projected on the slit. Thus the remaining task is to automatize the aligning procedure and develop an image capturing and data analysis algorithm.

The mentioned requirements for the new setup posed certain conditions on the envisioned microscope that could be only realized if the microscope was built from single modules instead of modifying an off-the-shelf microscope. Therefore I needed to lend extra attention to designing and aligning the optical path of the illumination and the signal. The illumination of the sample is often a neglected area in the microscopy community because the human eye can often easily compensate for brightness inhomogeneities or contrast issues. But for an automatized microscope that acquires the images automatically the homogeneous illumination of the sample is a critical issue, especially if one wants to compare measurements from different locations in the field of view. In my case I applied the principles of the *Köhler illumination* concept. Köhler's concept has the advantage that is washes out all intensity variations in the illumination and with the introduction of the field aperture and the condenser aperture it offers simple means to control the illuminated area and the brightness, respectively. In Appendix A, Figure A.2 the reader is presented with an accurate drawing of the ray paths in a microscope including the Köhler illumination concept.

3.3.1 The System Design

To create a setup that can produce a spectroscopic image of the sample using wavelength multiplexing (as described in Chapter 3.2) and a slit we need three devices (positioning device, spectrometer,

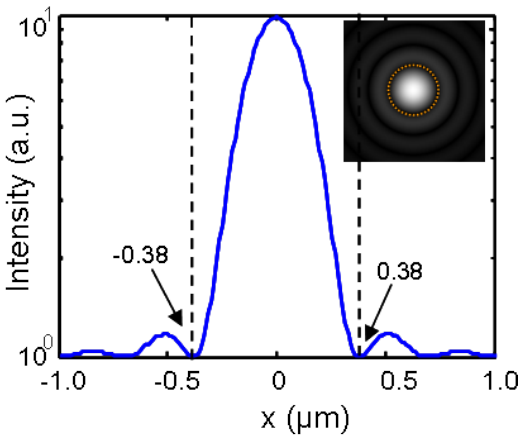

Figure 3.2: 1D cut through the (de-magnified) Airy-pattern, the diffraction limited image of a point source @ $700nm$ through the circular aperture of the objective ($100X$, $NA = 1.1$). The y-axis is plotted in logarithmic scale to make the secondary maxima more visible. The dashed lines indicate the position of the first minimum = the limits of the Airy-disc. Inset: the 2D image of the Airy pattern with Airy-disc (orange dotted circle).

and camera) to work together in sync since the sample must be positioned at the optical axis before the spectrum can be taken. Figure 3.1a shows the system design chart of the setup. Sample stage, spectrograph, and CCD-camera connected to the controlling computer. The computer controls the position of the sample, the settings of the spectrometer, and the image acquisition. The spectral map of the scanned area is then recorded by the following procedure:

1. Initialize sample position.
2. Take spectrum.
3. Move sample along the x-axis by a distance (scanning step size).
4. Repeat the step 2 and 3 unless the terminal position has been reached

As a result of the described procedure a spectral map is being acquired that is stored in a 3-d data array that we call the *data cube*. We will discuss the data analysis performed on the data cube in a subsequent chapter. Since this setup is based on the scanning principle it is crucial to understand and design the sample movement according to the requirements of gapless image reconstruction.

3.3.1.1 Sample Positioning

We use the sample stage (PI P-542.2CD Nanopositioning and Scanning Stage) to precisely position the sample. It has a travel range of $200\mu m$ in both x and y directions with a resolution of $2nm$. This travel range allows to access every corner of the sample within the field of view of the most commonly used high magnification microscopic objectives (Zeiss N-Achroplan 40X, NA=0.65 or Zeiss Plan-Neofluar Oil, Iris, 100X, NA=0.7..1.2). During a spectral scan the sample is moved in steps along the x-axis, while at each step the spectrum of the image is taken.

Scanning Step Size The step-wise shifting of the sample along the x-axis is performed with a certain step size, the *scanning step size*. To understand the influence of the scanning step size on the scanned image, let's discuss first how the spectrometer is positioned in the setup. The entrance of the spectrometer (SpectraPro 2300) is positioned in the image plane of the microscope where a slit with adjustable width cuts out a small 1-dimensional strip from the center of the image (Figure 3.1c) and only the light originating from this strip enters the spectrometer where the optical grating disperses it horizontally by directing photons with different wave vectors to different sides of the image plane of the spectrometer (Figure 3.1d). The most often used objectives in our experiments

Objective type	NA	Airy-Disc diam. (μm)
40X	0.65	0.8
100X oil imm.	1.1	0.67

Table 3.1: The diameter of the de-magnified Airy-disc for the most often used objectives.

have magnifications of 40X and 100X and numerical apertures of 0.65 and 1.1 respectively. The value of the magnification and the numerical aperture have an impact on the scanning step size. To obtain a complete scan (a scan that covers the whole area seamlessly) the step size must be so small that each accessible part of the sample gets imaged at least once through the slit. Therefore, ideally, the step size needs to match the (de-magnified) width of the entrance slit of the spectrometer. For example: if the entrance slit has a width of $1mm$ for 100X magnification the step size is ought to be $1/100mm$ thus $10\mu m$. If the step size is too large, gaps get introduced in the scanned image that leads to missing details of the sample. If the step size is too small - this would be the less critical problem - the scanned image contains overlapping image strips that need to be post-processed to obtain a non distorted image of the scanned area, but no information would be lost.

It is suitable to choose the slit width to be the size of the Airy-disc (Figure 3.2) diameter of the image of a point source. In such a case two or in worst case three strips completely contain the image (and consequently the spectrum) of a nanoparticle. Thus the step-size must not exceed the size of the diameter of the de-magnified Airy-disc. We talk here about the de-magnified Airy disc, since the Airy-disc and -rings occur only in the image plane, where the magnified image of the sample is, but for the step size we need to convert the image dimensions into sample dimensions. To get an estimate for the de-magnified Airy-disc diameter, s we recall the definition of the resolution limit defined by Rayleigh, d_{Rh}. Since d_{Rh} is the distance between the intensity maximum and the first minimum (which is zero), the size of the Airy-disc is twice of d_{Rh}:

$$s = 2 \cdot d_{Rh} \tag{3.3}$$

Table 3.1 lists the de-magnified Airy-disc diameters for 40X and 100X oil immersion objectives. These numbers times the magnification set a lower limit for the slit width, so to be on the safe size we usually use a de-magnified slit width of $1.5\mu m$ and a scanning step-size of $1\mu m$. The step size can be set in the *Scanning Imaging* dialog.

Scanning Travel Range The travel range of the positioning stage can be set within the *Plasmoscope* software environment that is accompanying the setup. Opening the *Scanning Imaging* dialog the user can enter the x-coordinate of the start and the end position. In most cases it is possible and recommended to use the full travel range ($200\mu m$) since it allows to measure the largest number of nanoparticles.

3.3.1.2 Spectrometer and CCD Camera Settings

The spectrometer (SpectraPro 2300 by Princeton Instruments/ACTON) is fitted with three optical dispersing elements, where one is a mirror, one is a 50 line/mm and one is a 150 line/mm grating. Before we can proceed to perform spectral measurements we need to set and check the width of the entrance slit as discussed in previous chapter.

We can easily set the slit width by observing the images of the sample that can be recorded with the CCD (Princeton Instruments Pixis 400B) camera. Setting the spectrometer into imaging mode with a nanoparticle sample inserted in the microscope and taking an image displays the sample with spherical discs representing the scattering nanoparticles. The micro-screw on the top

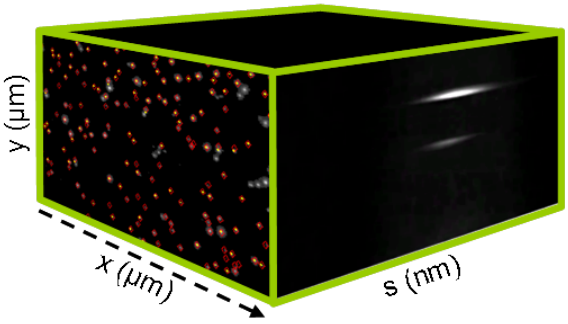

Figure 3.3: The *Data Cube* containing the spectral image of the sample. The dashed arrow along the x-axis indicates the scanning direction. The x-y-plane contains the intensity map of the sample at the corresponding wavelength (in this image we show the intensity map integrated over the full wavelength range and some particles are marked with red and yellow markers). The s-y plane contains the spectral data of a narrow strip of the sample at a given x-position. Each cut through the data cube parallel to the s-y plane contains a frame that has been recorded with the CCD-camera.

of the entrance serves to adjust the width with a very high precision. As mentioned in 3.3.1.1 it is suitable to set the width of the slit equal to the diameter of the Airy-disc. Since the micro-screw's scale doesn't give any valuable information about the width of the slit, we need to use the images acquired by the CCD camera to observe the nanoparticle relative to the slit. Using the *Move Stage* dialog of the Plasmoscope Software the user can fine-position with nanometer precision the nanoparticle to the center of the image and simultaneously can reduce the width of the slit until it reaches the Airy diameter size.

3.4 Data-Cube Analysis

A full spectral scan of the sample produces a large number of images (also called as frames). A standard measurement procedure results in a collection of 201 frames. Each frame contains the spectral image of a narrow strip of the sample. For the size of the strip see Chapter 3.3.1.1. Thus the complete data set constructs a 3D array (called *Data Cube)* where the dimensions have following meanings:

1. x - the lateral x-dimension, which is also the scanning direction. Its limits are given by the positioning stage travel range.
2. y - the lateral y-dimension. Its limits are given by the magnification of the objective.
3. s - the spectral dimension. Its limits are defined by the central wavelength - the wavelength that is mapped into the center of the CCD-chip. The extent of the spectral dimension is set by the used grating in the spectrometer. For the grating (150 line/mm) that we used exclusively in all our experiments the extent of the covered wavelength range is $568nm$ if the full width of the CCD-chip is being used. Thus if the central wavelength is $600nm$ the short wavelength limit is $600 - 568/2 = 316nm$ and the long wavelength limit is $600 + 568/2 = 884nm$.

The data cube contains the complete spectral information of the sample thus allowing for finding and analyzing the nanoparticle spectra. In the following chapter we will introduce the two most often used methods of finding a nanoparticle signal in the data cube.

3.4.1 Particle Signal Finding Methods

The data cube $\bar{\bar{M}}$, a three dimensional array obtained by a spectral scan of the sample contains all the necessary information that is needed to get the spectra of the nanoparticles that were located in the scanning range. To find areas where nanoparticles can be found we need to obtain

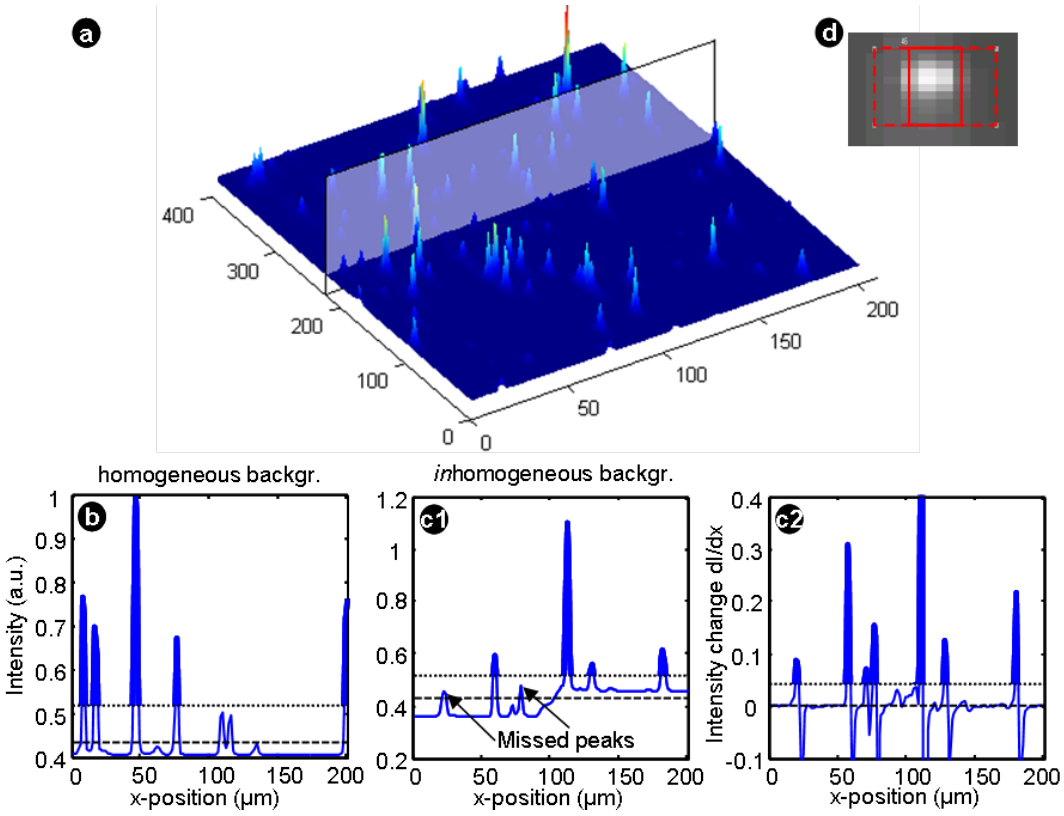

Figure 3.4: Particle Finding Methods. (a) 3D false color image of the intensity map of the scanned area. The semitransparent white rectangle indicates the location of the cut displayed in (b). (c1) a cut through an other intensity map with inhomogeneous background. (c2) cut through the intensity change map at the same position like (c2). (b, c1, c2): The dashed lines indicate the average of the intensity map, the dotted line is the same line displaced by a constant shift. Signal that shoots above the dotted line (thick blue contoured section of the data) is treated as particle signal. (d) The particle image in the intensity map. The red rectangle indicates the particle signal rectangle, the dashed red line indicates the background that is used for data processing.

the intensity map of the scanned area. The intensity map is the black and white image of the sample and it is created by summing up the data cube along the spectral axis: $I_{xy} = \sum_s \bar{\bar{M}}_{xys}$ with $x, y, N, M \in \mathbb{N}, x = 1..N, y = 1..M$ (N and M are the number of pixels along the x- and the y-axis) The obtained image of the sample contains bright spots over a dark background. We have developed two methods to locate the nanoparticles, with the first method, called *0th order method* being a simple, straightforward solution, and the second, called *1st order method* being an evolution of the 0th order method to overcome its shortcomings. Figure 3.4a shows the intensity map I of the scanned area. The areas containing useful signals in the intensity map, I are termed *signal areas.* Since the diffraction limited image of a point source is a circular disc, the signal areas that we are interested in are disc shaped. But in order to simplify the data handling we store the signal areas in a rectangular patch centered around the location of the maximum in the signal area. This rectangular patch, called *particle rectangle* is created by taking the smallest rectangle that fits around the disc shaped signal area (Figure 3.4d), and meets certain conditions that will be discussed in the followings where we elaborate the particle finding methods:

0th Order Method

This method has been developed first and the underlying principle of finding signals works well on a homogeneous background. It is based on the assumption that nearly all signal emitter are radiating with comparable intensities and furthermore the surrounding area consists of a constant featureless background. Such a background leads to an overall intensity increase, but has no further influence on the signal. Let us assume that there are Z number of signal areas. The signal areas S_n with $n = 1..Z$ are found by defining a threshold and taking the islands that are above the threshold (dotted line in Figure 3.4 b,c1) as individual signal areas . The threshold is defined by taking the average of the intensity map, $I_{avg} = \sum_{x,y} I_{xy}$ and adding a constant, C to it. The constant C is usually the standard deviation of the intensity map multiplied with a tuning factor that can be set by the user.

1st Order Method

The development of the 1st order method became necessary when many experiments were suffering under the influence of inhomogeneous backgrounds. Such inhomogeneities can arise when there are out of focus scatterers in the field of view like bubbles in the immersion oil under the sample or impurities on the cover slip. Since these scatterers are out of focus, their image is largely blurred creating a circular spot with a large diameter. Often the diameter is not large enough to cover the whole scan area. In such cases certain areas of the intensity map can have a higher background intensity than other areas. For example in Figure 3.4c1 we plotted a situation where the background intensity is mildly increased at ca. $100\mu m$ and maintaining a constant offset throughout the remaining of the x-axis. In this situation the 0th order method would lose some particles inevitably. But such frequent problems can be overcome if the particle signal finding method abandons the 0th order method and looks in more general properties of the particle signal. Such general property is the sudden and steep rise and fall of the intensity where the particle is. Taking the 1st derivative of the intensity map along the x-axis results in an *intensity change* map. The peak finding is performed similarly like in case of the 0th order method, but with added intelligence. The threshold is defined by taking the average of the intensity change map, $I_{avg} = \sum_{x,y} I_{xy}$ and adding a constant, C to it. The constant C is usually the standard deviation of the intensity change map multiplied with a tuning factor that can be set by the user. The intensity change map provides us additional information to identify a peak, as to every peak in the intensity

map corresponds a positive peak in the intensity change map immediately followed by a negative peak. Only such structures are particle signals, since a single positive (or negative) peak in the intensity change map would only represent a sudden increase (or decrease) in the signal but not a peak. In Figure 3.4 c1 and c2 we can compare the situations of inhomogeneous backgrounds from the 0th and the 1st order method's point of view. A cut through the intensity change map (Figure 3.4 c2) at the same position where the cut through the intensity map (Figure 3.4 c1) shows evidently that background inhomogeneities like constant offsets are completely suppressed, whereas a step in the intensity results only in a positive peak without the negative corresponding peak. Thus peaks that could have been eventually lost due to difficulties to set a proper threshold with the 0th order method are retained if using the 1st order method.

3.4.2 Spectrum Extraction

As we saw, the data cube contains the complete spectral information of the scanned sample area. In the previous chapter we described the methods that are used to find the signal areas. The signal areas contain the spectrum of individual nanoparticles, but on top of the signal of the nanoparticles overlays a background signal, and this whole signal is spectrally modulated by the wavelength dependent excitation, transmission and sensitivity of the setup. To extract the spectrum of the nanoparticle S_{NP} we need to apply a series operations (Equation 3.4) on the measured spectrum $S_{NP,msr}$. First subtract the measured background BG_{msr} from the measured spectrum $S_{NP,msr}$, and then normalize the signal to the detector response W. The detector response represents the spectral characteristics of the whole system in response to a constant incoming spectrum. Knowing the detector response the measured spectrum can be renormalized to cancel out systematic errors that originate from the spectral inhomogeneity of the illumination, optics, and detector sensitivity. The background, BG_{msr} is taken from the immediate surrounding of the particle. Due to the scanning principle of the image creation it is beneficial to take the background from a similarly sized and positioned area as the signal area but from a neighboring frame. By this we ensure that the particle and the background signal travel along the same optical path through the system thus we eliminate any systematic errors that would occur if the optical paths would differ. Especially effects of etaloning can be reduced using this background acquisition strategy.

$$S_{NP}(\lambda) = \left(S_{NP,msr}(\lambda) - BG_{msr}(\lambda)\right)/W(\lambda) \tag{3.4}$$

W is determined by measuring the spectrum of the illumination without sample in the microscope. We must proceed here with additional attention to a common systematic error originating from the detector. A constant offset that is electronically added to the signal to avoid negative counts caused by the noise. This is an additive error and has critical impact on the correctness of the data analysis. Luckily it affects the result only through W, because in the enumerator these additive systematic errors cancel out due to the subtraction of measured signal and background, $S_{NP,msr}(\lambda) - BG_{msr}(\lambda)$. The experimental determination of the electronic offset consists of taking a spectrum with closed shutter, thus leaving the CCD chip of the camera in complete darkness. The recorded the frame contains only a low intensity noisy signal called the *dark noise* D. To obtain the correct detector response, W we need to subtract the measured dark noise from the measured detector response $W = W_{msr} - D_{msr}$. The uncertainty that remains is due to noise and can not be eliminated although it can be overcome with sufficiently large signal strengths.

Chapter 4

Plasmon Resonance Linewidth of Au@Ag Nanoparticles

4.1 Introduction

The ensemble linewidth of a suspension of plasmonic nanoparticles is a convolution of the linewidth of individual particles and the distribution of their resonance wavelength. A narrow ensemble plasmon linewidth is desirable for most plasmonic applications such as sensors [Elghanian et al., 1997, McFarland & Van Duyne, 2003, Raschke et al., 2003], the enhancement of nonlinear optical effects [Nie & Emory, 1997, Kneipp et al., 1997, Campion & Kambhampati, 1998], light guiding [Maier et al., 2001, Quinten et al., 1998], labeling [Schultz et al., 2000], or tissue targeting [Brigger et al., 2002, Hirsch et al., 2003]. A small single particle plasmon linewidth implies a long plasmon lifetime, a large field enhancement, and a high sensing sensitivity. This intrinsic single particle plasmon linewidth is determined by the amount of damping and mainly due to inter-band and intraband excitation of electron-hole pairs, thus temperature, frequency, and material dependent[Sönnichsen et al., 2002]. The plasmon resonance wavelength is strongly dependent on the nanoparticle shape; a narrow ensemble linewidth indicates therefore a low polydispersity of the plasmonic particles. The main factor influencing the resonance wavelength of rod-shaped particles is the aspect ratio via a linear relationship we term the 'plasmon-shape relation'. Hence, three factors effectively determine the ensemble plasmon linewidth: (I) the single particle linewidth, (II) the width of the distribution in aspect ratios in the sample, and (III) the slope of the plasmon-shape relation connecting aspect ratio to resonance wavelength (Figure 4.1).

4.2 Reduced Ensemble Linewidth: Plasmonic Focusing

We find that coating gold nanorods with a thin shell of silver leads to a strong reduction of the ensemble linewidth. The quantitative examination of this effect leads to the surprising finding that it is caused by a change in slope of the plasmon-shape relation (factor III), an effect we term "plasmonic focusing". The silver coating leaves the shape and size of the original gold nanorods intact, excluding factor II from the discussion. The contribution of the single particle line width to the observed ensemble linewidth (factor I) is complex due to simultaneous shifts in the central resonance wavelength. However, we are able to show by single particle experiments together with theoretical modeling that the single particle linewidth contribution actually counteracts plasmonic focusing.

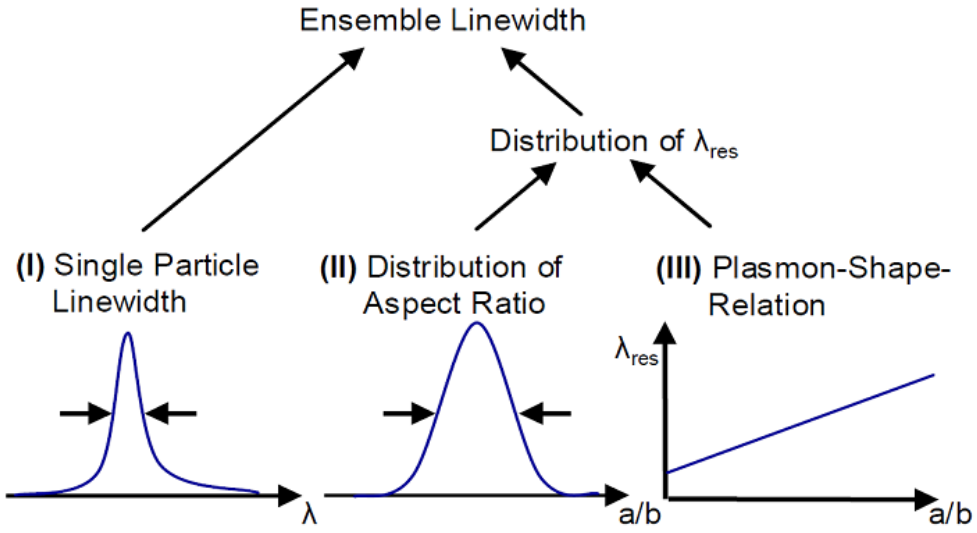

Figure 4.1: The three factors contributing to the ensemble plasmon linewidth: (I) the single particle linewidth, (II) the width of the distribution in aspect ratios (a/b) in the sample, and (III) the slope of the plasmon-shape relation connecting aspect ratio (a/b) to resonance wavelength (λ_{res}). A change in the slope of the plasmon-shape relation (III) is responsible for the ensemble linewidth narrowing of gold nanorods after silver coating. (Figure taken from [Becker et al., 2008])

4.2.1 Plasmon-Shape Relation of Nanorods

To explain our term plasmonic focusing, we first note that during nanoparticle crystallization in solution, the shape and size polydispersity of the ensemble typically increases by statistical variations over time. An exception is the well known (chemical) focusing regime during nanocrystal growth [Peng et al., 1998, Reiss, 1951, Yin & Alivisatos, 2005], where a faster growth of small compared to larger particles lets small particles "catch up". This effectively narrows or focuses the nanoparticle size distribution. The plasmonic focusing we observe, where the plasmon resonance linewidth of an ensemble of gold nanorods is smaller after silver coating than before, leaves the gold nanoparticles shape undisturbed but rather changes the way their shape polydispersity translates into spectral polydispersity. A shallower slope of the plasmon-shape relation narrows or focuses the distribution of plasmon resonances. In the ideal case of a completely flat plasmon-shape relation, all particles would have the same resonance wavelength regardless of their aspect ratio leading to an ensemble linewidth only limited by the intrinsic single particle linewidth. Another way of looking at plasmonic focusing is observing the spectral shift induced by the silver coating. Silver coating generally leads to a blue shift, but the shift is stronger for particles with resonances further in the red. Note the nontrivial choice of units in the discussion of linewidth changes accompanied with a resonance shift: a linewidth narrowing in energy or frequency units may correspond to a linewidth narrowing or broadening in wavelength units, depending on the magnitude of the resonance shift. Length or wavelength units have to be chosen here because of the almost linear relationship between aspect ratio and resonance wavelength [Link et al., 2005, Perez-Juste et al., 2005]. Other geometric factors besides aspect ratio, namely, end-cap geometry and particle volume, have a weak influence on the plasmon resonance compared to the aspect ratio [Prescott & Mulvaney, 2008, Bryant et al., 2008]. An ensemble linewidth in length units therefore relates to a certain polydispersity in aspect ratio regardless of the mean resonance wavelength. For other discussions, linewidth in energy units may be more appropriate, e.g., the single particles energy linewidth corresponds to the plasmon

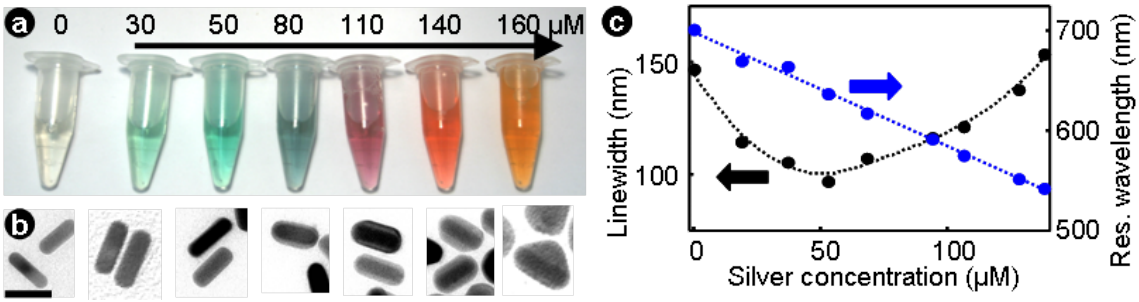

Figure 4.2: (a) True color photograph showing the color change of the pure gold nanorods (mean diameters 51 × 18 nm) (outer left sample) upon increasing silver concentration in the coating solution. The number above each vial indicates the concentration. (b) Representative TEM images corresponding to the samples shown above. They show the increasing thickness of the silver shell with increasing silver concentration becoming inhomogeneous at very high silver concentrations (scale bars for all images 50 nm). (c) Linewidth (black dots) and resonance wavelength (blue dots) as a function of silver concentration in the coating solution for a gold nanorod sample with a starting resonance wavelength of 700 nm and an initial line width of 148 nm. The shift in the resonance wavelength is approximately linearly dependent on the amount of silver present with a slope of -1.15 nm/µM (dashed blue line). The linewidth is the full width at half-maximum (fwhm) as determined directly from the spectra. It shows a minimum at 53 µM, where it is reduced to 97 nm from the initial 148 nm (dashed black line is a guide to the eye). (Figure taken from [Becker et al., 2008])

decay time.

4.2.2 Spectral Characterization of Silver Coated Gold Nanorod Ensemble

We produce silver-coated gold nanorods according to literature [?] by adding preformed gold nanorods [Nikoobakht & El-Sayed, 2003] to a coating solution containing silver ions. Increasing the silver concentration in the coating solution leads to a strong color shift (from green to orange-yellow, Figure 4.2a). The different electron density of silver and gold makes it possible to visualize clearly the silver shell around the original gold nanorod in transmission electron microscopy (TEM). The images confirm the expected increase of the silver shell thickness with increasing concentration of silver in the coating solution. When the silver concentration gets too high, the shell grows inhomogeneously (Figure 4.2b).

Extinction spectra of the solutions reveal a blue shift of the plasmon resonance wavelength of up to 150 nm (Figure 4.2c), which is approximately linearly dependent on the amount of silver present (slope about -1.15 nm/µM). The extinction spectra also show the strong narrowing of the plasmon resonance in the particle ensemble spectra after silver coating when compared to the linewidth of the original gold nanoparticles at least for thin silver coating. This narrowing has to the best of our knowledge not been reported before and is only observable if the silver shell is very homogeneous [?, Wang et al., 2005, Tsuji et al., 2006]. As can be seen from Figure 4.2b, a slightly thicker silver layer typically leads to more inhomogeneous coating resulting in a broadening of the ensemble linewidth compared to the optimal silver thickness.

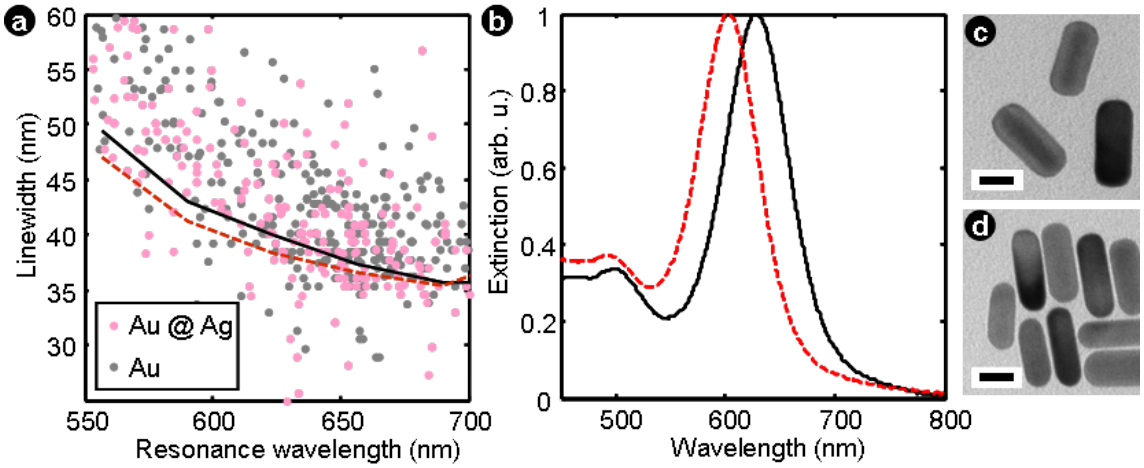

Figure 4.3: Single particle and ensemble spectra of silver coated gold nanorods. a) Linewidth vs. resonance-wavelength for bare (grey dots) and silver coated (reddish dots) gold-rods measured on over 400 single particles in each sample using an automated setup. This setup has a relatively high error in the linewidth determination. The lines show the trend with 90% of the particles above and 10% below (at each wavelength) for pure (black line) and silver coated (red line dashed line) gold rods. The line for silver coated nanoparticles is below the line for pure rods indicating a linewidth narrowing due to silver coating comparing particles at the same wavelength. b) Ensemble extinction spectra for bare gold (black line) and silver coated gold particles (red line). The silver-coated particles exhibit a blue shifted maximum. c)/d) TEM images of the pure (c) and silver-coated (d) gold particles, respectively. Scale bars are 20 nm. (Figure taken from [Becker et al., 2008])

4.2.3 Linewidth Analysis with Single Particle Spectroscopy

Before discussing the ensemble linewidth narrowing by plasmonic focusing in detail, we will first examine the single particle linewidth for coated and uncoated nanoparticles by observing the scattered light of individual nanoparticles in a dark-field microscope. Our setup is automated to allow the spectral investigation of several hundred nanoparticles with reasonable effort (see Chapter 3). For each particle spectrum, we extract the mean resonance position (λ_{res}) and the full linewidth at half of the maximum intensity Γ_{SP} (Figure 4.3a). Because the excitation of d-band electrons into the conduction band requires a threshold energy, the linewidth increases for higher frequencies or equivalently for smaller wavelengths. Hence, a plot of single particle linewidth Γ_{SP} as a function of the resonance wavelength λ_{res} shows an increase of linewidth at smaller wavelengths (Figure 4.3a). Most importantly, we observe a decrease of the single particle linewidth Γ_{SP} after silver coating compared to uncoated particles at the same resonance wavelength λ_{res}. Thus the plasmon oscillation with the same energy experiences a weaker damping if it occurs in a particle with a thin silver shell. The silver shell reduces the plasmon damping due to the higher energy required to excite d-band electrons into the conduction band in silver compared to gold. The interface between the gold core and the silver shell causes apparently no additional damping. A smaller single particle linewidth means lower plasmon damping, thus a longer plasmon lifetime and a higher field enhancement, which is beneficial for many plasmonic applications. If the silver layer becomes too thick, the particles start to lose their rod-like shape.

The smaller linewidth of silver-coated gold rods compared to uncoated gold rods at the same resonance wavelength is, however, not responsible for the observed linewidth narrowing of the ensemble linewidth. The reason is the simultaneous shift in resonance wavelength toward regions with

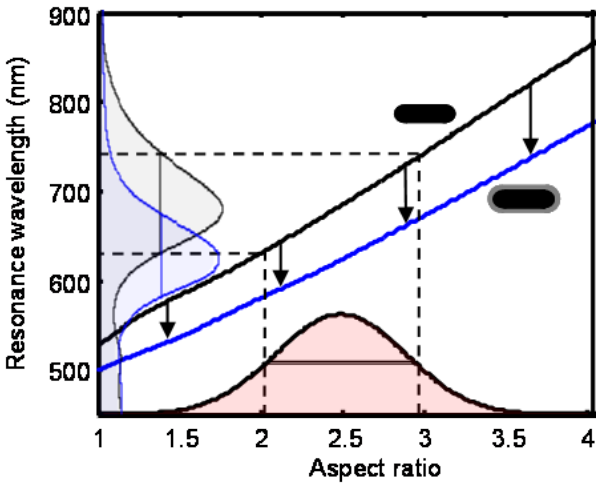

Figure 4.4: The plasmon-shape relation shows how the resonance wavelength depends on aspect ratio. Values derived theoretically within the quasi-static approximation are shown for gold rods in water (black line, n = 1.33) and with a 2.3 nm silver coating (blue line). The plasmon-shape relation converts an ensemble of particles with a distribution of aspect ratios (indicated by pink shading) into a distribution of resonance wavelengths (indicated by the gray shaded spectrum). The plasmon-shape relations are almost linear, i.e. a distribution of aspect ratios with a given width (polydispersity) gives a certain linewidth regardless of the mean aspect ratio. The shallower slope of the plasmon-shape relation for the silver-coated rods results therefore in a smaller spectral linewidth (blue shaded spectrum). An alternative way to look at the effect of coating is to observe the vertical differences between the two plasmon-shape relations (indicated by black arrows). Hence, rods with higher aspect ratio shift more on silver coating than those with a smaller aspect ratio. (Figure taken from [Becker et al., 2008])

intrinsically higher plasmon damping (Figure 4.3b). Depending on the initial and final wavelength, this shift in resonance wavelength often results in a broadening of the linewidth of a given particle after coating with silver. We observe such plasmon linewidth broadening of an individual particle by continuously monitoring individual particles exposed to a coating solution [Becker et al., 2008].

4.2.4 The Influence of the Plasmon Shape Relation on Ensemble Linewidth Narrowing

If a single gold nanorod is coated with silver, its resonance wavelength shifts towards blue. The silver layer alters the dielectric function of the nanorod and as its consequence the particle demonstrated a mixed behavior between pure gold and pure silver. The blue shift of the resonance wavelength is a phenomenon that is caused by silver. Silver is known to have higher energy localized surface plasmon resonance. But the blue shift of the resonance has also the consequence that its linewidth increases since at shorter resonance wavelengths the influence of d-band damping of gold increases. If the plasmon resonance linewidth of each silver coated single nanorod increases, why do we observe a narrowing of the ensemble linewidth? The answer is a change in the plasmon-shape relation, which converts the distribution of particle aspect ratios into a distribution of plasmon resonances. In chemical focusing during nanocrystal growth, the growth of small particles is favored, but in our case, the silver coating shifts the plasmon resonances stronger for rods with higher aspect ratios than for particles with lower ones. Therefore, the same particle distribution leads to a narrower distribution of plasmon resonances after coating due to a different slope in the plasmon-shape relation (Figure 4.4). This purely electrodynamic effect that we call plasmonic focusing is responsible for the observed narrowing of the ensemble linewidth. The shallower slope of the plasmon-shape relation for silver coated particles is caused by the strong

wavelength dependency of the dielectric function of silver due to the plasma of the quasi free conduction band electrons.

4.3 Summary

The analysis of the plasmon linewidth of silver-coated gold nanorods shows two surprising and important results: ensemble linewidth narrowing by plasmonic focusing and single particle linewidth narrowing, comparing particles with the same resonance wavelength. Even though silver-coated nanoparticles have been prepared and studied before, the linewidth narrowing of both the ensemble and of single particles has not been reported, probably because it is only present for very homogeneous silver shells. Only the spectroscopic investigation of several hundred single particles using an advanced single particle spectroscopy approach made it possible to obtain enough statistics to compare particles at the same resonance wavelength. Each individual particle shifts in resonance wavelength after silver coating, but observing many different particles allows comparing pairs with the same resonance wavelength. Since the damping (and thus the single particle line width) changes with resonance wavelength, only this direct comparison at the same wavelength makes sense. In combination with extensive particle size analysis by TEM, our electrodynamic model allows disentangling the contributions of single particle linewidth and plasmonic focusing for the observed ensemble linewidth changes. Plasmonic focusing alone would reduce the ensemble linewidth by about 30%; the convolution with single particle linewidth reduces the effect to about 20%. Plasmonic focusing is a new feature of bimetallic core-shell structures, interesting from a fundamental point of view. A sample preparation strategy with plasmonic focusing provides a simple method to obtain high-quality plasmonic particles with tunable resonance energy over the entire visible spectrum. The silver-coated gold nanoparticles we produce are among the best plasmonic structures known with up to 50% longer plasmon lifetime than gold nanorods at the same resonance energy, which will make them ideal candidates for the enhancement of nonlinear effects, sensing, and light-guiding applications.

Chapter 5

Copper - Gold Alloy Nanorods

5.1 Introduction

The vivid colors of plasmonic nanoparticles have attracted interest for decorative purposes since ancient times [Freestone et al., 2007]. New applications including optical sensing [Anker et al., 2008, Murphy et al., 2008], biological labeling [Pierrat et al., 2007, Sönnichsen et al., 2002], cancer therapy [Huang et al., 2008], and light guiding [Maier et al., 2001] have recently emerged. Tuning the plasmon properties (resonance frequency and linewidth) for the desired application is achieved through the nanoparticles' shape or material composition. Rod-shaped particles are the most useful plasmonic structures as their polarizability is strongly enhanced compared with more spherical shapes and their resonance frequency is dependent on the aspect ratio [Perez-Juste et al., 2005, Jana et al., 2001]. The material for plasmonic nanorods is almost exclusively gold because of its chemical stability and the availability of robust protocols for their high yield synthesis. Nanorods with a silver coating [Liu & Guyot-Sionnest, 2004] or a silver-gold alloy [Wang et al., 2005] have also been reported and shown improved plasmonic properties [Becker et al., 2008]. Gold-copper particles have only been synthesized without shape control [Sra & Schaak, 2004, Sra et al., 2005, Schaak et al., 2005]. In general, synthesizing alloyed nanocrystals is complicated by the tendency for self-purification [Norris et al., 2008, Dalpian & Chelikowsky, 2006]. Here, we report a protocol for producing rod-shaped single crystalline gold-copper ($Au_x Cu_{(1-x)}$) alloyed nanoparticles. We characterize them with various direct and indirect optical and electron microscopy techniques in order to verify the presence of copper in the particles. Pure spherical copper particles show no plasmon resonance because of the degeneracy with interband excitations of d-band electrons; AuCu nanorods are therefore the only plasmonic particles with high copper content. Changing the copper content allows us to vary the plasmon resonance frequency and linewidth. Electron diffraction and optical single particle plasmon-linewidth observations suggest an ordered AuCu lattice in the particles (at least after mild tempering) leading to reduced plasmon damping at specific stoichiometric copper contents. We prepare $Au_x Cu_{(1-x)}$ nanoparticles using a seeded growth technique modified from the procedure for gold nanorods published by Nikoobakht [Nikoobakht & El-Sayed, 2003]. Preformed gold seeds are added to a growth solution containing gold and copper ions in various ratios together with surfactants (cetyltrimethylammoniumbromide, CTAB) and reducing agents (ascorbic acid, AA). We characterize the resulting monocrystalline rod-shaped nanoparticles using transmission electron microscopy (TEM), energydispersive X-ray spectroscopy (EDS), solid state nuclear magnetic resonance (NMR), optical extinction spectroscopy (UV-vis), and darkfield single particle spectroscopy (DF-SPS).

5.2 $Au_xCu_{(1-x)}$Nanoparticle Synthesis

Deionized water (>18kΩ) is obtained from a Millipore system (Milli Q). Seed Synthesis.

Seed Synthesis

A total of 50 µL of 0.1 M tetrachloroauricacid ($HAuCl_4$) is added to 5.0 mL of water and mixed with 5.0 mL of 0.2 M CTAB in water solution. During vigorous shaking, 0.60 mL of ice-cold 0.010 M sodiumborohydride ($NaBH_4$) are added resulting in the formation of a brownish yellow or yellow solution. After 1 h at 35 °C, the solution can be used. Afterward, the solution is kept at 30 °C and used within one week.

$Au_xCu_{(1-x)}$Nanoparticles

Keeping the overall metal salt concentration constant at 5×10^{-4} M, we vary the molar ratio between $HAuCl_4$ and copper(II) chloride ($CuCl_2$) between 4:1 and 1:4. The metal salts are dissolved in 5.0 mL of water and mixed with 5.0 mL of 0.2 M CTAB solution. We add 10 µL of 0.04 M silvernitrate ($AgNO_3$) as in the pure gold rod recipe, which helps in the formation of rod-shaped particles. Then, we add just enough ascorbic acid (AA) to reduce all Au^{3+} and Cu^{2+} ions to their monovalent ions (c_{AA}) $c_{AA'}$ $x_{Au} + c_{AA'}$ $0.5x_{Cu}$ where x is the mole fraction of the element and $c_{AA'}$ the standard AA concentration for gold nanorod synthesis, $c_{AA'} = 0.0788$ M). The reducing agent changes the growth solution from dark yellow to colorless. After the addition of 12 µL of seeds, the solution gradually changes color within 10-20 min, indicating the growth of nanoparticles.

5.3 Characterization

Particle suspensions were characterized within one week after synthesis, typically on the same or the next day. For clarity, we named the samples according to the ratio of gold and copper ions present in the growth solution, which does not necessarily match the atomic composition of the final particles.

5.3.1 Applied Techniques

In this chapter we briefly introduce the characterization methods that were employed to detect the existence of copper in the nanoparticles. We present a lengthy introduction of the scanning dark-field microscopy setup in Chapter 3.

UV-Vis Spectroscopy

Extinction spectra were measured using an OceanOptics USB2000 Spectrometer equipped with an OceanOptics HL-2000-FHSA halogen lamp with a resolution of 1 nm.

NMR Spectroscopy

Static ^{63}Cu NMR Hahn-Echo spectra were acquired at 184.53 MHz using a Bruker Avance 700 spectrometer and an interpulse delay of 20 µs. A total of 12 µL of an Au_4Cu_1 nanoparticle solution were transferred into a commercial BRUKER 4 mm HR-MAS ZrO2 rotor, and measured at room temperature. 2 048 000 scans were accumulated using 200 ms relaxation delay. In addition, a background control spectrum was recorded (empty probe). All spectra were referenced with respect to solid copper(I) bromide at -381 ppm.

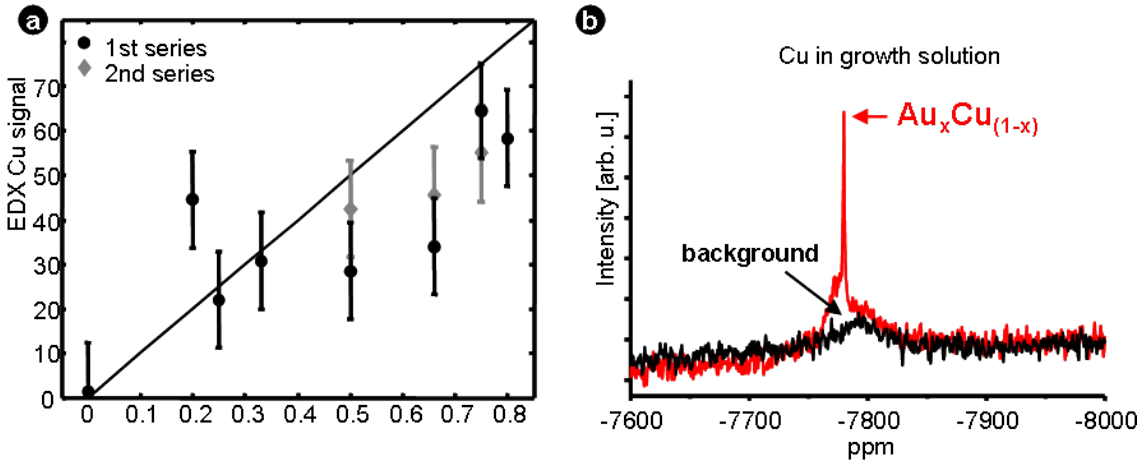

Figure 5.1: (a) Atomic composition of $Au_xCu_{(1-x)}$ particles with different copper amounts (x(Cu)) in the growth solution as determined by EDS on groups of particles. The values show a trend toward higher Cu content in particles produced from growth solutions containing more Cu. The measurement error (indicated by the error bars) is estimated by repeated experiments to be about 10%. A background value of 5% has been subtracted from the Cu content. Black dots: series shown in Figure 5.4. Grey diamonds: another series. (b) Static ^{63}Cu spectra of a $Au_xCu_{(1-x)}$ sample compared to the background. A sharp singularity at -7780 ppm and a broad featureless hump is observed, which clearly reveals the presence of Cu within the nanoparticles. (Figure taken from [Henkel et al., 2009].)

TEM

TEM analysis was performed at the Electron Microscopy Center (EMZM) at the University of Mainz, Germany, on a Philips CM12 using an operating voltage of 120 kV. EDS measurements were performed on a FEI Tecnai 30 (300 kV). Typically, EDS data was acquired in imaging mode on a group of particles using an integration time of 90 s. TEM samples were prepared from about 1 mL of nanoparticle solution, centrifuged twice for 10 min at a force of 9870 g (10000 rpm). The supernatant solution was first replaced by 1 mL and the second time by 300 µL of fresh water. A drop (5 µL) of this concentrated solution was deposited on a 200 mesh Formvarcoated copper grid and dried in air at 30 °C. For EDS analysis, Ni grids were used to reduce copper background. Statistical size analysis was performed on about 1000 particles for each sample. The particle sizes were measured by hand and, when possible, with the automatic sizing tool of the ImagePro software package. We cross-checked the reliability of the automatic count by hand for every image series and obtained the same sizes.

Dark Field Spectroscopy

Single particle scattering spectra were measured with the dark-field microscope setup described in Chapter 3 using a 40× objective (Carl-Zeiss NP-Neofluar). The applied particle signal detection scheme was chosen to be the 0th order scheme, which is setting a threshold on integrated intensity an picks the signal by finding the locations that exceed the threshold. A more detailed description of the method is presented in Chapter 3.4.1.

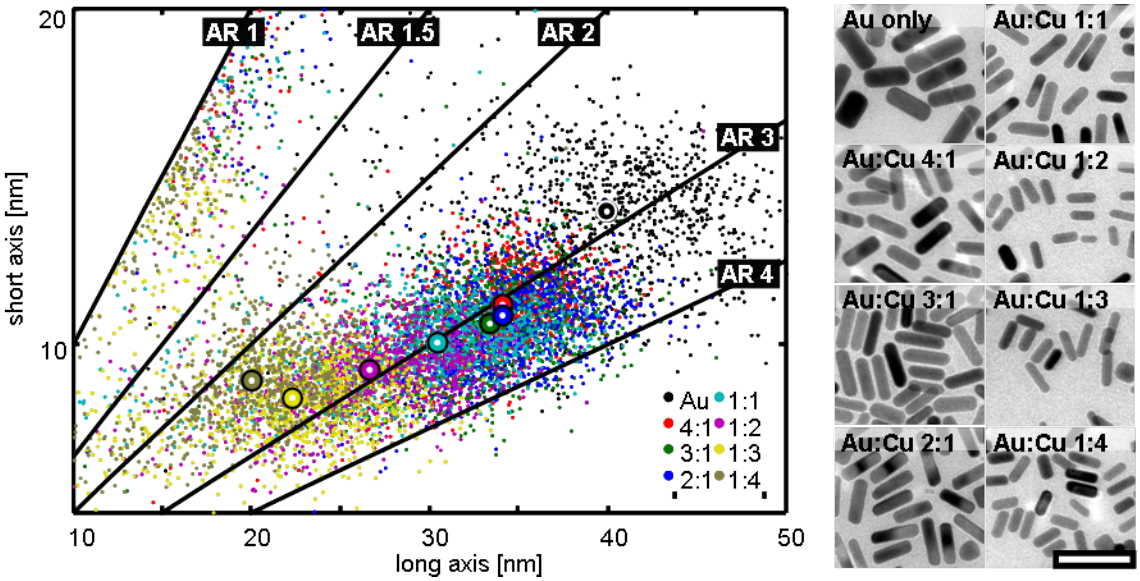

Figure 5.2: Size distribution and exemplary TEM images of copper-gold rods synthesized with different metal salt ratios in the growth solution. The thick circles mark the mean of the distribution and the lines indicate different aspect ratios. The aspect ratio (AR) of the rods stays close to an AR of 3 for all different compositions (compare TEM images), while the length and the width are decreasing with an increasing Au:Cu ratio. The differences in sizes can be clearly seen when the images of Au only and Au:Cu 1:4 are compared. Scale-bar 60 nm. (Figure taken from [Henkel et al., 2009].)

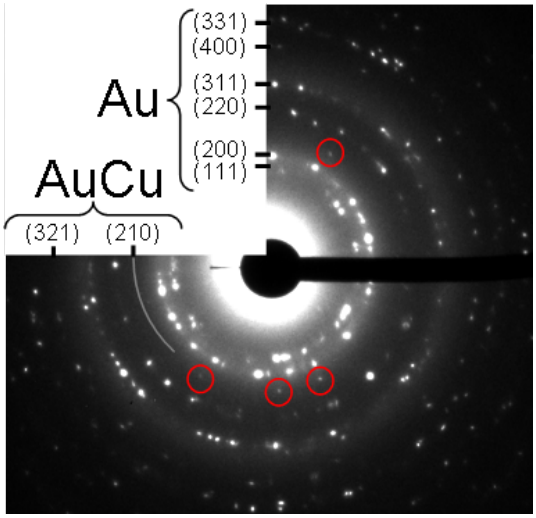

Figure 5.3: Selected area electron diffraction (SAED) pattern of Au_1Cu_1 particles heated by in situ TEM. At 400 °C, an $AuCu$ phase can be found indicating a phase transition. The red circles in the SAED emphasize some low index reflections (210), which start to appear at 350 °C. The shape of the particles is mostly preserved. (Figure taken from [Henkel et al., 2009].)

5.3.2 Characterization of the Material Composition

We need to establish first that copper ions present in the growth solution are indeed incorporated into the particles during growth. The most direct evidence for copper in or around the particles comes from EDS analysis and solid state NMR; both methods show a clear copper signal coming from the samples of nanorods grown in the presence of copper (Figure 5.1). Indirect evidence comes from optical spectra compared to TEM size analysis: the presence of copper changes the plasmon resonance position in a way incompatible with the shape variations observed by TEM (Figure 5.2). We will discuss the influence of copper on the optical spectra in Chapter 5.3.3 where we find that copper influences both the position of the resonance wavelength and the linewidth. Electron diffraction patterns of such samples show the emergence of a regular Au:Cu lattice after mild tempering (Figure 5.3), which may be responsible for the reduced plasmon damping. To quantify the amount of copper in the particles, we performed EDS (energy dispersive X-ray spectroscopy) analysis of the particles. Unfortunately, some Cu signals can be found in all EDS measurements (even when using Ni grids), because Cu is present in parts of the electron microscope. To account for this background Cu signal, we subtract a value of 5% from the measured Cu content, a value typically found on empty grids and on areas not containing particles. The mean values averaged over the course of at least three measurements show a trend toward higher Cu content in particles produced from growth solutions with higher Cu contents (Figure 5.1a). Generally, the copper content in the particles seems to be lower than its content in the growth solution. Interestingly, there is a good agreement with the expected amount at the Au:Cu ratios 1:3 and 3:1, which are known AuCu alloys with defined crystal structure [Villars et al., 1985]. However, the amount of copper we find in different parts of one TEM grid varies strongly (see error bars). Therefore, the presence of Cu was verified by solid-state ^{63}Cu-NMR for a sample with a low amount of Cu in the growth solution. The NMR clearly showed a Cu signal at -7780 ppm above background, confirming the presence of copper in the particles (Figure 5.1b) [Villars et al., 1985]

5.3.3 Impact of Copper Content on the Optical Properties of the Alloy-Nanoparticles

The plasmon resonance wavelength is a function of material composition, aspect ratio, and end cap geometry.[Prescott & Mulvaney, 2008, Kelly et al., 2003] We therefore carefully analyzed the ensemble extinction spectrum and single particle spectra in connection with particle sizes of samples with Au:Cu ratios of 4:1 to 1:4.

5.3.3.1 Dependence of Ensemble Extinction Spectrum Maxima on Copper Content

We carefully analyzed the particle sizes of samples with Au:Cu ratios of 4:1 to 1:4 by measuring the length and width of one thousand particles per sample on TEM images (Figure 5.2). The mean aspect ratio is about 3 except for very high copper contents (Au:Cu 1:3 or 1:4), where the aspect ratio decreases to about 2. We find a small fraction ($<$10%) of "spherical" particles with aspect ratios smaller than 1.5, which we excluded from the calculations of the means. The overall length and width of the particles (i.e., the volume) decreases continuously with increasing copper content, which points toward a less than stochiometric inclusion of copper into the particles. The polydispersity of the long axis is approximately 5% lower for the AuCu samples (15% instead of 20%) compared to a pure Au sample, while the polydispersity of the short axis stays the same. The curvature of the end caps increases with an increasing Cu amount. Increasing the content of Cu in the growth solution leads to a strong red shift of the maximum value in the extinction spectra (about 100 nm with respect to the pure gold sample) until a ratio of 1:1 is reached. Further increasing the amount of Cu shifts the spectra back to the blue (Figure 5.4b and c). When we

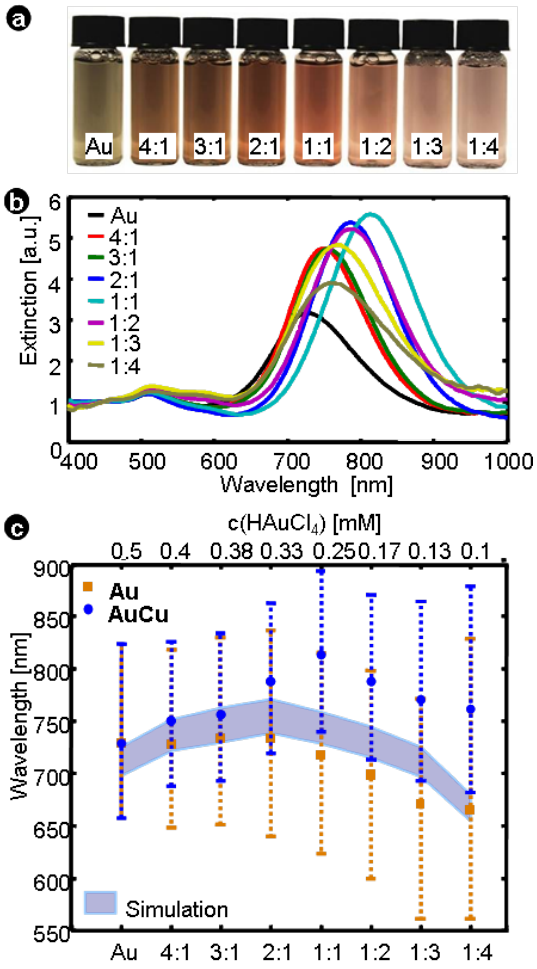

Figure 5.4: (a) Real color images of the gold copper samples (labels indicate the Au:Cu ratio). (b) Normalized optical extinction spectra of $Au_xCu_{(1-x)}$ samples with the composition indicated by the colors as noted. (c) Plasmon resonance wavelengths for ($Au_xCu_{(1-x)}$) samples with increasing Cu content. Increasing the Cu amount leads to a red shift of the longitudinal plasmon resonance with the strongest shift at a gold-to-copper ratio of 1:1 (blue dots, error bars show ensemble line-width). Further increasing the Cu content decreases the red shift. Pure Au samples (orange squares) with Au concentrations reduced in the same way as for the ($Au_xCu_{(1-x)}$) samples show a constant resonance wavelength or a blue shift compared to the original synthesis (for $c(HAuCl_4)$ smaller 0.25 mM). Since both the material composition and the particle morphology are shifting the plasmon resonance, this experimental comparison is not enough to conclude that copper is indeed incorporated into the particles. However, the shaded area shows the range of plasmon resonances expected from simulations for pure gold nanorods with different end cap geometry using the size distributions of the ($Au_xCu_{(1-x)}$) samples obtained by TEM analysis. The copper-gold nanorods are clearly outside this range confirming the presence of copper in the particles. The fact that the pure gold particles are also outside the simulation range is not surprising because their size distribution differs from those used for the simulations. (Figure taken from [Henkel et al., 2009].)

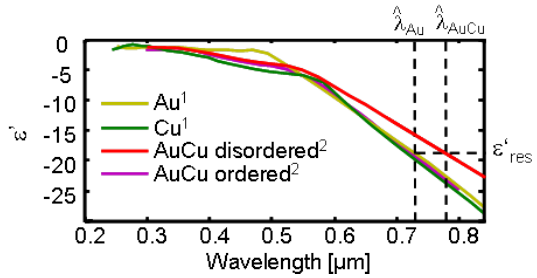

Figure 5.5: The real part of the dielectric functions gold, copper and gold-copper alloys ((1) by [Johnson & Christy, 1972] and (2) by [Köster & Stahl, 1967]). The dashed horizontal line at ϵ_{res} indicates schematically a value of the dielectric function where the plasmon resonance occurs in a given surrounding medium, since this value is reached at different wavelengths for different material compositions, the plasmon resonance occurs at different wavelengths ($\hat{\lambda}_{Au}$ and $\hat{\lambda}_{AuCu}$).

increase the copper content, we reduce the gold concentration correspondingly to keep the total metal ion concentration fixed. To exclude the possibility that the reduction of Au concentration itself is causing the observed spectral changes, we repeated the experiment leaving out the copper (adjusting the amount of ascorbic acid and $AgNO_3$ to the now reduced amount of metal ions). The extinction spectra for these samples show a constant resonance wavelength down to gold concentrations comparable to the Au:Cu 1:1 synthesis. At lower gold concentrations, the resonance wavelength shifts to the blue and a pronounced decrease of the total extinction is observable . Additionally, we checked the influence of the small amount of $AgNO_3$ present in the growth solution. We found opposite trends for particles with and without copper ions present in the growth solution: for pure gold rods, the plasmon resonance shifts to the red with increasing silver concentration, whereas in the presence of copper ions, the resonance shifts to the blue . The optical response of plasmonic nanoparticles can be simulated using the size parameters obtained from TEM (see above) and bulk dielectric functions with the Mie-Gans theory. Unfortunately, there are several conflicting dielectric functions reported for AuCu alloys, often only up to 800 nm (Figure 5.5). We therefore simulated spectra with the dielectric function of pure gold, which was successfully used to predict the spectral response of gold nanoparticles in earlier studies [Becker et al., 2007]. Here, we used both spherical and flat end caps to obtain a prediction band for the resonance wavelengths of pure gold particles (Figures 5.4c). We find a significant mismatch of the resonance wavelengths of AuCu particles compared to the predicted wavelengths for Au nanorods, especially for Au:Cu ratios above 2:1. This mismatch and the difference with the results from syntheses without copper indicate a difference in the dielectric function of the produced particles to pure gold particles, hence the presence of Cu in the particles. We looked for evidence of an ordered AuCu lattice using electron diffraction. At first, the sample Au_1Cu_1 showed the diffraction pattern expected for cubic (fcc) gold with a lattice constant of 0.403 nm (Figure 5.3) . However, after some moderate tempering (heating to 200 °C, leaving it constant for 20 min, then raising the temperature in 50 °C steps for 20 min until 400 °C), we observed clear evidence for an ordered AuCu phase. While heated, the shape of the particle was mainly preserved. First, additional diffraction spots (lattice constant 0.37 nm) were visible at 350 °C. At 400 °C, more spots appeared, which were distinct from those belonging to the 0.403 nm fcc Au lattice. Those new spots belong to an ordered AuCu phase with a lattice constant of 0.38 nm. That means that either parts of the particles or some of the particles that contained the right ratio of Au:Cu form an ordered AuCu phase.

5.3.3.2 Influence of Copper on the Resonance Wavelength of the Disordered Au_1Cu_1 Alloy

In this section we try to give a qualitative explanation for the red shift that is detected for nanorods containing copper. In Au:Cu nanoparticles with the composition ratio of 1:1 we saw the largest red shift of the resonance wavelength (around 100 nm). Since the ensemble extinction spectra were recorded for the unannealed particles we can strongly assume that the crystal structure of these particles was disordered, thus if we want to understand the optical spectra we need to take a closer look at the dielectric function of gold and disordered gold-copper alloys plotted in Figure 5.5. The real part of the dielectric function of Au_1Cu_1 (red curve) is shifted closer to zero in the visible wavelength range, especially from 600 nm onwards.

	Au	Ag	Cu
m^*/m_e	0.99	0.96	1.49
$\Gamma_{Drude}(meV)$	71	21	95

Table 5.1: The optical effective mass m∗ from [Johnson & Christy, 1972], free electron damping constant Γ_{Drude} from [Zeman & Schatz, 1987].

To understand why this shift towards zero causes a red-shift of the resonance wavelength, let us remind of the expression for microscopic polarizability from Chapter 2.2.2:

$$\alpha = V\epsilon_0 \frac{\epsilon_r(\lambda) - 1}{1 + L(\epsilon_r(\lambda) - 1)} \tag{5.1}$$

Where V is the volume, $\epsilon_r(\lambda) = \epsilon_{NP}(\lambda)/\epsilon_m$ is the relative dielectric function with $\epsilon_{NP}(\lambda)$ the wavelength (frequency) dependent dielectric function of the nanoparticle and ϵ_m the dielectric constant of the surrounding medium, which is water. Water has a constant dielectric function in the visible range. The parameter L is the shape dependent depolarization factor (as introduced in Chapter 2.2.2, equation 2.50) which has values between 0 and 1: $0 \leq L \leq 1$. We see, that to fulfill the resonance condition ($\alpha \to \infty$) the denominator has to approach its minimum (ideally it would approach zero $1 + L(\epsilon_r - 1) = 1 + L \cdot (\epsilon_{NP}(\lambda) - \epsilon_m)/\epsilon_m \to 0$, but clearly this can not be fulfilled with the complex dielectric function of gold. This is the reason for why plasmon resonances have a low Q value). But if we only consider the real part of the dielectric function $\epsilon'_{NP} = Re\{\epsilon_{NP}\}$, we can find a wavelength $\hat{\lambda}$ where the denominator reaches zero $1 + L \cdot \left[\epsilon'_{NP}\left(\hat{\lambda}\right) - \epsilon_m\right]/\epsilon_m = 0$, since $\epsilon_{NP}(\lambda)$ is negative in the visible range. That means, if we rearrange the resonance condition we obtain:

$$\epsilon'\left(\hat{\lambda}\right) = \epsilon_m \frac{L-1}{L} \tag{5.2}$$

This formulation makes it even clearer that the shape and surrounding materials define the resonance wavelength through the dielectric function of the noble metal. For both, Au and AuCu following relation must hold in case of a resonance:

$$1 + L_{Au} \cdot \left[\epsilon'_{Au}\left(\hat{\lambda}_{Au}\right) - \epsilon_m\right]/\epsilon_m = 1 + L_{AuCu} \cdot \left[\epsilon'_{AuCu}\left(\hat{\lambda}_{AuCu}\right) - \epsilon_m\right]/\epsilon_m = 0 \tag{5.3}$$

with $\hat{\lambda}_{Au}$ and $\hat{\lambda}_{AuCu}$ as the resonance wavelength of gold and disordered gold-copper nanoparticles, respectively. We can further simplify above expression, if we assume that L is the same for both samples. Since in case of nanorods L depends on the aspect ratio (AR): $L = (1 + AR)^{-1.6}$ (see Chapter 2.2.2) L would be the same, if both samples would have the same aspect ratio distribution. The analysis of the TEM images of (Figure 5.2) reveals that the aspect ratio distribution of both samples centers very close to the line for AR = 3. Consequently the assumption of $L_{Au} = L_{AuCu}$ holds and leads to:

$$\epsilon'_{Au}\left(\hat{\lambda}_{Au}\right) = \epsilon'_{AuCu}\left(\hat{\lambda}_{AuCu}\right) \tag{5.4}$$

Now, since $\epsilon'_{Au}(\lambda) < \epsilon'_{AuCu}(\lambda)$ and both functions are monotonically decreasing in the spectral range of interest (from 550 nm to near IR), we conclude that 5.4 can only be fulfilled if the resonance wavelength of gold-copper nanoparticles is longer than that of gold nanoparticles,

$$\hat{\lambda}_{Au} < \hat{\lambda}_{AuCu} \tag{5.5}$$

That means the higher real part of the dielectric function of disordered AuCu leads to a red shifted plasmon resonance if the other parameters stay constant for both samples. We indicated these findings with dashed lines in Figure 5.5. The line $\epsilon'(\lambda) = \epsilon_m \frac{L-1}{L} = \epsilon'_{res}$ intersects the curve of Au at a shorter wavelength than the curve of disordered AuCu.

We believe that the fundamental physical reason for red shift of the plasmon resonance wavelength is the larger optical effective mass of copper compared to gold and the larger damping that is also known to reduce resonance frequency of oscillators. The values for both parameters are listed in Table 5.1.

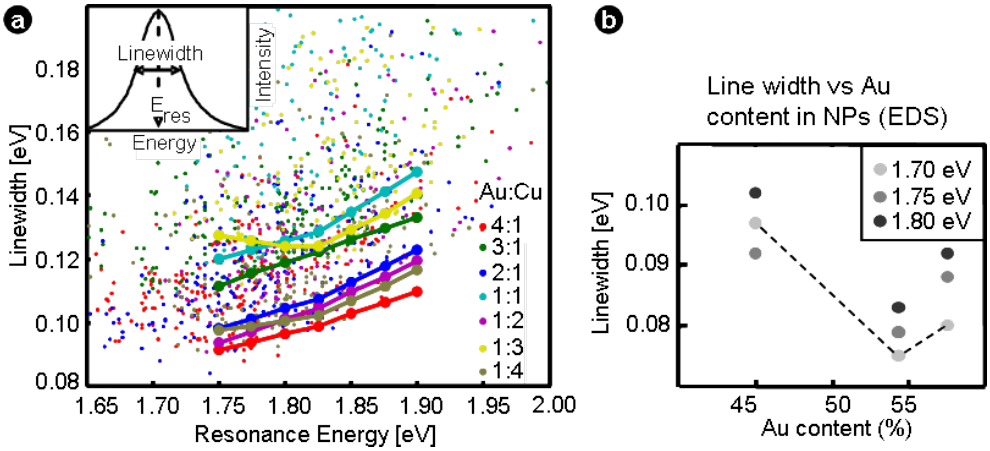

Figure 5.6: a) Single particle line-width (fwhm) versus resonance energy (E_{res}) determined from spectra in a dark-field microscope (inset) for eight samples with Au:Cu ratios in the growth solution of 4:1, 3:1, 2:1, 1:1, 1:2, 1:3, and 1:4 as indicated by the colors. The continuous lines correspond to the minimum line width trend lines of the respective sample (90% lines) due to the intrinsic damping of the material. We observe a general increase of line-width with increasing resonance energy due to stronger interband damping from d-band electrons at higher energies. b) Single particle plasmon linewidth vs. measured Au content at different resonance energies. (Figure taken from [Henkel et al., 2009].)

5.3.3.3 Influence of Copper on Single Particle Plasmon Resonance Linewidth

In order to search for an influence of the varying material composition of the AuCu particles on plasmon damping, we investigated the samples with single particle dark-field spectroscopy. The spectral line-width (fwhm) determined from single particles (homogeneous line-width) is directly related to the plasmon damping. For single crystalline nanorods of the sizes found in this study, the main plasmon damping mechanism is through electronic excitations within the conduction band caused by electron-electron collisions (intraband damping) [Sönnichsen et al., 2002]. Interband excitations (from the d-band to the conduction band) require a threshold-energy (about 2 eV for gold and copper). It is therefore useful to plot the plasmon line-width against the resonance energy when comparing samples (Figure 5.6a). Since many processes (imperfections in the crystal, the surface quality, aggregations, strongly bound chemical surface contaminations) lead to additional damping in some particles, we expect a range of linewidths for any given resonance energy. The lower bound of this range, represented by the 90/10 median, is characteristic for the material. We indicate those lower bounds with lines in Figure 5.6a and observe a general increase of damping for higher resonance energies (as expected from increased interband damping). There is a significant difference between the samples. At Au:Cu ratios of 4:1, 2:1, 1:2, and 1:4 (referring to the concentrations of the precursors in the growth solution), the linewidth is lower than the line width at the ratios of 3:1, 1:1, and 1:3. For another series of samples, we checked the precise elemental composition with EDS and found a local minimum in line-width at Au content of 54% (Figure 5.6b) regardless of the resonance energy. Previous experimental [Linde & J.O., 1936] and theoretical [Banhart & Czycholl, 2002] reports found high DC electrical conductivity for Au:Cu ratios of 1:1 (50% Au) and 1:3 (25% Au). The intraband plasmon damping is, within the Drude theory, proportional to the DC conductivity (see Equation 2.33). Even though a direct comparison of DC conductivity and damping at optical frequencies is not possible, these previous DC reports on copper-gold alloys make our optical results plausible, if we assume that the strong light fields in the dark-field microscope induced the formation of an ordered stoichiometric gold-copper alloy.

5.4 Summary

The evidence we gathered about the rod-shaped particles formed in a gold-copper mixture conclusively shows the presence of a gold-copper alloy. The particles have unique spectral characteristics, shapes, crystal structures, EDS spectra and plasmon damping strength. The copper content allows us to control the two important plasmon properties: resonance position and line-width. We find red shift of the resonance wavelength with increasing copper content up to Ag:Cu = 1:1 and reduced intraband damping at specific copper contents. We find that the more flat slope of the real part of the dielectric function for disordered copper can explain the red shift of the longitudinal plasmon within the uncertainity that is prevalent regarding the electronic structure of disordered metallic alloys. The successful formation of alloyed nanocrystals from solution with coprecipitation while preserving the shape control will be useful for other metal particle synthesis.

Chapter 6

Optimal Aspect Ratio of Gold Nanorods for Plasmonic Sensing

6.1 Introduction

Gold nanoparticles have a long history as optical or electron microscopy labels. More recently, their plasmon resonance has been employed for more elaborate optical nanoscopic sensing schemes. The plasmon resonance of coupled particles depends on interparticle distance [[Jain et al., 2007, Sönnichsen & Alivisatos, 2005, Wang & Pedersen, 2009] and the strong plasmonc light scattering efficiency allows for the visualization of single nanorods, for example for orientation sensing [**?**, Bingham et al., 2009, Pierrat et al., 2009, Schubert et al., 2008]. Furthermore, the resonance position is influenced by the particle charge [Novo et al., 2008, Carbone et al., 2009] and the refractive index of the particle's immediate environment [Perez-Juste et al., 2005]. The plasmonic sensitivity to the immediate dielectric environment of the particles allows one to monitor the dielectric constant of liquids and binding events of molecules to the gold particle surface. Here, the nanoparticle sensor acts in a way similar to sensors exploiting the surface plasmon resonance (SPR) on gold films, which is a standard method in many laboratories. However, whereas the detection scheme for surface plasmon resonance is usually a shift in the plasmon excitation angle [Homola et al., 1999], plasmonic nanoparticles show a shift in the plasmon resonance frequency [Sönnichsen et al., 2000]. The main advantage of using nanoscopic particles as sensors instead of metal films is their extremely small size which allows one, in principle, to measure analytes in volumes as small as attoliters [Raschke et al., 2003]. The key factor for taking advantage of the small detection volume of plasmonic particles is the single particle plasmon scattering spectroscopy [Sönnichsen et al., 2000, Sönnichsen et al., 2002]. Single particle measurements probe the local environment around one specific particle, which – in principle – enables massive parallelization of nanoparticle plasmon sensors either for analyzing different analytes or obtaining statistics. Recently, we demonstrated a scheme that can conduct parallel sensing on randomly arranged nanoparticles using a liquid crystal device as an electronically addressable entrance shutter for an imaging spectrometer [Becker et al., 2007]. For such dielectric plasmon nanoparticle sensors, one hopes to have a large spectral shift for a given amount of analyte or refractive index change of the environment. Initially, spherical gold particles were used [Raschke et al., 2003, McFarland & Van Duyne, 2003] but were soon replaced by gold nanorods [Baciu et al., 2008] due to their higher sensitivity on refractive index changes [Lee & El-Sayed, 2006]. A lot of effort has been applied towards identifying the ideal plasmon sensor with a large spectral shift for a given change in refractive index, for example, using rod shaped gold

nano rattles [Khalavka et al., 2009], meta materials [Liu et al., 2009], silver coated gold nanorods [Becker et al., 2008] and others. However, rod-shaped nanoparticles remain popular for plasmonic applications. Some reasons for this are: the ability to fabricate gold nanorods in high quality using seeded crystallization from solution, the adjustability of the plasmon resonance by varying the aspect ratio, the strong scattering efficiency, and the low plasmon damping in nanorods.

Here, by means of simulations and experiments, we investigate which aspect ratio (AR) of gold nanorods is ideal for plasmonic sensing by employing various measures for 'ideal' behavior. There are several different quantities that describe the performance of a plasmonic structure for sensing applications on a single particle level – and all of them have their merits for certain applications. We will discuss the most important of them in the following paragraphs – the plasmonic sensitivity to refractive index change as well as various 'figures of merit' – and present their dependency on nanorods' geometry from calculations for spherically capped gold rods with the Boundary Element Method (BEM) [Hohenester & Krenn, 2005, de Abajo & Howie, 2002]. We confirm the identified trends by experimental results obtained using single particle dark-field scattering spectroscopy.

6.2 Plasmon Sensor Quality

Changing the refractive index n of the embedding medium by a given amount dn shifts the plasmon resonance position in wavelength or energy units (λ_{res}, E_{res}, respectively, see Figure 1a). The corresponding proportionality constant or sensitivity S (often simply denoted $\Delta\lambda/RIU$, RIU = refractive index unit) can be expressed in wavelength (S_λ) or energy (S_E) units [Burgin et al., 2008]: $S_\lambda = d\lambda/dn$ and $S_E = dE/dn = -S_\lambda/\lambda^2 \cdot 1240\,[nm/eV]$.

6.2.1 Definition of FOM and FOM* and FOM*$_{\mathbf{layer}}$

The relatively broad plasmon linewidth Γ (full width at half maximum) complicates the analysis further, because the plasmon linewidth of nanostructures with different geometries can vary more than tenfold. Since it is easier to detect a given resonance shift for narrow lines, the resonance shift relative to the linewidth is a more meaningful measure of the sensoric quality. This dimensionless quantity is often referred to as the 'figure of merit' $FOM = S/\Gamma$.

The FOM is easily determined experimentally and allows for the comparison of the plasmonic properties of many different structures with a single sharp plasmonic resonance. For more complex plasmonic responses (such as in metamaterial structures based on an analog of electromagnetically induced transparency (EIT) [Liu et al., 2009]), where the plasmon resonance does not follow a simple Lorentz peak shape, the concept needs to be refined. In practice, one would normally detect a spectral shift of a resonance as a relative intensity change dI/I at a fixed wavelength λ_0 induced by a small index change dn. We can therefore define an alternative dimensionless figure of merit:

$$FOM^* = \left(\frac{1}{I}\cdot\frac{dI}{dn}\right)_{max} = \left(\frac{S_\lambda}{I}\cdot\frac{dI}{d\lambda}\right)_{max} \tag{6.1}$$

The wavelength λ_0 is chosen such that FOM^* has a maximum value—for gold nanorods in the shoulder of the resonance of the long-axis plasmon near the place where the slope $dI/d\lambda$ is highest.

Bio-sensing applications are even more complex. In this case, one seeks to detect the binding of small (organic) molecules to the nanoparticle surface instead of exchanging the entire embedding medium. The spectral shift now depends on the relative size of the molecules to the volume the plasmon field penetrates into the medium. Furthermore, the sensitivity is reduced with increasing distance to the particles surface. A 'figure of merit' trying to capture the different sensing volumes

Quantity	Definition	AR_{opt}	Max value
S_λ	$d\lambda_{res}/dn$	∞	
S_E	dE_{res}/dn	3.0 (4.4)	0.85 eV/RIU
FOM	$S_\lambda/\Gamma_\lambda = S_E/\Gamma_E$	4.3 (3.2)	11.1 (10.9)
FOM^*	$\left(\frac{1}{I}\cdot\frac{dI}{dn}\right)_{max}$	4.2 (3.1)	24 (23)
FOM^*_{layer}	$\lim_{l\to 0}\left(\frac{1}{I}\cdot\frac{dI}{dl}\right)_{max}$	3.0 (4.3)	0.57 $/nm$

Table 6.1: Summary of the different quantities describing the quality of plasmon sensors regarding their ability to detect changes in their environment: sensitivity S_λ and S_E in wavelength and energy units, the figures of merit as classical definition (FOM), in generalized form (FOM^*), and for thin layers (FOM^*_{layer}). The last columns list the optimal aspect ratio AR_{opt} (the value in bracket corresponds to the second maximum) for gold nanorods with 20 nm diameter in an aqueous environment and the value of the corresponding quantity at the maximum

of various nanostructures can be defined as the FOM^*_{layer} for a homogeneous coating of molecules with a specific refractive index (for example, n=1.5, typical for organic molecules) in a layer of thickness l around the particle normalized to this layer thickness. The formal definition of this 'figure of merit for thin layers' FOM^*_{layer} is therefore:

$$FOM^*_{layer} = \left(\frac{1}{I}\cdot\frac{dI}{dl}\right)_{max} \tag{6.2}$$

To compare the general sensing quality of different nanostructures, the limit of FOM^*_{layer} for l→0 gives a defined value. Table 6.1 summarizes the different quantities used to determine the quality of plasmon sensors and their definitions.

6.2.2 Plasmonic Sensitivity, FOM, FOM* and FOM*$_{layer}$ Simulation

We simulate the light scattering cross-sections of gold nanorods by solving Maxwell's equations using the BEM and tabulated optical constants for gold [Johnson & Christy, 1972]. Regarding shape, we use rods with spherical end-caps varying the particle length while keeping the diameter constant at 20 nm. Even though the exact end-cap geometry influences the resonance position [Prescott & Mulvaney, 2006], many researchers have successfully used spherical end-caps for their simulations [Bryant et al., 2008]. We vary the aspect ratio by changing only the particle length because gold nanoparticle synthesis usually results in particles of comparable width. From the BEM calculations, we find a linear relationship between aspect ratio AR and plasmon resonance wavelength: $\lambda_{res}/nm = 391 + 114\cdot AR$. The calculations of the layer effect for FOM^*_{layer} were performed within the quasi-static approximation (QSA) for spheroids since we did not implement coated particles in our BEM simulations so far. However, comparisons of QSA with full solutions for the Maxwell equations have shown good qualitative agreement [Prescott & Mulvaney, 2006].

The plasmon sensitivity in wavelength units S_λ(calculated with BEM) shows the expected steady increase for an increasing aspect ratio [Lee & El-Sayed, 2006] (not shown here), whereas the sensitivity in energy units S_E shows a maximum at an aspect ratio of $AR_{max} = 3$ (Figure 6.1). Both the 'classical' FOM and the more general FOM^* show the same trend with two maxima (Figure 6.2a). The classical FOM has a maximum for rods with an aspect ratio of $AR = 4.3$ and a second local maximum at $AR = 3.2$. The maxima of the generalized FOM^* is slightly shifted to rod aspect ratios of $AR = 4.2/3.1$ (cf. Table 6.1). The values of the 'figure of merit for small layers' FOM^*_{layer} (obtained by QSA calculations) are shown in Figure 6.2b for increasing layer

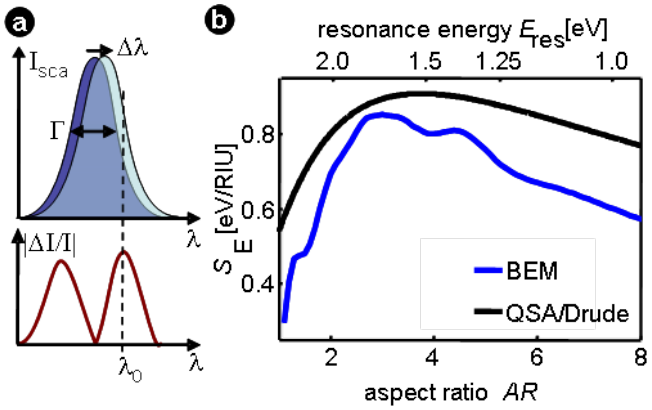

Figure 6.1: a) The plasmon resonance shifts ($\Delta\lambda$) upon changing the refractive index of the surrounding medium by Δn. To detect such changes, the sensitivity $S_\lambda = \Delta\lambda/\Delta n$ needs to be large. Other important parameters that characterize plasmonic sensors are the plasmon linewidth Γ and the wavelength λ_0 where the relative intensity change $|\Delta I/I|$ is largest (see text). b) The plasmonic sensitivity in energy units S_E shows a maximum for gold nanorods with aspect ratio $AR = 3.0$. The blue line shows data calculated with the BEM, assuming gold rods with a diameter of 20 nm and spherical end-caps embedded in water ($n = 1.33$). A similar trend is found for a simple calculation using the quasi static approximation (QSA) and a Drude dielectric function for gold (black line). (Image taken from [Becker et al., 2010].)

thickness l and show maxima at the aspect ratios of $AR = 3.0$ and $AR = 4.3$. The first maximum at $AR = 3.0$ is higher for thin layers and in the limit of layer thickness $l \to 0$. Hence, rods with aspect ratios in the range of 3 to 4 are the best candidates to investigate changes in the refractive index of the embedding medium.

6.2.3 Experimental determination of FOM and FOM* and FOM*$_{\text{layer}}$ for Gold Nanorods

To verify the theoretical conclusions given above, we compared the theoretical results with experimental values measured on single particles. The particle spectra were obtained for nanorods immobilized in a flow cell and exposed to liquids with various refractive indices in a dark field microscope coupled with an imaging spectrometer [Sönnichsen et al., 2002, Becker et al., 2007]. The resulting values are shown in Figure 6.3 and show the same trend as predicted by the BEM simulations. The values are generally lower than the calculated values due to the influence of the supporting glass substrate and are potentially also influenced by a thin organic coating of the particles remaining from the synthesis. The variance within the experimental results is not a measurement error but originates from small derivations from the ideal particle geometry and environment. For example, defects in the nanoparticles' crystal structure would increase damping, therefore broadening the plasmon resonance and reducing FOM and FOM^*.

6.2.4 Theoretical Explanation of the Observed Trends

The existence of a maximum of the plasmon sensitivity in energy units as a function of the aspect ratio can be derived from a simple calculation of the polarizability of a spheroid in quasi-static approximation: The polarizability α of a spheroid within the quasi-static approximation is given

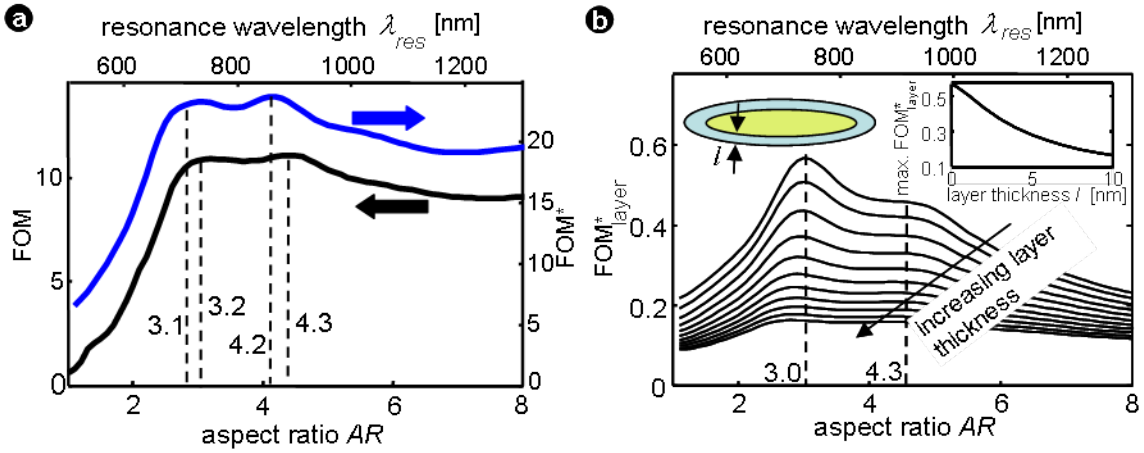

Figure 6.2: To identify the optimal aspect ratio for plasmon sensing, various 'figure of merits' (FOM) are calculated: a) The classical FOM defined as plasmon sensitivity S divided by plasmon linewidth Γ (left axis) is compared to a generalized FOM^* defined as the maximal relative intensity change $|\Delta I/I|$ for a small refractive index change Δn (right axis). While the classical figure of merit FOM has a maximum for an aspect ratio of $AR = 4.3$ and a second maximum at $AR = 3.2$, the generalized FOM^* has its maximum at $AR = 4.2$ with its second local maximum at $AR = 3.1$. b) The FOM^*_{layer} takes into account the sensing volume by considering the plasmon change induced by a small layer around the particle normalized to the layer thickness ($0.01nm < l < 10nm$ in 1 nm steps). The plasmon sensing quality FOM^*_{layer} decreases with increasing layer thickness (inset) and shows a maximum value of $FOM^*_{layer} = 0.55$ for $d \to 0$ at an aspect ratio $AR = 3.0$. Data for (a) are calculated by BEM for gold nanorods with spherical end-caps and 20 nm diameter, data for (b) within the quasi static approximation QSA for spheroids. (Image taken from [Becker et al., 2010].)

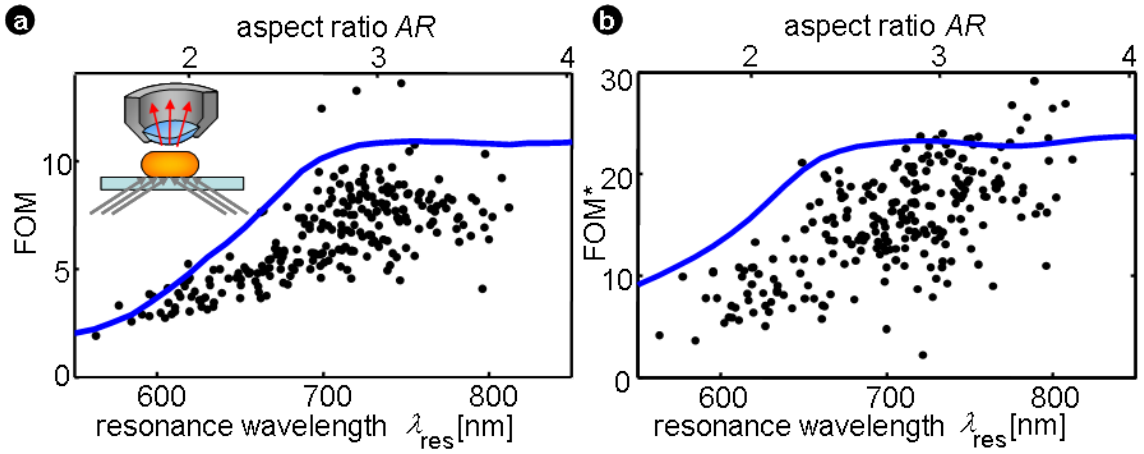

Figure 6.3: Experimental data (each black dot represents one single particle) for the figures of merit FOM(a) and FOM^* (b) obtained by single particle spectroscopy in a dark field microscope (inset). The absolute values are slightly lower than the theoretical prediction (blue line) due to the attachment of the gold rods to a glass substrate which limits the accessible surface (inset). (Image taken from [Becker et al., 2010].)

by (see Chapter 2.2.2):

$$\alpha = V\epsilon_0 \frac{\epsilon_r(\lambda) - 1}{1 + L(\epsilon_r(\lambda) - 1)} \tag{6.3}$$

Where V is the volume, $\epsilon_r(\lambda) = \epsilon_{NP}(\lambda)/\epsilon_m$ is the relative dielectric function with $\epsilon_{NP}(\lambda)$ the wavelength (frequency) dependent dielectric function of the nanoparticle and ϵ_m the dielectric constant of the surrounding medium, which is water. Water has a constant dielectric function in the visible range. The parameter L is the shape dependent depolarization factor (as introduced in Chapter 2.2.2, equation ??) which has values between 0 and 1: $0 \leq L \leq 1$. The exact equation for L is given by [Osborn, 1945]:

$$L = \frac{1}{AR^2 - 1} \cdot \left[\frac{AR}{2 \cdot (AR^2 - 1)^{1/2}} \cdot \ln\left(\frac{AR + (AR^2 - 1)^{1/2}}{AR - (AR^2 - 1)^{1/2}} \right) - 1 \right] \tag{6.4}$$

For $AR < 8$, this formula can be simplified to (see also expression 2.52 in Chapter 2.2.2) :

$$L = (1 + AR)^{-1.6} \tag{6.5}$$

with an error of $<5\%$ [Sönnichsen, 2001]. Equating the real part of the denominator of Equation 6.3 to zero to fulfill the resonance condition ($\alpha \to \infty$) and using the Drude model to describe the dielectric function of the particle ($Re(\varepsilon) \approx \varepsilon_\infty - \omega_p{}^2/\omega^2$ [Sönnichsen, 2001]) we can express the resonance position E_{res}:

$$E_{res} = \frac{\omega_p}{\sqrt{\epsilon_\infty + n^2 \cdot (1/L - 1)}} \tag{6.6}$$

In order to get the plasmon sensitivity S_E we take the derivative of 6.6 with respect to n:

$$S_E = \frac{dE}{dn} = -\frac{\omega_p n (1/L - 1)}{[\epsilon_\infty + n^2 \cdot (1/L - 1)]^{3/2}} \tag{6.7}$$

To find the maximum sensitivity $S_E(AR)$ as function of the aspect ratio, we need to perform another differentiaion, this time with respect to L, knowing that the depolarization factor is dependent on the aspect ratio (see equation 6.5):

$$\frac{d}{dL} S_E = \frac{\omega_p n \left[\epsilon_\infty - \frac{1}{2} n^2 (1/L - 1)\right]}{L^2 \cdot [\epsilon_\infty + n^2 (1/L - 1)]^{5/2}} \tag{6.8}$$

and we have to set 6.8 equal to zero and solve it for L. Then using 6.5 we can calculate the optimal aspect ratio AR_{max}, at which the sensitvity $S_E(AR)$ reaches its maximum:

$$AR_{max} = \left(\frac{n^2}{n^2 + 2\epsilon_\infty} \right)^{-1/1.6} - 1 \tag{6.9}$$

where, ω_p and ε_∞ are the plasma frequency of the conduction electrons (9 eV for gold [Lambrecht et al., 2007]]) and the polarizability of the bound electrons (9.84 for gold [Cao et al., 2009]), respectively, and $n = (\varepsilon_{medium})^{1/2}$ the surrounding medium's refractive index.

The agreement of these simple calculations with the BEM calculations is surprisingly good (Figure 6.1, black lines) since the quasi-static approximation is only valid for spheroid shaped particles much smaller than the wavelength of the incident light. The particles we investigate are neither spheroids nor much smaller than the light wavelength (only a factor of up to 5). Our BEM

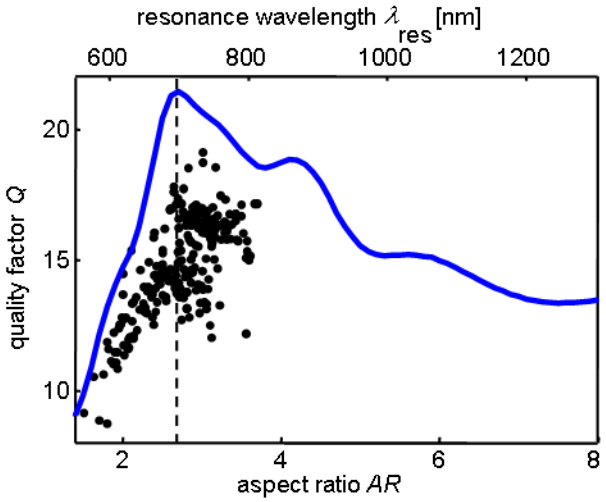

Figure 6.4: The quality factor Q (determined via $Q = E_{res}/\Gamma$) shows a maximum for rods with an aspect ratio of approximately $AR = 3$ and decreases for larger aspect ratios. The blue line represents the results obtained by BEM calculations, while the black dots correspond to measurements on single gold nanorods. (Figure taken from [Becker et al., 2010].)

calculations using spherically capped cylinders model the real particle shape more realistically and correctly take the particles' absolute size into account.

Interestingly, the aspect ratio with the highest plasmon sensitivity in energy units AR_{max} depends on the polarizability of the inner electrons of the metal ε_∞ and the refractive index of the medium. For water ($n = 1.33$) as a medium, the optimal aspect ratio becomes $AR_{max} = 3.8$. Since the Drude model does not include the contribution of interband damping to the imaginary part of the dielectric function, we conclude that the maximum in plasmonic sensitivity S_E is not caused by the effect of those interband excitations.

6.2.5 Influence of the Q-Factor on FOM and FOM* and FOM*$_{\text{layer}}$

Yet, what is the reason for the 'optimal aspect ratio' for the three 'figures of merit' introduced in Chapter 6.2.1? We believe the quality factor Q is the key quantity in explaining this behavior. The quality factor of an oscillation describes the number of oscillations until the oscillation is damped. We find it plausible that a longer plasmon oscillation lifetime (i.e., a higher quality factor) results in a more sensitive dependency on changes in the surroundings. For a classical-driven harmonic oscillator, the resonance frequency divided by the linewidth of the resonance Γ gives the quality factor $Q = E_{res}/\Gamma$. Figure 6.4 shows the quality factor as a function of the aspect ratio for gold nanorods (calculated by the BEM and measured experimentally on single particles). Evidently, a maximum is found around $AR = 3$. The initial rise from $Q(AR = 1) = 8$ to $Q(AR = 3) = 22$ is easily explained considering the reduced plasmon damping as the resonance shifts to lower energies with an increasing aspect ratio [Sönnichsen et al., 2002]. The slow decrease above the aspect ratio of 3 is due to the decreasing resonance frequency divided by the (more or less) constant Drude damping.

6.3 Summary

In summary, for the four measures for an 'optimal plasmonic sensor', namely sensitivity S, figure of merit FOM, generalized figure of merit FOM^*, and figure of merit for thin layers FOM^*_{layer}, there is an optimum aspect ratio around 3-4, where gold nanorods show the best sensitivity. Only the plasmon sensitivity in wavelength units S_λ increases steadily with aspect ratio. Even though

gold nanorods show very strong plasmon resonances with high quality factors and are, at the same time, small in volume, we don't want to exclude that other shapes of metal structures (bi-pyramids, rattles, pairs of particles, EIT structures, etc) are even better plasmon sensors. We hope that our new definition of a generalized figure of merit and the corresponding generalized figure of merit for small layers will trigger the comparison of plasmon sensor quality of many more complicated metal structures.

Chapter 7

Highly Sensitive Silver Nanorods

7.1 Introduction

Sensor devices based on the refractive index sensitivity of surface plasmons have emerged on the market in the last decade. Attempts to increase the sensitivity and reduce the sensor size focus on single particle based sensors supporting localized surface plasmons polaritons (LSPP) or particle plasmons.[Baciu et al., 2008, Mayer et al., 2010, Wu & Xu, 2009] As recently reported, single particle sensors can have a better sensitivity than propagating surface plasmon based sensors.[Otte et al., 2010] The spectral position of the localized surface plasmon is highly dependent on the dielectric properties of the surrounding medium.[Kelly et al., 2003] For example, a change of the surrounding refractive index of 0.02 from 1.333 to 1.353 results in a red shift of the resonance wavelength by $5.1nm$ for a gold nanorod with an aspect ratio of 2.5. For optimal sensing of smallest dielectric changes (i.e. binding of single molecules), the spectral shift of the resonance wavelength upon changing the surrounding medium has to be maximized. Increasing the spectral shift can be achieved by various methods like: optimizing the shape and size,[Becker et al., 2010, Khalavka et al., 2009, Mahmoud & El-Sayed, 2010, Liz-Marzan, 2006] inter-particle distance[Wang & Reinhard, 2009, Jain & El-Sayed, 2008] or the material of the particle.[Liz-Marzan, 2006, Ringe et al., 2010] In recent times, efforts have been intensified to investigate silver nanoparticle sensitivity.[Wei et al., 2010, Malinsky et al., 2001] Silver and gold nanotriangle sensitivities of self assembled monolayers have been reported earlier[Haes & Van Duyne, 2004], but due to different monolayer thicknesses the differing sensitivities could not be attributed to optical properties of the metals. In this work, we present experimental results of single silver nanorod and gold nanorod sensitivities revealing that silver nanorods have a larger sensitivity than gold nanorods at the same resonance wavelength and that – contrary to earlier predictions[Lee & El-Sayed, 2006] – the background polarizability of the d-band electrons strongly influences the sensitivity. We provide a theoretical discussion of the differing sensitivities based on medium long wavelength approximation (MLWA)[Kelly et al., 2003, MEIER & WOKAUN, 1983] to account for size dependent effects. Finally a simplification offered by quasi static approximation (QSA) leads to an elegant formulation of sensitivity as function of resonance wavelength position, plasmonic material parameters and the refractive index of the embedding medium.

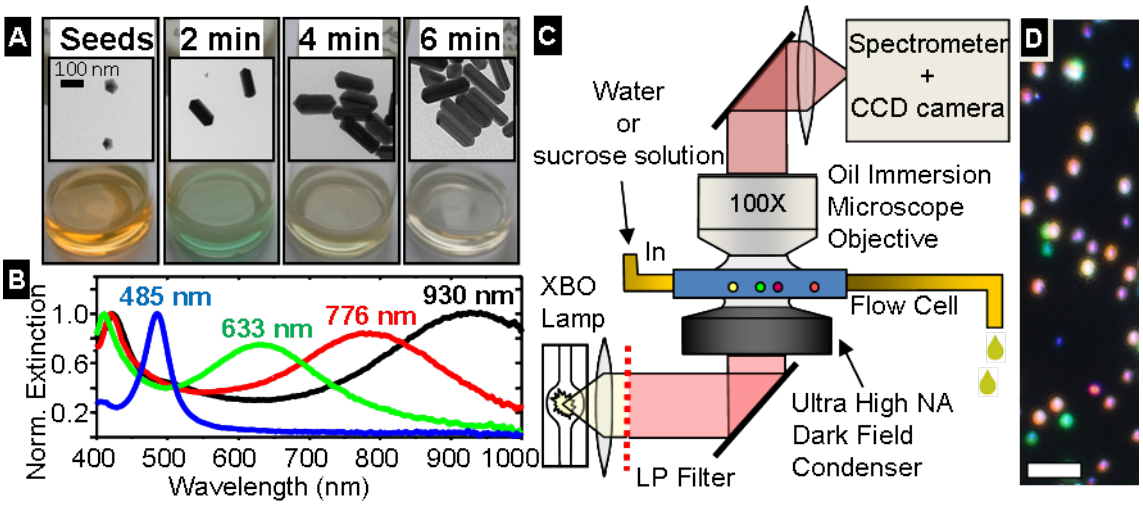

Figure 7.1: A: Representative silver nanorod samples are shown as photographs and TEM images together withthe corresponding ensemble extinction spectra (B). The samples correspond to: Ag-seeds and Ag-nanorods grown with 2, 4, and 6 minutes of heating time (from left to right). Their plasmon peak increases from 485nm to 633nm, 776nm, and 930nm. C: Experimental wet environment dark field setup designed for single nanoparticle spectroscopy in various surrounding media. D: Typical dark-field image of the nanoparticles, the scale bar is 10µm.

7.2 Synthesis

For our study, we form silver nanorods with various aspect ratios in solution adapting a two-step "seeded growth" approach developed by Kitaev et al. [Pietrobon et al., 2009] with small modifications in illumination and heating. In the first step, faceted silver "seeds" are produced under light illumination. We use a blue LED lamp (141mW, peak maximum @ 459.5nm, full-width-at-half-maximum (FWHM) 20.53nm) instead of the high power metal halide lamp used by Kitaev and co-workers. In the second step, the seeds are added to a "growth solution" where they develop into silver nanorods. We preheat the growth solution in a consumer microwave at 90W for 1 minute. Then AgNO3 is added and the solution is placed into the microwave again for heating between 2 and 6 minutes resulting in rods with increasing aspect ratio (AR). Two minutes of heating result in rods with an aspect ratio of 2.4 ± 0.8, four minutes yield an aspect ratio of 2.9 ± 1.3, and six minutes an aspect ratio of 4.0 ± 1.6. (Figure 1, top). We compare the plasmonic sensitivity of those silver rods with two types of gold nanorods with different widths. The nanrods with small widths were synthesized by the method of Nikoobakht et al. [Nikoobakht & El-Sayed, 2003], the ones with the large thickness by the method of Ni et al..[Ni et al., 2008] The thick gold nanorods have the advantage that their widths are comparable with the silver nanorods.

7.3 Plasmonic nanorod sensitivity

We observe the light scattering spectra of the single nanoparticles with a scanning dark-field setup [Carbone et al., 2009] (see Chapter 3 for more details of the microscopic setup) that allows for a rapid measurement of a large number of immobilized nanoparticles (Figure 7.1C).

Material	Longitudinal ens. peak (nm)	Width (nm)	Aspect Ratio
Ag	633	55 ± 10	2.4 ± 0.7
Ag	776	59 ± 14	2.9 ± 1.0
Au	634	28 ± 4	2.0 ± 0.5
Au	702	18 ± 2	2.7 ± 0.5
Au (disregarded)	743	18 ± 3	3.1 ± 0.8
Au	816	11 ± 2	4.1 ± 1.4
Au	680	50 ± 6	2.1 ± 0.5

Table 7.1: Dimensional characterization of the silver and gold nanorods used in our study (sizes from TEM images). The small Au NRs with ensemble peak @ $743nm$ were disregarded from the sensitivity analysis due to their irregular rod shapes and very flat end-caps.

Flow Cell Preparation

To measure the plasmon resonance shift upon changes in the refractive index of the environment (single particle sensitivity), the nanoparticles are immobilized in a flat glass capillary or flow cell (Figure A.1). The glass capillary (Vitrotube W5010-100 by Vitrocom) is initially UV-irradiated for 15 minutes and left for another 15 minutes in the reactive atmosphere, then we attach thin polyethylene tubing using epoxy glue to construct the flow cell system. The flow cell is purged with 1% Helmanex solution for 24 hours, and finally cleaned with hot deionized water for 1 hour.

Immobilization

To immobilize nanoparticles in the flow cell, we add a suspension of nanoparticles in water followed by a salt solution. The concentration of nanoparticles is adjusted by dilution to create a nanoparticle density in the field-of-view that allows the distinction of single particles (Figure 7.1D); i.e. an average inter-particle distance of about $10\mu m$. The addition of salt screens the surface charges that stabilize the nanoparticle suspension, which leads to nonspecific adsorption of nanoparticles to the glass surface of the flow cell. For gold nanorods, we used $0.1M\ NaCl$, for silver $0.1M\ KNO_3$ because, as discussed later, chloride ions can cause structural changes to silver nanoparticles. To avoid aggregation, both liquids are separated in the source tube by a tiny air bubble that gets trapped in the entrance chamber of the flow cell thus the mixing takes only place in the flow cell.

Table 7.1summarizes the size characteristics of the nanorods used for single particle spectroscopic measurements. We used only silver nanorods from samples with mean longitudinal plasmon resonances of $633nm$ and $776nm$ (green and red curves in 7.1B). Those silver nanorods had a mean width of about $55 - 60nm$ and aspect ratios of 2.4 : 1 and 2.9 : 1, respectively. In comparison, the small gold nanorods have widths of $11 - 28nm$ but with comparable aspect ratios, and the thick gold nanorods have widths of $50nm$. The endcap of the silver nanorods is a pentagon based pyramid with a rather flat tip angle (Figure 7.1A), the end cap of the gold nanorods (regardless of size) is spherical or flattened spherical (7.2 and 7.3).

7.3.1 Sensitivity measurements

The plasmon sensitivity quantifies the dependence of the plasmon resonance wavelength or frequency on changes in the dielectric properties of the surrounding medium. Sensitivity S (in wavelength units) is therefore defined by $S = d\lambda_{res}/dn$, where λ_{res} is the plasmon resonance wavelength and n is the refractive index of the surrounding medium. There are more elaborate measures to quantify the sensor quality of nanoparticles taking into account more realistic sensor concepts, for

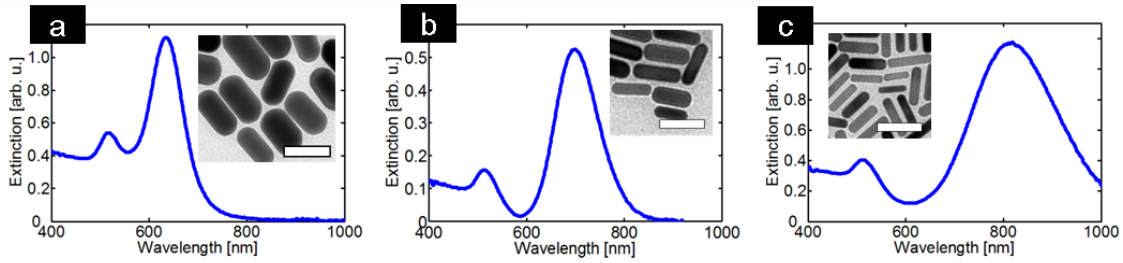

Figure 7.2: TEM images and ensemble absorption spectra of the small gold NRs used to measure the sensitivity. The longitudinal ensemble peak is at (a) $630nm$, (b) $702nm$ and (c) $816nm$. The gold NRs have spherical or slightly flattened endcaps. The scale bars are $50nm$.

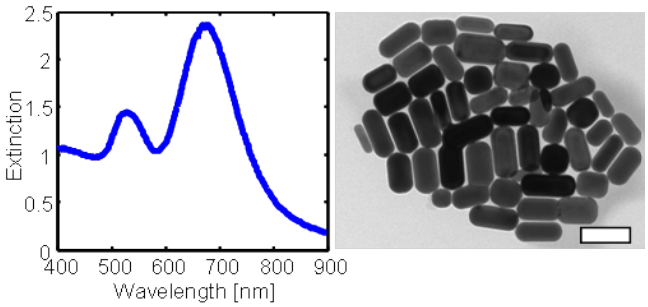

Figure 7.3: TEM images and ensemble absorption spectra of the thick gold NRs used to measure the sensitivity. These gold NRs have lengths of $107 \pm 12nm$, and widths of $50 \pm 6nm$, these dimensions are similar to the silver NR dimensions. The scale bar is $100nm$.

example FOM [Sherry et al., 2005, Unger & Kreiter, 2009], FOM* [Becker et al., 2010]. All of these quantities depend on the plasmon sensitivity. Here we focus on the sensitivity in wavelength units and refer to this term simply as 'sensitivity'.

We determined the plasmonic sensitivity experimentally by recording spectra of single immobilized nanoparticles in the initial environment (pure water, $n_1 = 1.3330$), then immersed in 12.5% sucrose solution ($n_2 = 1.3454$), and at the end again in water. The resulting experimental results are shown in Figure 7.4 (top panel). The experimentally obtained trend-lines (continuous lines) qualitatively follow the trend simulated with the boundary-element-method (BEM) [Hohenester & Krenn, 2005] (dashed lines) but are lower than the simulation. However, the simulation was performed with a homogenous medium around the particles, whereas in the experiment, the particles are attached to a glass substrate reducing the influence of the change in medium. The fact that the experimental silver trend shows a stronger deviation from simulations than the gold nanorods might be caused by additional damping of the plasmon resonance due to their penta-twinned crystal structure [Tang et al., 2006].

Silver sensitivity is higher than gold sensitivity, furthermore thick gold nanorods have a higher sensitivity than the thinner gold nanorods. Conclusively, both material and thickness (diameter) influence the sensitivity. The sensitivity of silver nanorods reaches values above $400nm/RIU$, which is, up to now, the largest value for rod-like objects in this wavelength range [Mahmoud & El-Sayed, 2010]. Especially in the wavelength range of 600 to $700nm$, where thin gold nanorods have only a sensitivity of ca. $170nm/RIU$ and thick gold nanorods have $250nm/RIU$, silver outperforms both group of gold NRs with sensitivities around $340nm/RIU$. Due to the lack of thick gold nanorods with larger aspect ratios, we measured the sensitivity of the thick gold nanorods only up to $710nm$. We believe that the scattering of the data points around the trend lines is primarily caused by the varying thicknesses of the particles and the surface stabilizing layer (Ag: PVP, Au: CTAB) around the particles.

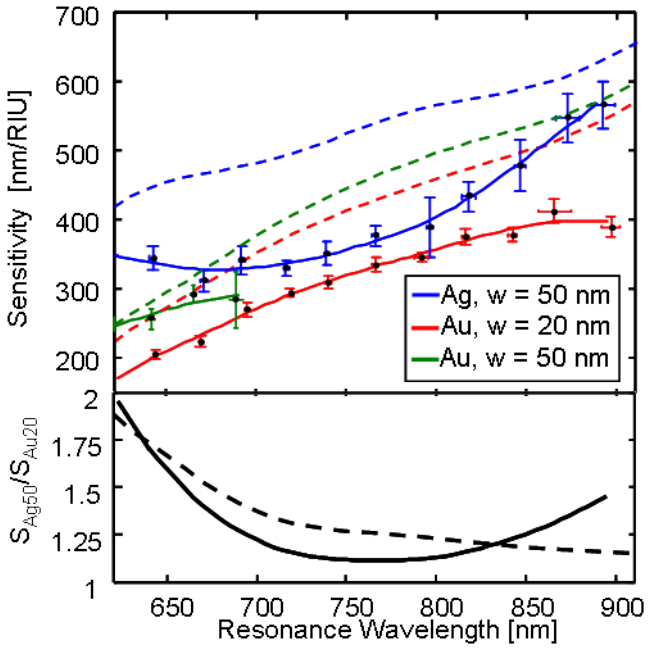

Figure 7.4: *Top:* Experimental results (continuous lines) and BEM-simulation without substrate (dashed lines) of single particle sensitivity of silver (blue), thin (red) and thick (green) nanorods. The error bars indicate the uncertainity of the mean in a range of 25 nm. Bottom: the experimentally obtained (continuous line) and BEM-simulated (dashed line) sensitivity enhancement (S_{Ag}/S_{Au}) of silver nanorods with 50 nm thickness in relation to gold nanorods with 20 nm thickness.

To directly compare the sensitivity of thin gold (ca. 20 nm thickness) and silver nanorods over the entire measured spectral range, we show the ratio of their sensitivity (the sensitivity enhancement of silver compared to gold S_{Ag}/S_{Au}) in the bottom plot of Figure 7.4, both for the experimental data and the simulation. In simulations we use 20nm diameter for the thin gold NRs which is the average of the thicknesses of the thin gold NRs (11 to 28 nm) used in our experiments. The influence of thickness on the plasmonic response (thus the sensitivity) in this range is – as we discuss it later – negligible. Experiment and simulation agree well in this diagram up to $850nm$, the substrate effect effectively cancels out. At shorter wavelengths, around $620nm$, the enhancement reaches a factor of 2, at longer wavelengths the enhancement drops to a value between 1.1 and 1.2 with a slow increase above $850nm$ that is not followed by the simulated results.

7.3.2 Discussion and Model,

Medium long wavelength approximation of plasmonic sensitivity

To understand the origin of the higher plasmonic sensitivity of silver nanorods compared to gold nanorods, we calculated sensitivities with the MLWA [Kelly et al., 2003, MEIER & WOKAUN, 1983]. MLWA includes size dependent effects in plasmon resonance calculations thus allowing us to investigate impacts of size and embedding medium refractive index. We start with the scattering cross-section of a particle that is proportional to the square of the modulus of the polarizability $C_{sca} \sim |\alpha|^2$. The polarizabiliy can be obtained from the Maxwell Equations for the polarization $\mathbf{P} = \alpha\mathbf{E}$. The size dependent polarizability contains the expansions of the Mie coefficients (thus the exact calculation of the Maxwell Equations) to the third order of the wave vector, k with $k = 1/\lambda$. This expansion takes the retarded field of the induced dipole into account. Using the wavelength inside the metal: $\lambda^{'} = \lambda/n^{'}$ with $n^{'} = Re[\tilde{n}]$ where $\tilde{n}$ is the complex refractive index

of the metal, we can express the polarization of the nanoparticle:

$$\mathbf{P} = \alpha\mathbf{E} = \frac{\alpha_0\mathbf{E}}{1 - \alpha_0\left[\frac{1}{b}\left(\frac{n'}{\lambda}\right)^2 - i\frac{2}{3}\left(\frac{n'}{\lambda}\right)^3\right]} \tag{7.1}$$

Where a is the width and b is the length of the NR, and α_0 is the static polarizability expressed as:

$$\alpha_i = V\epsilon_0\frac{\varepsilon_r - 1}{1 + L_i(\varepsilon_r - 1)} \tag{7.2}$$

Where ε_r is the relative $\varepsilon_r = \varepsilon(\omega)/\varepsilon_m$ dielectric function of the particle $\varepsilon(\omega)$ to the embedding medium (ε_m), L is a geometric depolarization form factor that is well approximated by (2.51) $L = (1 + AR)^{-1.6}$ for rods with aspect ratio (AR) between 1 to 8. Inserting the expression of the static polarizability into Equation 7.1 and using $V = \frac{1}{6}\pi a^2 b = \frac{1}{6}\pi a^3 \cdot AR$ for the volume of the ellipsoid, we get:

$$\alpha = \frac{\frac{1}{6}\pi a^3 \cdot AR \cdot (\varepsilon_r - 1)}{1 + (\varepsilon_r - 1)\left[L - \frac{\pi}{3}\left(2\pi\frac{n'a}{\lambda}\right)^2 - i\frac{\pi}{9}\cdot AR\cdot\left(2\pi\frac{n'a}{\lambda}\right)^3\right]} \tag{7.3}$$

It becomes obvious that the corrections reduce the geometric depolarization factor, L. The term $\sim (n'a/\lambda)^2$ is called dynamic depolarization factor and is responsible for the red shift with increasing width (short axis of NR), whereas the imaginary term $\sim (n'a/\lambda)^3$ is causing the additional linewidth broadening with increasing volume. To find the resonance wavelength, we must find the wavelength for which maximum polarizability occurs, the maximum is reached where the real part of the denominator becomes zero:

$$1 + (\varepsilon_r - 1)\left[L - \frac{\pi}{3}\left(2\pi\frac{n'a}{\lambda}\right)^2 - i\frac{\pi}{9}\cdot AR\cdot\left(2\pi\frac{n'a}{\lambda}\right)^3\right] = 0$$

This equation can not be analytically solved for λ to find λ_{res} as a function of the other parameters in the equation (material and geometric parameters). Before we proceed to the numerical solution, we introduce Drude's expression of the dielectric function. Drude's model (Equation 2.35 from Chapter 2.1.2) gives us a concept to separate the influence of the contribution of bound and conduction electrons:

$$\varepsilon(\omega) = \varepsilon_\infty - \frac{\omega_p^2}{\omega^2 + \gamma^2} \tag{7.4}$$

Where ω_p is the plasma frequency ($\hbar\omega_p = 9.1eV$ for both gold and silver), and ε_∞ the background polarizability arising from the bound d-band electrons ($\varepsilon_{\infty,Au} = 9.84$ for gold and $\varepsilon_{\infty,Ag} = 3.7$ for silver). The lower value for background polarizability of silver reflects the deeper lying d-band with an offset to the Fermi-energy of $4eV$ compared to $2eV$ for gold. The damping term, γ has following values $\gamma_{Au} = 67meV$ and $\gamma_{Ag} = 19meV$ [Sönnichsen, 2001]. Due to its small value compared to optical frequencies, the damping term is often omitted for analytic calculations, but we keep it, since it will also contribute to the size dependent red shift of the resonance. In Figure 7.5 we plot the resonance vs. the aspect ratio for 0, 20 and $50nm$ width. The influence of the width on the resonance wavelength is only marginal @ $20nm$, but becomes more prominent @ $50nm$. The width of $0nm$ - as unphysical it may seem – makes sense, since it is a special case that is called the quasi static (QSA) approximation. We will discuss the implications of QSA in the following section.

To calculate the sensitivity we determined sensitivity for the refractive index difference between water (n=1.333) and 12.5% sucrose solution (n=1.3454) and plotted it in Figure 7.5. Although

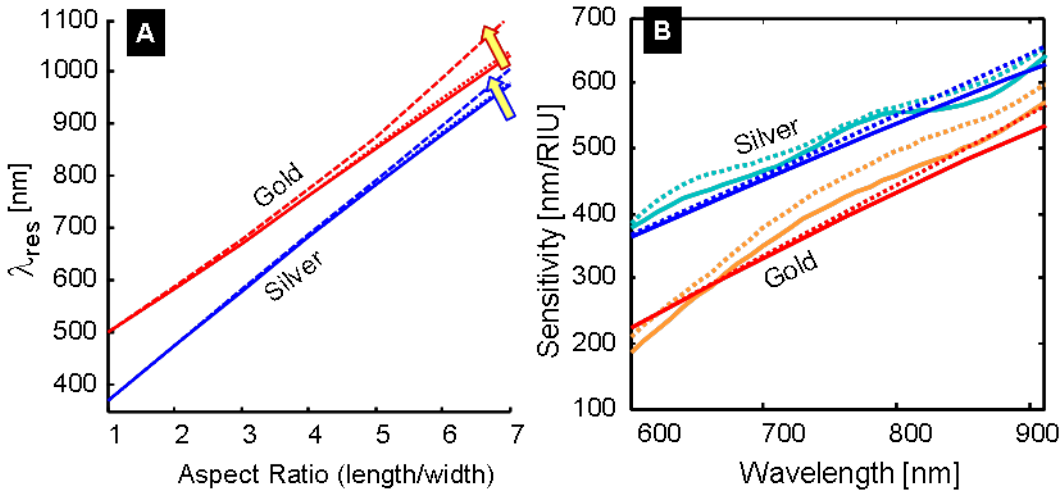

Figure 7.5: *Left:* Resonance wavelength calculated with MLWA as function of the aspect ratio and diameter for gold (red) and silver (blue). The yellow arrows indicate the red shift of λres with increasing width (from 0 over 20 to 50nm). *Right:* Sensitivity of gold and silver vs the resonance wavelength λ_{res} calculated with BEM (gold: orange lines, silver: cyan lines) and MLWA (gold: red lines, silver: blue lines). The continuous lines correspond to a nanoparticle width of 20nm, dotted lines correspond to a width of 50nm. In case of MLWA the sensitivity of nanorods with 20nm widths overlap practically with the sensitivity calculated using the QSA approach of 7.8.

the MLWA curve is following the BEM curve quite well, indicating both the dependency on the resonance wavelength position and on the width of the NRs, there are differences that are mainly rooted in the fact that BEM uses tabulated dielectric function values, and MLWA uses Drude's model. Furthermore MLWA assumes an ellipsoidal NR shape, whereas BEM uses a rod like shape with spherical endcaps that are resembles more to the real shape of the NRs. As the material parameters entered MLWA calculations through Drude's model we can clearly see that due to its higher background polarizability ε_∞, gold sensitivity remains below the silver sensitivity if all other parameters are kept the same.

Simplifying the plasmonic sensitivity equation with quasi-static approximation (QSA)

The quasi-static approximation offers us an elegant simplification that allows a fully analytic derivation of the sensitivity. Within the quasi-static approximation (i.e. for particle dimensions much smaller than the light wavelength in the metal), the dipole's interaction with its own field is neglected thus no retardation effects are taken into account. Similarly like in case of MLWA, the plasmon resonance occurs at the frequency where the real part of the denominator of the polarizability becomes zero. Using Equation 7.4 as the frequency dependent dielectric function for the nanoparticle and inserting it into the resonance condition (denominator in Equation 7.2 is zero) $1 + L(\varepsilon_r - 1) = 0$ we can rearrange it to express ω. This frequency is the resonance frequency from which we can obtain the resonance wavelength $\lambda_{res} = 2\pi c_0/\omega_{res}$. We replace ε_m for practical purposes with the refractive index of the surrounding medium $n = \varepsilon_m^{1/2}$:

$$\lambda_{res} = \lambda_p \sqrt{\varepsilon_\infty + n^2 \left(\frac{1}{L} - 1\right)} \tag{7.5}$$

where $\lambda_p = 2\pi c_0/\omega_p = 136nm$ is the bulk plasmon wavelength with c_0 , the speed of light in vacuum. The curve for NR width of $0nm$ in the left diagramm of Figure 7.5 represents the resonance wavelength obtained with Equation 7.5. Clearly, QSA is applicable for widths of $20nm$ (up to ca. $30nm$) because the overall deviation between the curves of 0 nm and 20 nm is very small.

Since the sensitivity is defined by the change of the resonance wavelength λ_{res} with the surrounding refractive index n, we arrive at the equation for the sensitivity by taking the derivative of 7.5 with trespect to the refcractive index:

$$S = \frac{d}{dn}\lambda_{res} = \frac{\lambda_p n}{\sqrt{n_\infty^2 \left(\frac{L}{1-L}\right)^2 + n^2 \left(\frac{L}{1-L}\right)}} \tag{7.6}$$

where $n_\infty = \varepsilon_\infty^{1/2}$ is the background refractive index. To be able to directly compare the experimental data to the results of the analytic expression in Equation 7.6, we need to express the sensitivity as function of the resonance wavelength. Thus we use Equation 7.5 and rearrange it to express $L/(1-L)$ as function of n_∞ , n, λ_p and λ_{res} we get:

$$\left(\frac{L}{1-L}\right) = n^2 / \left(\frac{\lambda_{res}^2}{\lambda_p^2} - n_\infty^2\right) \tag{7.7}$$

Inserting the right side of 7.7 into 7.6 and writing λ for λ_{res} we get:

$$S(\lambda) = \frac{\lambda}{n} \cdot \left(1 - \frac{\lambda^2}{\lambda_p^2} n_\infty^2\right) \tag{7.8}$$

The sensitivities obtained with Equation 7.8 overlap practically with MLWA's result for 20 nm widths, thus it is not plotted to avoid overcrowding Figure ??B. The equation above reveals that, contrary to earlier reports [Lee & El-Sayed, 2006], the sensitivity depends on the material through the strong difference in the background polarizability ε_∞ of gold and silver (the sensitivity decreases with increasing ε_∞ or n_∞).

Despite the simplifications of the quasi-static approach and the Drude model for the dielectric function, the Equation 7.8 predicts the sensitivity of nanorods remarkably well. Compare the sensitivites calculated with QSA analogous settings of MLWA with the sensitivities for NRs with $20nm$ diameter (dotted lines) obtained with BEM in Figure ??B. Interestingly, in 7.8 all geometry related factors cancel. Consequently, the sensitivity of a plasmonic nanorod at a given wavelength is independent from its size as long the conditions for QSA are valid (e.g. for particles which are thin enough that retardation is negligible, but thick enough that surface damping is not significant – thus particles with widths of 10 to 30 nm) and the formula could be valid more generally for metal structures of other shapes. Our results extend the findings of Miller et al. who found that within the QSA the sensitivity of gold nanoshells depends only on the location of the plasmon resonance peak and the dielectric properties of the involved materials [Miller & Lazarides, 2005].

7.3.3 Sensing Reversibility

Whereas sensitivity alone seems to favor silver over gold, another important aspect for sensors is the sensing reversibility upon repeated changes of the environment. Given the fact that silver is less noble than gold, I carefully checked the reversibility. For this purpose, our measurements always went back to the initial environment at the end and I recorded the difference in resonance

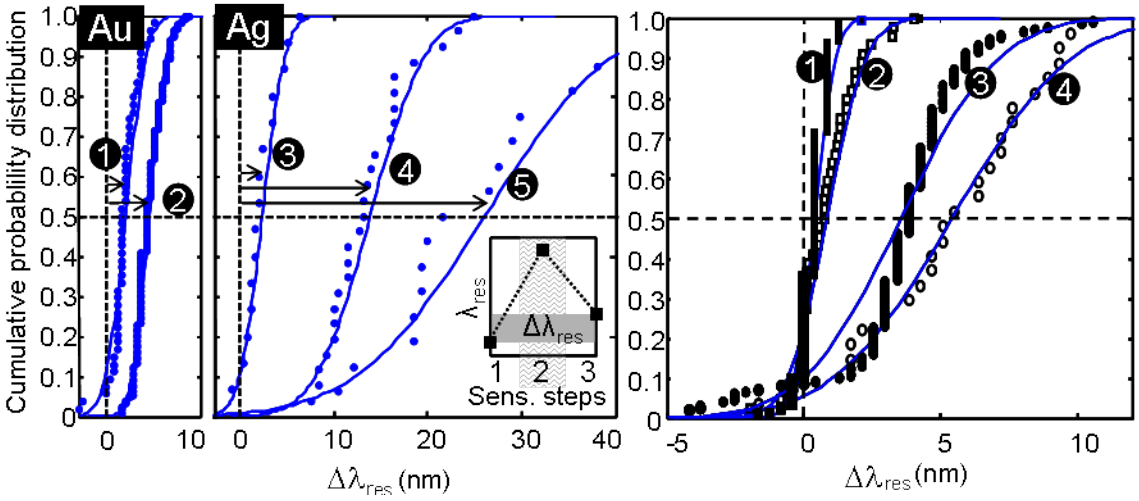

Figure 7.6: *Left:* Cumulative distribution of single nanoparticle resonance wavelength shifts after one sensing measurement cycle (the sensing cycle shift). For clarity I plotted the curves for gold and silver separately. The continuous lines are Gaussian fits, the arrow indicates the mean cycle shift. Left graph: (1) Au rods with $610nm$ long pass (LP) filter (2) Au rods without LP filter. Right graph: (3) Ag rods with $610nm$ LP filter, (4) Ag rods with $530nm$ LP filter (5) Ag rods without LP filter. Inset at bottom right: definition of sensing cycle shift $\Delta\lambda_{res}$ in the cycle $n_1 \rightarrow n_2 \rightarrow n_1$. *Right:* Spectral stability of nanoparticles measured under identical conditions as during sensitivity measurements, except that here the surrounding medium was always water. The graph shows the influence of the long pass filter on the spectral stability of Au and Ag nanoparticles by plotting the cumulative probability (integrated histogram) of the spectral shift $\Delta\lambda_{res}$ (1) Au with $610nm$ long pass filter, (2) Ag with $610nm$ long pass filter, (3) Au without long pass filter, (4) Ag without long pass filter. The spectral stability of gold is better (smaller average shift) than of silver. I assume that some activation energy related photochemical process is inducing an irreversible reshaping of the nanoparticle.

wavelength between initial and final resonance wavelength, a quantity I call the sensing cycle shift. For a reliable sensor, the mean sensing cycle shift should remain close to the experimental uncertainty ($\pm 0.5nm$) and I had disregarded all particles that did not show a full reversibility in the datasets for estimating particle sensitivity (within one standard deviation). Halide ions (Cl^- and especially Br^-) induce a reshaping of silver nanoparticles above a threshold concentration of $10 - 8M$ so I took care to avoid any use of those ions [Jiang & Yu, 2008, Cathcart et al., 2009]. Generally, I found that even without halide ions present, silver nanoparticles showed much worse reversibility performance than gold. I suspected a light induced process so I measured the reversibility with different filters in the light path. In the left plot of Figure 7.6 I show the sensing cycle shift of single nanorods plotted as a cumulative distribution probability (an integrated histogram that allows an easy visualization of the mean value) measured under different illumination conditions where each dot corresponds to the sensitivity cycle shift of a single particle. The sensing cycle shift is decreasing with increasing cut-off wavelength of the long pass filter. The mechanism of this light-induced irreversible shift remains unclear and is probably a combination of heating and photochemical processes. The shift has nothing to do with changing the environment as I checked in experiments that show a red shift of nanoparticles monitored continuously in water (right plot in Figure 7.6. Our experiments indicate that a sufficiently high cut-off filter allows the use of silver nanoparticles for sensing in environments without halide ions.

7.4 Summary

I have presented experimental results of silver nanorod sensitivity and compared them to results found for gold nanorods. Silver nanorods have up to two times higher sensitivity than gold nanorods in the spectral range of 600 to 700nm. Increasing nanorod width leads to higher sensitivity especially above 30nm, but the dominant factor that influences the sensitivity is the material of the nanorods. In the region of 700 to 900nm, the sensitivity is still about 10 to 20% higher. Calculations using MLWA (medium long wavelength approximation) and simulations with BEM (boundary element methods) confirm both material and size dependency. From simple theoretical arguments (Drude's model of optical properties of metals and the quasi-static-approximation), I developed an expression for the sensitivity, and I could identify the lower background (d-band electron) polarizability of silver compared to gold as the main reason for the higher sensitivity. The reversibility of silver nanorod based sensors is, generally, worse than gold nanorod based sensors, but adding a 610nm cut-off long-pass filter in the light path, resulted in a reasonably reversible sensor for both cases.

Chapter 8

Gold - Semiconductor - Nanohybrids

8.1 Introduction

In the past few years, numerous examples of binary hybrid nanocrystals have been reported with novel properties arising from their controlled topologies and geometries, for example, core-shell semiconductor quantum dots [Peng et al., 1997, ?], linear and branched sections of two semiconductors [Shieh et al., 2005], magnetic-noble metal nanocomposites [Pazos-Perez et al., 2007], metal-tipped semiconductor nanorods and tetrapods [Mokari et al., 2004, Carbone et al., 2006, Liu & Alivisatos, 2004, Khalavka & Sönnichsen, 2008], and magnetic-functionalized semiconductor nanorods [Buonsanti et al., 2006, Casavola et al., 2007]. Particularly, metal-semiconductor hybrid nanocrystals offer potential opportunities for solar energy conversion [?] and photocatalysis [Subramanian et al., 2004]. Their nanoscopic dimension alters the electronic and optical properties via the quantum confinement effect in the semiconducting part (leading to a size tunable band gap [Alivisatos, 1996]) and via the electrodynamic confinement ("plasmon") in the metal part (leading to a very high polarizability at the plasmon frequency [Eustis & El-Sayed, 2006]). Potentially, the plasmonic "antenna-effect" could amplify the excitation or radiative decay of excitons in the semiconductor [Lin et al., 2006, Fedutik et al., 2007]. Charges generated by the excitation of the semiconducting part can be transferred to the metal part shifting the plasmon frequency [Mulvaney, 1996, Hirakawa & Kamat, 2004, Wood et al., 2001] and/or promoting redox reactions [Subramanian et al., 2004, Costi et al., 2008, Elmalem et al., 2008]. Complex semiconductor and plasmonic material systems have been reported mainly focussing on switching the plasmon spectral wavelength or the intensity

8.2 Growth of large Gold Domains on CdSe/CdS Nanorods

In recent years, great advances have been made toward designing the controlled growth of small Au crystals selectively on the tips of CdSe and CdS rod-shaped nanocrystals, where the metal is in direct crystalline contact with the semiconductor part [Mokari et al., 2004, Saunders et al., 2006]. These structures underwent a change from two-sided (dumbbells) to one-sided (matchstick) growth attributed to intraparticle electrochemical Ostwald-Ripening where the smaller metal domains are dissolved in favor of the larger tip [Mokari et al., 2005, Mokari et al., 2006]. The gold tips on the semiconductor rods can both serve as anchoring points for self-assembly [Mokari et al., 2004, Figuerola et al., 2009, Salant et al., 2006] and accumulate electrons photogenerated in the semiconductor to drive redox reactions [Wood et al., 2001, Costi et al., 2008, Cozzoli et al., 2005].

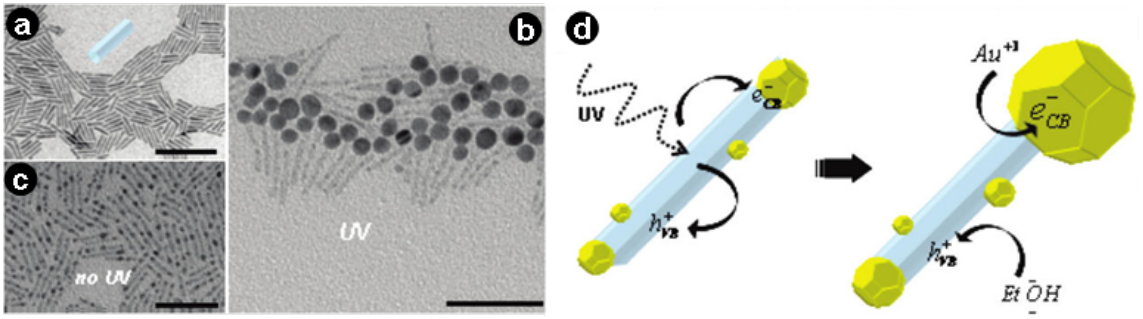

Figure 8.1: (a) TEM image of the CdS nanorods used as starting material. (b) Au-CdS hybrid nanorods formed after UV irradiation. (c) Control experiment without UV light (all scale bars 50 nm). (d) Sketch of the mechanism for photoinduced growth of large gold domains (yellow) on semiconductor CdS nanorods (light blue). (Image taken from [Carbone et al., 2009].)

Until now, it has not been possible to control the metal size in those systems. The gold domains were typically in the order of 2.0 nm in diameter when reacting with CdS nanorods in anaerobic condition and eventually just overcame 10 nm when ripened for 3 days in the presence of oxygen for nanorods longer than 50 nm [Saunders et al., 2006]. Since plasmons in gold nanoparticles are strongly damped for particle diameters below 10-20 nm by surface scattering [Hu et al., 2008, Pinchuk et al., 2004] and the size dependent d-band-Fermi-level offset [Phala & van Steen, 2007], the poorly understood interaction between plasmons and excitons could not be studied in detail in such hybrid particles. Here, we provide a strategy for creating large gold domains of controlled size (up to 15 nm) on CdS or CdSe/CdS quantum rods [Carbone et al., 2007] through the photoreduction of gold ions. The metal deposition is promoted and controlled by UV light irradiation under anaerobic conditions. The large gold domain supports efficient plasmon oscillations with a light scattering cross section large enough to visualize single hybrid particles in a dark-field microscope during the particle growth in real time.

8.2.1 Synthesis of CdSe/CdS Nanorods with Large Gold Tips

First, CdS and CdSe(core)/CdS(shell) nanorods were prepared using the seeded growth method [Carbone et al., 2007] (Figure 8.1a). This method produces rods with narrow size distribution. In addition, gold tipped CdSe/CdS dumbbells were grown [Mokari et al., 2004, Saunders et al., 2006] using the beforehand synthesized CdSe(core) / CdS(shell) nanorods as starting material. After purification, every nanorod sample was suspended in a mixture of $CHCl_3$/EtOH (90:10 v/v) and while stirring, a chloroformic solution of $HAuCl_4$, (di-n-dodecyl)dimethylammonium bromide (DDABr), and dodecylamine (DDA) was drop-wise injected (within 3 min). Afterward, every semiconductor solution was irradiated using an ordinary UV lamp (wavelength 366 nm, 2-3 mW/cm^2) for up to 120 min withdrawing the aliquots at scheduled intervals for further characterization. The growth was interrupted by removing the irradiation source, percipitating the particles with acetone, drying, and resuspending the precipitate in chloroform: depending on the dilution volume, the final sample appeared dark or pale violet. Large gold domains form selectively on one side of each semiconductor rod exclusively under UV irradiation (Figure 8.1b). There is only one large gold domain per semiconductor rod regardless whether a CdSe seed is present in the CdS rods or whether there are preformed gold domains on both tips. Control experiments without UV light (Figure 8.1c), without EtOH, without semiconductor rods, or with UV irradiation before Au injection showed no large gold domain formation confirming the importance of each component

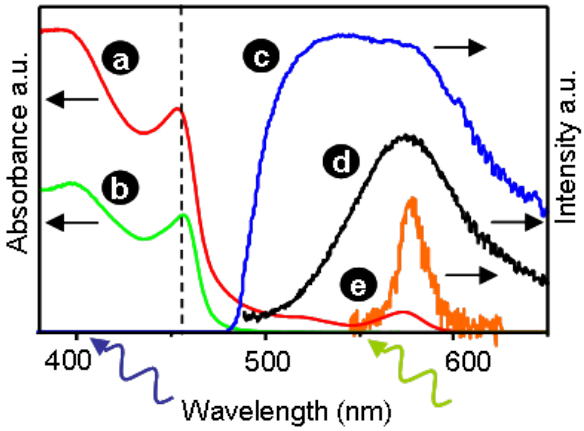

Figure 8.2: Absorbance of CdSe/CdS (a) and of CdS (b) semiconductor nanorods. (c) Spectrum of the white light illumination with 495 nm long-pass filter. (d) Typical single particle scattering spectrum of the gold domain grown on CdSe/CdS semiconductor nanorod. The peak is red shifted compared to bare gold sphere plasmon peaks (540 nm), probably due to the high index of refraction of CdS (ca. 2.5) and also due to less perfect spherical shape. (e) Fluorescence spectrum of a single CdSe/CdS nanorod (max. @ 580 nm). *The curved arrows at the x-axis* indicate the excitation wavelengths: 405 nm and 562 nm. The *dashed line* indicates the absorption band edge of the semiconductor nanorods. All curves have been rescaled for better visibility.

and reaction step.

8.2.2 Growth Model of the large Gold Tip

We propose a model based on the mechanism shown in Figure 8.1d to explain the observed gold domain formation. After a few drops of Au^{3+} ions are injected, small gold domains form instantly on the sides and at the tips of the semiconductor rods without need of UV light excitation [Mokari et al., 2006]. Since the photocatalysed one-sided growth also occurs on preformed dumbbells, they are likely an intermediate structure at this point. Upon UV stimulation, the electron (e-) created in the semiconductor migrates preferentially to one metal tip reducing further Au^{3+} ions [Costi et al., 2008], whereas the correlated hole (h^+) is reduced by the solvent. The efficiency of carrier separation is further improved by organic electron donors present in the reaction mixture like EtOH, $CHCl_3$ and even Br^- that can (in deaerated systems) scavenge the valence band holes [Cozzoli et al., 2004, Choi & Hoffmann, 1997, Calza et al., 1997]. Supporting the proposed mechanism, we find no large gold domain growth when exciting pure CdS rods with an energy (2.21 eV or 562 nm) smaller than the band gap of CdS. Interestingly, we observe also no gold domain formation when CdSe/CdS nanorods are excited at 562 nm, which is enough to excite the CdSe core (see greenish curved arrow in Figure 8.2), indicating that the electrons created within the CdSe core remain confined and are not able to transfer to the gold domain. The model above explains the photoinduced gold-domain formation but not why only one out of several initially formed small gold domains growths larger. An earlier explanation for one-sided Au growth (observed in experiments without light excitation over long time periods) proposed an electrochemical ripening process. A gold atom returns to the solution as a positive ion and the remaining electron transfers via the semiconductor rod to another gold domain where it is able to reduce a gold ion [Saunders et al., 2006]. The electron transfer along the particle greatly enhances the ripening speed.

The switch from two-sided to one-sided gold domains is much faster in our case than the previously observed ripening process that took place over the course of days. There is also no evidence for the dissolution of small gold domains. We believe a different mechanism is in place in our case: one of the initially formed gold domains, usually at the tip, attracts the vast majority of the photoelectrons reducing gold ions from solution. Since the selective drift of electrons to one domain does not involve any oxidation of gold atoms, our mechanism is not a ripening process. The question is, how does one gold domain attract all the electrons or majority of gold reduction?

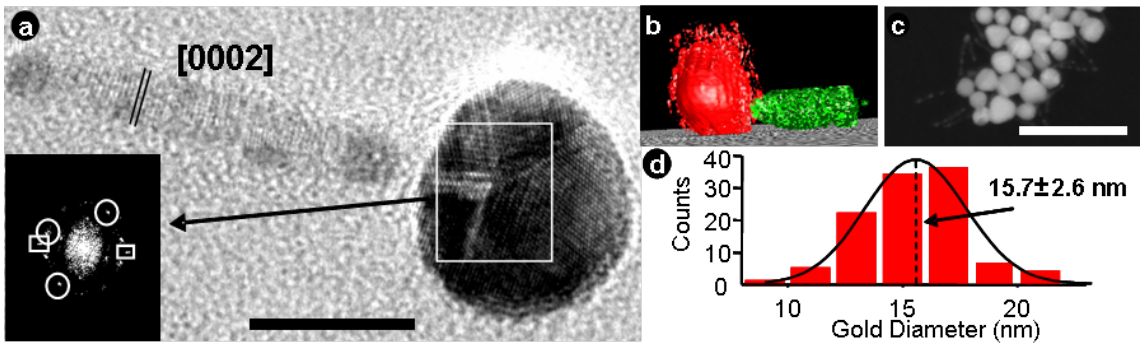

Figure 8.3: (a) Representative HR-TEM image of the Au-CdS hybrid particle displaying a 5-fold symmetry of the gold domain nucleated on one nanorod tip. The inset shows a FFT-pattern of the gold domain region indicated by the white box. Circles and squares mark the 111 and 220 reflections, respectively. Visible on the lateral nanorods facets and on the opposite tip are small gold islands (scale bar 10 nm). (b) Projection of the 3D particle model reconstructed from a tilt series (tomography) showing a noncentrosymmetric gold domain attachment. (c) High-resolution SEM image (scale bar 50 nm). (d) Gold domain size distribution of more than 100 particles for a generic sample irradiated for 120 min. (Image taken from [Carbone et al., 2009].)

It could be due to a lower barrier to the semiconductor (less passivated interface), a lower surface tension, a higher electrical capacity, or a combination of these factors. Another force driving electrons mainly in one direction might be the influence of the intrinsic electrical dipole moment of the binary II-VI nanocrystals or a preferential crystal matching between gold and certain CdS facets. In our opinion it is favorable for the electrons to end up in the largest gold domain due to its higher electrical capacity but this point should be subject to more investigation.

8.2.3 TEM-Characterization of the Au-CdSe/CdS nanohybrids

Electron microscopy gives us further details of the growth process. High resolution TEM images show the crystalline nature of the entire hybrid particle (Figure 8.3a). The CdS wurtzite lattice is preserved and the large gold domain typically shows pentagonal twinning. There are very small gold domains at irregular intervals and at the second tip (Figure 8.3a), which form at rod surface defects [Saunders et al., 2006] or defects in the surfactant layer [Menagen et al., 2009]. We also observe a nonsymmetric attachment of the gold domains to the CdS rod on TEM tomographic reconstructions from low-resolution TEM images (Figure 8.3b). The particles do not actually resemble “nanomatchsticks” but rather “nanosized smoking pipes”. The asymmetry could result from a preferential crystallographic interface between the (111) facets of the pentatwinned gold crystal and the (101) facet of the CdS rod [O’Sullivan et al., 2008]. The asymmetric attachment of the gold domain slightly shortens the apparent semiconductor rod length under some viewing angles, which may be wrongly ascribed to a rod etching. In this context, UV-induced growth experiments carried out on very short nanorods showed no significant etching of the semiconductor. As an example, a statistical analysis of the gold domain diameters deduced from TEM images shows a mean diameter of 15.7 nm with a polydispersity of 30% after 120 min of growth (Figure 8.3d). The domains are therefore large enough to support a strong plasmon oscillation where the bulk dielectric function of gold describes the optical properties well [?].

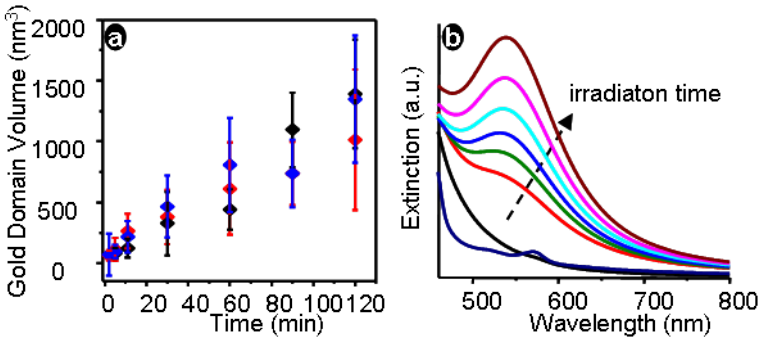

Figure 8.4: (a) Gold domain volume extracted from TEM images (100 nanoparticles per data point). Red, CdSe/CdS nanorods; blue, CdS nanorods; black, nanodumbbells. (b) Optical extinction with increasing UV irradiation time. The plasmon peak at 536 nm grows over time. (Image taken from [Carbone et al., 2009].)

8.2.4 Optical Extinction of the Au-CdSe/CdS nanohybrid-Ensemble at different stages of growth

In order to learn more about the growth kinetics, we carefully analyzed the evolution of particle size over time using the following three methods: TEM analysis of aliquots taken at regular time intervals, real-time optical extinction monitoring during growth, and single particle spectroscopy of individual particles in a flow cell (these last two topics will be discussed in subsequent chapters). The results of the TEM analysis are shown in Figure 8.4a. We measured the diameter of the gold domains of approximately 100 particles per sample on low-resolution TEM images after reaction times of 2, 5, 11, 30, 60, 90, and 120 min. Independent of the employed starting material (CdS, CdSe/CdS, dumbbells), the volume of the gold domain shows a linear increase over time at a rate of about 0.24 nm^3/s (14 atoms/s) as expected from a constant rate of electron generation in the semiconductor particle. Since the plasmon excitation (530 nm) does not overlap with the semiconductor rod absorption, simultaneous optical extinction measurements during the growth show a corresponding increase in the optical density around the plasmon resonance (Figure 8.4b). For irradiation times longer than 120 min, the particles start to aggregate and the gold domains fuse together. From the measured absorbance and the particle concentration, we estimate an absorption cross section of our CdS rods of 4.46 × 10-14 cm^2 at 366 nm, which means the generation of 166 photoelectrons/s per particle at our irradiation intensity (2 mW/cm^2). From this, we estimate that after 120 min, circa 50% of the injected gold ions have been reduced. Assuming all gold ions in the +3 oxidation state, we calculate an efficiency of approximately 25% for the photoreduction process. The charge separation process in our metal-semiconductor hybrid particles is therefore very efficient and promising for light harvesting purposes.

8.2.5 Observation of Charging induced Plasmon Shift in Au-CdSe/CdS nanohybrid-Ensemble

Further insight confirming the light driven gold domain formation process shown in Figure 8.1d comes from a careful analysis of optical extinction measurements during particle growth. From spectra acquired every 150 s, we extracted the spectral position of the plasmon extinction maximum λ_p (Figure 8.5 left, black plot, left axis) and the corresponding "intensity", I_p, the extinction value at the maximum (Figure 8.5 left, blue plot, right axis). I_p allows monitoring of the growth of the gold domain and plasmon resonance λ_p indicates the accumulated charge [Hirakawa & Kamat, 2004]. At time zero we added an amount of gold ions that is insufficient to form the large gold domains. Under UV irradiation, the plasmon peak intensity I_p started to increase indicating Au-Tip growth. After about 30 min of UV irradiation, the plasmon intensity increase leveled off indicating the depletion of gold ions and the halt of growth. However, the plasmon peak position

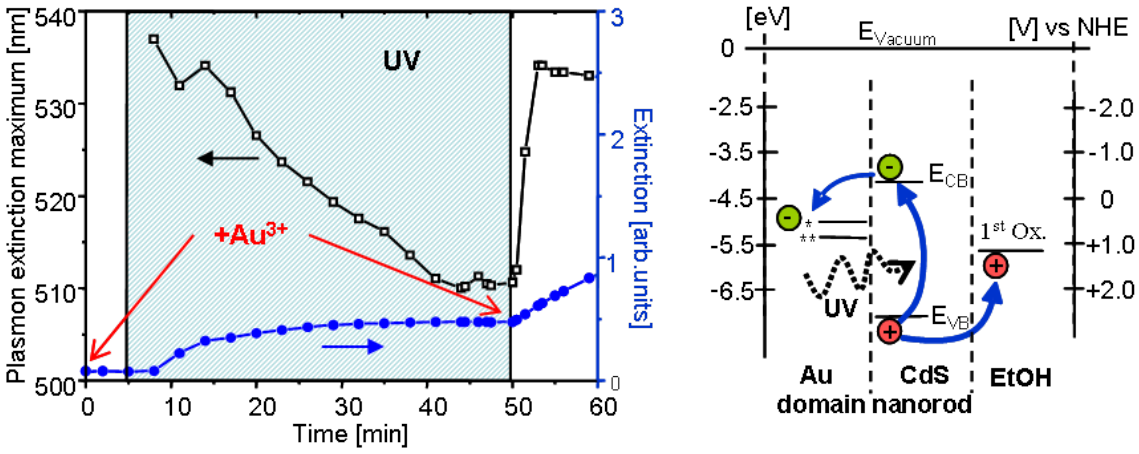

Figure 8.5: *Left:* Spectral position of the plasmon extinction maximum λ_p and its absolute extinction value I_p over time. At time t = 0, a small amount of gold ions (ca. 6000 Au atoms per rod) were added to CdSe/CdS nanorods in a mixture of ethanol and chloroform. *Right:* Diagram of the Fermi level of the gold domain , the conduction and valence band edges of CdS nanorods (E_{CB}, E_{VB}, respectively) and the first oxidation level of ethanol before irradiation [Cozzoli et al., 2004, Yang, 2006]. The bulk Fermi-level of small gold domains (*) is slightly lower than in larger gold domains (**) [Phala & van Steen, 2007]. (Image taken from [Carbone et al., 2009].)

λ_p shifted to the blue with a constant rate from its initial position at about λ_p= 535 nm. Only after 40 min, we observed a sudden stop at 510 nm (25 nm blue shift). The blue-shift is due to an accumulation of negative charges in the gold domain, increasing its electron density and plasmon frequency [Wood et al., 2001]. The saturation indicates an equilibrium of the metal's Fermi level and the semiconductor conduction band edge where the Fermi level of the gold domain increases from -5.1 eV to -4.1 eV during charging (Figure 8.5 right). The magnitude of the observed plasmon resonance shift corresponds to a potential difference of 1V for a approximately 3 nm diameter sphere. Since we only added such an amount of gold ions that is insufficient to form the large gold domains, we have a good agreement between our experimental findings and model. A previously measured plasmon shift of 29 nm per 1 V in 2 nm gold spheres has been reported by other groups [Mulvaney et al., 2006]. After 50 min, we stopped the UV irradiation and added more gold ions discharging the gold domains, thus rapidly shifting back the plasmon resonance, and increasing again the plasmon intensity I_p.

8.2.6 Observation of Single Particle Growth with Dark-Field Microscopy

With the aim to avoid particle aggregation and to monitor the metal growth in real time, we performed single particle measurements of nanorods immobilized in a glass flow cell. Details of the dark-field microscope setup and the flow cell are sketched in Figure 8.6a, and A.1 in Appendix, respectively. At first, CdSe/CdS nanorods are fixed in the flow cell using following immobilization protocol:

1. The cell is washed with 60mL of Hellmanex (Hellma)/Millipore H_2O solution 4% v/v
2. washing with 60 mL of Millipore H_2O
3. washing with 60 mL of pure EtOH The flow cell is transferred into the glovebox for the following steps and anhydrous solvents are used hereafter
4. washing with 6 mL of pure $CHCl_3$

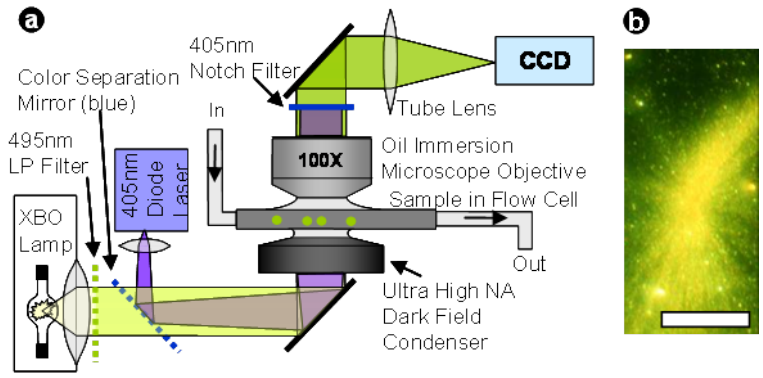

Figure 8.6: (a) Microscope setup with a 405 nm laser diode for photoexcitation of the semiconductor nanorods and white light dark-field contrast for the observation of gold domains. (b) A dark-field light scattering image of the particles (greenish dots) after large gold domains formed following the laser intensity distribution (scale bar is 50 µm). (Image taken from [Carbone et al., 2009].)

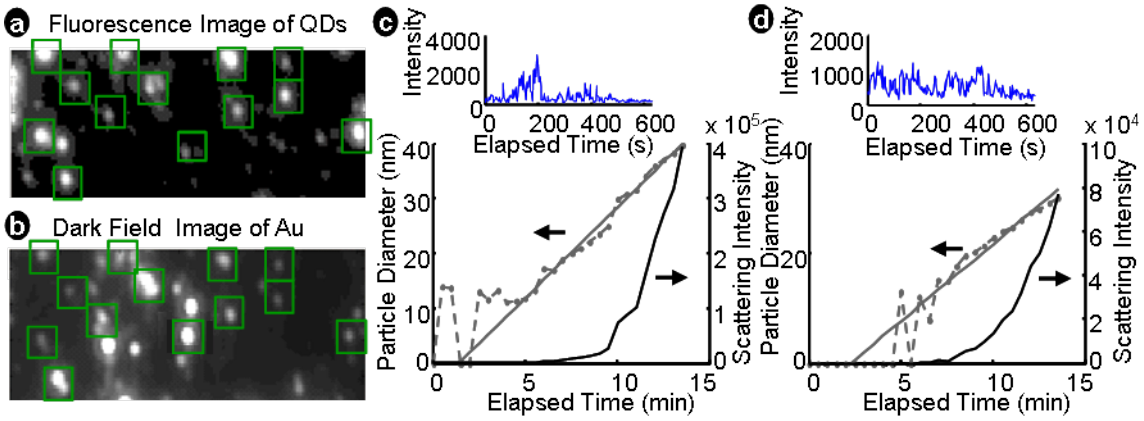

Figure 8.7: (a,b) Time trace of representative cases of the gold domain growth (main graphs) observed on single particles which were identified by the blinking behavior of the semiconductor quantum dot at the same position (insets). (c) Snapshot of the blinking semiconductor quantum dot fluorescence intensity signal recorded with the Plasmoscope CCD Camera (d) Snapshot of the plasmon scattering signal of the gold domains in the area of (c). (Image taken from [Carbone et al., 2009].)

5. functionalizing with 12 mL of mercapto-silane in $CHCl_3$ (5% v/v)
6. washing with 6 mL of pure $CHCl_3$
7. 4 mL of chloroformic solution 1.4 10-10M
8. washing with 2 mL of pure $CHCl_3$;
9. washing with 4 mL of EtOH in $CHCl_3$ (30% v/v)
10. The glass capillary is filled again with a solution 30% (v/v) of EtOH in $CHCl_3$ and sealed tightly with two syringes at both ends of the flow cell

The location of the CdSe/CdS semiconductor nanorods before the addition of gold is determined by looking at their fluorescent signal (blinking) on excitation at 405 nm (3.06 eV). The flurescence spectrum of single semiconductor nano rods are centered around 582 nm () and . (Figure 8.7a). Then we change the medium to the gold growth solution (everything under anaerobic conditions) and keep a constant flow to avoid depletion of gold ions. A simultaneous broad-band illumination of 490 nm to 700 nm (1.77 eV to 2.53 eV) through an ultrahigh numerical aperture dark-field condenser allows the observation of light scattered by the growing gold domains at the locations where previously fluorescence signal of immobilized CdSe/CdS nanorods was observed (Figure

8.7b). The white light and the violet laser are combined with a 45° degree blue dichroic color separation filter as indicated in Figure 8.6a. The laser light is then blocked out after the objective by a 405 nm notch filter to reduce the background. The broad-band illumination is created by filtering the white light of an XBO lamp with a 495 nm (2.5 eV) long pass (LP) filter (see Figure 8.2c) to suppress excitation of the semiconductor nanorod by the white light. Although as shown in Figure 8.2a and b, the experimentally measured absorption band edge of our CdSe/CdS nanorods is at 460 nm (2.7 eV) there is a residual small absorption as far as 590 nm (2.1 eV) due to the smaller band-gap of the CdSe core. Due to this residual absorption it would make sense to use a long pass filter with a more red-shifted cut-off wavelength that would completely prevent the excitation of the semiconductor nanorods by white light. But as mentioned in 8.2.2 we detect no significant gold domain growth in ensemble if the semiconductor nanorods are illuminated with energies below the absorption band edge of CdS. Also we have to consider that the plasmon peak maximum of the growing gold domains are in the range of 540 nm and above (see Figure 8.2d), therefore we need to leave this spectral window open if using broad band illumination to excite the plasmonic gold domains.

The fluorescent signal is completely quenched as soon as the gold ions are added but a growing light scattering signal I_{sca} of gold domains develops. After about 1 min of growth, the signal is clearly above noise level and gradually increases with time (Figure 8.6b). The intensity I_{sca} is converted to particle volume V by comparing with the intensity of 40 nm Au spherical particles and using the relation $I_{sca} \propto V^2$. We observe a linear increase of the gold domain diameter over time with 1.4 to 2.6 nm/min and no sign of saturation (Figure 8.7 c and d). The linear increase in diameter (not volume) with time indicates a diffusion controlled step as a limiting factor in the reaction not the amount of photoelectrons generated in the particle. A dark-field light scattering image taken at the end of the experiment clearly shows that the size of the gold domain formation follows the intensity distribution of the illumination by the blue laser (Figure 8.6b); the laser light was distributed in the sample plane in a "star-like" pattern and the gold particle distribution follows this pattern nicely. Control experiments without semiconductor rods show no significant gold particle formation under laser irradiation.

8.3 Switchable Plasmon Resonance in Gold-Semiconductor-Nanohybrids

The increased demand of processing power asks for solutions that can increase the speed of integrated circuits. Plasmonic devices, a relatively new device technology, are promising candidates for future integrated circuit elements. That is because plasmonics resolves a basic mismatch between wavelength-scale optical devices and the much smaller components of integrated electronic circuits. Although a number of techniques for controlling the propagation of guided surface plasmon polariton signals have been demonstrated [Nikolajsen et al., 2004, Pala et al., 2008] some of them even utilizing semiconductor quantum dots [Pacifici et al., 2007, Gomez et al., 2010]. Also switchable single particle plasmonic systems utilizing liquid crystals [Muller et al., 2002] were studied, but up to now no report has surfaced about localized SPP switching using noble metal and semiconductor nanoparticle combinations. We presented in Chapter 8.2.5 the experimental observation of shiftig the plasmon resonance by charging the gold domain with the assistance of the semiconductor nanorod and EtOH as surrounding medium. In this chapter we want to examine the possibilities of using a single Au-CdSe/CdS nanohybrid as a nanosized plasmonic switch.

As experimentally demonstrated by Mulvaney [Mulvaney et al., 2006] the the plasmon wavelength can be blue shifted if the plasmonic particle is charged up, since the LSPP (localized surface plasmon polariton) frequency depends on the conduction electron density (see Chapter 2.2.2). The

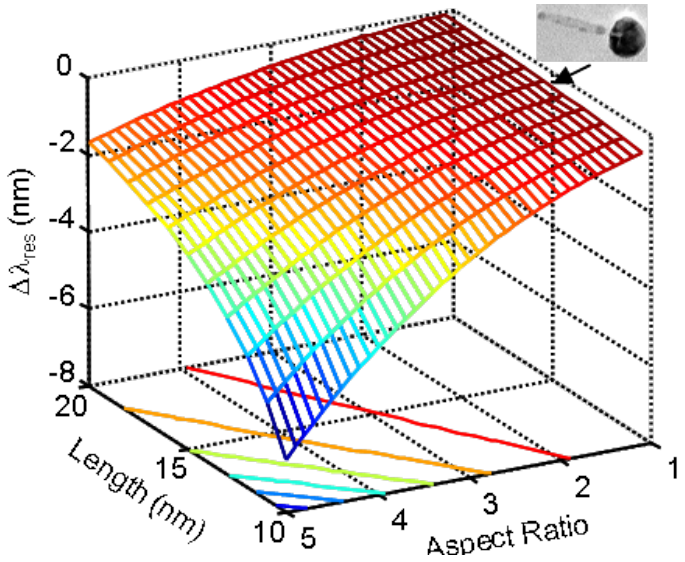

Figure 8.8: Surface plot of the resonance wavelength shift $\Delta\lambda_{res}$ vs. aspect-ratio (AR) and long axis of the gold domain for 1 eV difference between the Fermi-energy of the uncharged gold domain and the conduction band edge of the semiconductor nanorod. The black arrow indicates the location of our nanohybrids with nearly spherical shape (AR = 1, length = 15 nm).

shift of the plasmon resonance wavelength, $\Delta\lambda$ upon changing the electron density by Δn obeys a very simple relationship [Mulvaney et al., 2006]:

$$\Delta\lambda = -\lambda_0 \frac{\Delta\rho}{2\rho} \tag{8.1}$$

where λ_0 is the resonance wavelength, and ρ is the conduction electron density of the uncharged nanoparticle. Interestingly, this relation holds for nanoparticles of any shape if the particle size is so small that its optical response can be treated within the dipole (quasi static) approximation. Equation 8.1 predicts thus a blue shift of the resonance wavelegth (to shorter wavelengths) if the electron density increases. To obtain a large shift we only have to find a way to increase the electron density in the gold domain. Of course the number of electrons that can be transferred onto the gold domain has an upper limit. Each additional electron increases the Fermi-energy of gold, E_F^{Au}, and as soon the Fermi-energy reaches the semiconductor nanorod conduction band edge energy, E_{CB}^{SC} the charging stops. For a given potential difference $\Delta\phi = (E_{CB}^{SC} - E_F^{Au})/e$ the magnitude of Fermi-energy increase ΔE that an individual electron can cause depends on the static electric self-capacitance C of the gold domain through the relation:

$$\Delta E = \Delta\phi e = \Delta N e^2 / C \tag{8.2}$$

with e the charge of an electron and $\Delta N = \rho \cdot V$ the number of added electrons, V is the volume of the gold domain. This indicates that a larger static electric capacity results in a smaller increase of the Fermi-energy per added electron, thus allowing the addition of more electrons for a given potential difference. Since the selfcapacitance grows with increased elongation of the particle, there is a strong shape-dependency of the charging capacity of the gold domains in our nanohybrids. To estimate the magnitude of the resonance wavelength shift as function of the physical dimensions for a potential difference $\Delta\phi$, we need to rearrange 8.2 to express $\Delta\lambda$:

$$\Delta\lambda = -\lambda_0 \Delta\phi \frac{C}{2Ne} = -\lambda_0 \Delta\phi \frac{C}{2V\rho e} \tag{8.3}$$

If we restirct ourselves to calculate the plasmon resonance wavelength shift for only rod-like objects

we have to use the expression for the selfcapacitance of a prolate shaped particle where the length l is larger than the width w is given by:

$$C = \frac{4\pi\epsilon_0\epsilon_{dc}\beta}{\ln\left[(\frac{l}{2}+\beta)/(\frac{l}{2}-\beta)\right]} \tag{8.4}$$

with ϵ_{dc} as the static dielectric constant of the surrounding medium and with $\beta = \sqrt{(l/2)^2 - (w/2)^2}$. Inserting the expression for volume of a prolate: $V = \frac{1}{6}\pi l w^2$ we finally obtain the relation for the resonance wavelength shift:

$$\Delta\lambda = -\lambda_0\Delta\phi\frac{\epsilon_0\epsilon_{dc}}{3\rho e}\cdot\frac{\beta}{lw^2\ln\left[(\frac{l}{2}+\beta)/(\frac{l}{2}-\beta)\right]} \tag{8.5}$$

In the special case of spherical gold domains where $l = w$ the expression above reduces in limes to:

$$\Delta\lambda = -\lambda_0\Delta\phi\frac{3\epsilon_0\epsilon_{dc}}{2l^2\rho e}. \tag{8.6}$$

This expression clearly indicates that with increasing diameter l the spectral shift decreases drastically. Now to estimate the obtainable plasmon resonance wavelength shift in our nanoparticle hybrid system, let's enter following physical parameters into 8.5:

1. ethanol as surrounding medium with $\epsilon_{dc} = 24.3$ and refractive index: $n = 1.36$ [Lide, 1993].
2. plasmon resonance wavelegth of prolate nanorods as function of length and width: $\lambda_0 = 495.14 + (l/w \cdot 53.71 - 42.29)\, n^2$ [Link et al., 2005].
3. gold with conduction electron density of $\rho = 59nm^{-3}$ [Kopitzki, 1993], with diameter (length) of 15 nm and $E_F^{Au} = -5.1eV$.
4. CdSe/CdS semiconductor nanorod with $E_{CB}^{SC} = -4.1eV$ (see energy diagram in Figure 8.5 right).

With the resulting potential drop of $1V$ between gold Fermi-level and CdS conduction band we receive a resonance wavelength shift of $-0.15nm$, which is too small for us to be able to experimentally measure, since the spectral resolution of the setup described in Chapter 3 is only a little less than $0.5nm$. Figure 8.8 displays the resonance wavelength shift calculated for our nanohybrid system, where the length of the gold domain is varied between 10 and $20nm$ and the aspect ratio is varied from 1 to 5. We see that with increased prolongation of the particle the resonance wavelength shift increases, due to the increasing self-capacitance. We also see that to get a large plasmon resonance wavelength shift, it is advantagous to have rather small particles, because - as Equation 8.6 indicates - the linear growth of capacity with length is drastically counteracted with the power of 3 increase of the number of the required electrons with length. The consequence of the results in Figure 8.8 is that we have - from the perspective of plasmon switching purposes - two unfortunately competing trends. Increasing the gold domain size leads to a much stronger scattering plasmon resonance but this increase causes also a reduction of the achievable spectral shift. I see several ways to overcome this obstacle:

1. Increasinig the aspect ratio of the gold domain.
2. Increasing the spectral resolution by using more sensitive (lock-in type) measurement methods that are currently under development in our group.
3. Using different semiconductor nanoparticle materials with larger bandgap and lower electron affinity (= energy of the bottom of the conduction band compared to vacuum), like ZnSe ($E_g = 2.71eV$, $\chi = 4.09eV$) [Kasap & Capper, 2006] could increase the potential difference between gold Fermi-level and semiconductor conduction band edge.

8.4 Summary

TEM data, optical extinction measurements, and the single particle growth data support the model of photoinduced one-sided gold domain formation on semiconductor rods shown in Figure 8.1d. This model involves no ripening but rather a directed photoelectron drift toward the largest gold domain. The UV excitation leads to a growth of only one domain per semiconductor rod resulting in an anisotropic smoking-pipe structure. Because of the large metal part, we created a route for an easy transfer of the hybrid particles to polar solvents after a proper functionalization. The conversion of photogenerated electrons to reduced gold atoms is very efficient at early times. The single particle measurements demonstrate that gold domains can be arbitrarily large (above 40 nm in diameter) on supported particles in a flow cell. A careful analysis of the plasmon peak position during growth shows the buildup of electrons in the gold domain. In contrast to other systems where photodeposition of metals on semiconductors was observed (e.g., Ag, Au, Cu, Pt, on ZnO) [Wood et al., 2001], we create large gold domains with only one domain per rod. The light driven large gold domain formation on semiconductor nanorods allows for the controlled synthesis of nanocrystals supporting both plasmons and excitons with a light scattering cross section large enough to visualize single hybrid particles in a dark-field microscope. The combination of semiconductor and plasmonic materials gives ways to possible routes of switchable plasmons, that could be employed as fast switching plasmonic transistors in future's integrated circuits.

Chapter 9

Summary

In this thesis I discussed following topics: a comprehensive summary of optics of conductive materials with focus on plasmonic nanoparticles and semiconductor quantum emitters, a concept of a newly developed single particle spectroscopic setup, and experimental results achieved with this setup. The novelty of the setup comprises: (1) increased sensitivity, (2) extended spectral range, (3) intelligent data analysis, and (4) improved modularity. Earlier automatized single particle spectroscopic setups suffered from sensitivity and spectral limitations. The new setup that I termed *Plasmoscope* helps to surpass the sensitivity and spectral limitations of earlier automatized single particle spectroscopic setups. Some highlights of my achievements with the *Plasmoscope* are the first time observation of optical scatterings of a large number of nanoparticles down to $15nm$ in diameter, and the first measurements of near infra-red single nanoparticle spectra in high quantities. This last achievement is quite significant because potential medical applications of plasmonic nanoparticles require a spectral response in the therapeutic window (a.k.a. "optical window") that extends from $650nm$ to $900nm$.

To overcome the spectral limitations of earlier spectroscopy setups I desinged an automatized spectroscopy setup that avoids using optical elements that significantly absorb in the visible and the near infra red. The backbone of the design is an adjustable vertical slit placed into the entrance plane of the spectrometer where the magnified image of the sample is projected by the microscope and a precision positioning stage to scan the sample through this narrow window. Accompanying the hardware design and realization, I developed a software package that controls the hardware and performs data extraction and extensive analysis.

The first application of the *Plasmoscope* was the spectral measurement of a large number of single silver coated gold nanorods. My colleagues, Jan Becker and Inga Zins produced with careful analysis of the plasmon linewidth of silver-coated and uncoated gold nanorods two surprising and important results (presented in Chapter 4): ensemble linewidth narrowing despite the blue shift of the peak maximum and single particle linewidth narrowing. My *Plasmoscope* setup allowed the investigation of several hundred single particles and the collection of enough statistics to compare particles at the same resonance wavelength across a wide range of the optical spectrum. Since the damping (and thus the single particle line-width) decreases with the resonance wavelength only this direct comparison at the same wavelength makes sense. I could experimentally show that at a given resonance wavelength the plasmon life-time of silver coated gold is longer than that of bare gold.

As mentioned, one of the most promising projected application of plasmonic nanoparticles is to use them as biological markers or sensors. Since organic tissue becomes relatively transparent in the range between 650 and $900nm$ there has been keen interest to tune nanoparticle resonances

into this spectral range. Motivated by the limitations of the wet synthesis of gold nanoparticles, my colleague Andreas Henkel found a way to tune the resonance into the far red region by alloying copper and gold. Although it is very little known about the electron structure of alloys, we expected that the lower bulk plasmon frequency and the stronger damping of copper would red-shift the plasmon resonance. I discuss in Chapter 5 how the flatter slope of the dielectric function of disordered copper-gold alloy can cause a red-shift of the resonance with increasing copper content up to $Ag : Cu = 1 : 1$ and how specific copper contents lead to reduced intraband damping. Surprisingly, although the synthesized nanoparticles are thought to be disordered I found reduced intraband damping at specific copper contents in analogy to DC conductivity minimas for ordered bulk copper-gold alloys.

In order to increase the plasmonic sensing capabilities of nanoparticles Jan Becker and I performed a systematic analysis of parameters that influence the plasmonic sensitivity of gold nanorods. We report in Chapter 6 that for the sensitivity in energy units the optimal aspect ratio of gold nanorods lies between 3 and 4. Supported by my experiments, on the basis of Becker's theoretical investigations we could identify the range of optimal aspect ratios for various sensing schemes. As Becker pointed out, the quality factor of the resonance is the primary factor for the spectral position and magnitude of the maximum of the "figure-of-merit" sensing scheme.

Analyzing Becker's initial theroetical treatment of the sensitivity that is based on Drude's model of optical properties of metals and the quasi-static-approximation I identified two key material parameters that may influence the sensitivity: bulk plasmon wavelength and background polarizability. As presented in Chapter 7 by measuring a vast number of single nanoparticle sensitivities I succeeded to show experimentally for the first time that silver nanorod sensitivity exceeds gold nanorod sensitivity in the spectral range of 610 to $900nm$. I could show that the lower contribution of the bound electrons to the plasmon in silver (lower background polarizability) leads to a higher plasmonic sensitivity. Interestingly the sensitivity was found within this theory to be independent from shape and dimension for thin nanorods (widths of 10 to $30nm$), but not from the material. For such cases I developed an elegant expression that predicts the sensitivity as a function of resonance wavelength and the mentioned material parameters. On the other hand, I also found experimental evidence that the sensitivity of nanorods of the same material with widths above $30nm$ increases with the thickness. My theoretical treatment of the sensitivity based on Schatz and co-workers' [Kelly et al., 2003] Maxwell-Equation solution for nanorods up to the 3rd order to include size effects resulted in a successful prediction of size and material dependent plasmonic sensitivities. The reversibility of silver nanorod based sensors is, generally, worse than gold nanorod based sensors, but adding a $610nm$ cut-off long-pass filter in the light path I succeeded to suppress irreversibilities that resulted in a reasonably reversible sensor for silver and excellent reversible sensor for gold.

An effort in our group to use metal-semiconductor hybrid nanoparticles for energy conversion purposes led one of my coworkers (Luigi Carbone) to develop a way to grow gold domain on one end of a semiconductor nanorod. He successfully managed to synthesize metal-semiconductor hybrids with gold tips up to an average diameter of $16nm$. To understand this photo-activated growth better, I used my *Plasmoscope* to investigate this gold domain growth on a single particle level in real time. As presented in Chapter 8 these gold domains support efficient plasmon oscillations with a light scattering cross section large enough to visualize single hybrid particles. Being the first study of real time growth of single metal-semiconductor hybrids, we also mastered the difficulties accompanying with the observation of single particles in an anaerobic environment. My results confirmed our assumption that all semiconductor rods grow gold domains, and that light directly drives this process. Under UV illumination electrons accumulate on the gold domain that increases the electron density leading to a plasmon resonance blue shift that I hoped to be able to measure but eventually failed. As I point out in this work the amount of blue shift that is energetically possible

decreases with increasing volume therefore gold domains that are large enough to be observable exhibit only a small to negligible blue shift and vice versa. My suggestion to overcome this dilemma is increasing the aspect ratio of the gold domain that would allow a higher accumulation of electrons thanks to the increased capacity.

I hope that the presented scientific results in this work help to fine tune future plasmonic nanoparticles towards more efficient and robust structures that could be reliably employed in sensoric or energy conversion devices.

Chapter 10

Acknowledments

I would like to express my sincere thanks to people who directly or indirectly assisted me during my PhD studies.

I also want to thank to the company called Sigma-C that later became a part of the renowned TCAD company Synopsy. Through Sigma-C I discovered how much I like to work with nano-scaled optics and solid state physics.

Warmhearted acknowledges go to the creators of Lyx [The LyX Team, 2009], the document processor of this thesis.

This page is intentionally left empty.

Appendix A

Additional Figures

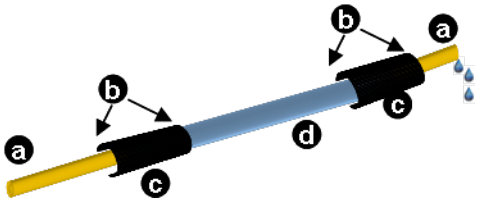

Figure A.1: The Flow-Cell. (a) Polyethylene Tubing (Intramedic Clay Adams brand, Becton Dickinson): inner diameter=0.28mm outer diameter= 0.61mm. (b) Epoxy Glue (5 min curing time). (c) Polyethylene Tubing (Intramedic Clay Adams brand, Becton Dickinson). inner diameter=1.67mm outer diameter= 2.42mm. (d) Borosilicate Glass Capillary W5010 (VitroCom Inc), inner dimensions: height: 0.1 mm, width: 2.0 mm, glass wall thickness: 0.1 mm.

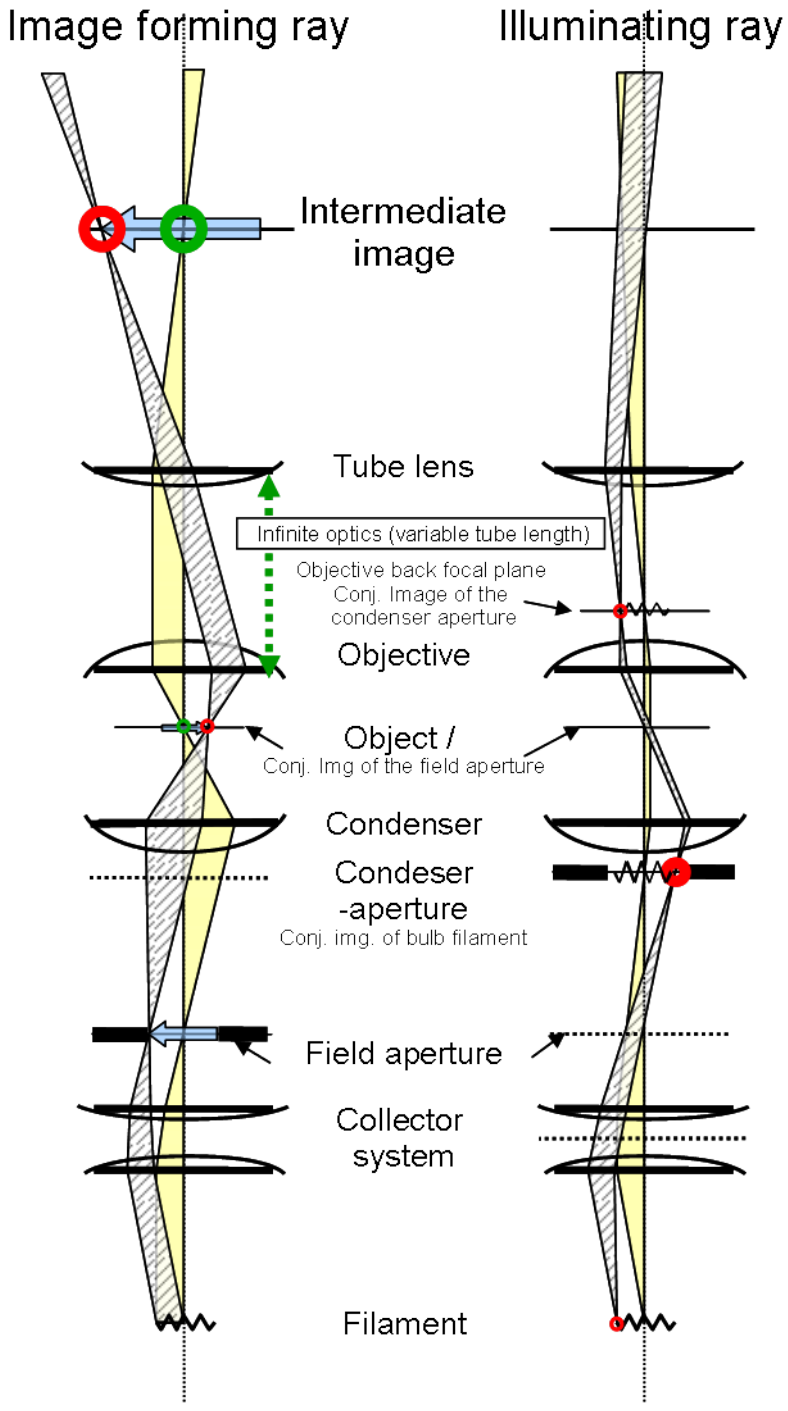

Figure A.2: Light path in a microscope with variable tube length utilizing Köhler's illumination concept. *Left*: the image forming rays create a magnified image in the image plane. But special care must be taken to keep the field aperture free of conatminations, because it is imaged onto the sample and therefore onto the image plane. *Right*: The advantage of Köhler's concept is that the illumination rays from each point of the light bulb filament is broadened and pass through the sample as a bunch of parallel rays. This provides a homogeneous illumination over a large area. Reducing the field aperture helps to improve contrast, and the condenser aperture adjusts the brightness.

This page is intentionally left empty.

This page is intentionally left empty.

This page is intentionally left empty.

Bibliography

[Alivisatos, 1996] Alivisatos, A. P. (1996). Perspectives on the physical chemistry of semiconductor nanocrystals. *Journal of Physical Chemistry*, 100(31), 13226–13239.

[Anker et al., 2008] Anker, J. N., Hall, W. P., Lyandres, O., Shah, N. C., Zhao, J., & Van Duyne, R. P. (2008). Biosensing with plasmonic nanosensors. *Nature Materials*, 7(6), 442–453.

[Arbouet et al., 2004] Arbouet, A., Christofilos, D., Del Fatti, N., Vallée, F., Huntzinger, J. R., Arnaud, L., Billaud, P., & Broyer, M. (2004). Direct measurement of the single-metal-cluster optical absorption. *Phys. Rev. Lett.*, 93(12), 127401.

[Ashcroft, 1976] Ashcroft, Neil W.; Mermin, N. D. (1976). *Solid State Physics*. Saunders College Publishing.

[Baciu et al., 2008] Baciu, C. L., Becker, J., Janshoff, A., & Sönnichsen, C. (2008). Protein-membrane interaction probed by single plasmonic nanoparticles. *Nano Letters*, 8(6), 1724–1728.

[Banhart & Czycholl, 2002] Banhart, J. & Czycholl, G. (2002). Electrical conductivity of long-range-ordered alloys. *Europhysics Letters*, 58(2), 264–270.

[Becker, 2010] Becker, J. (2010). *Plasmons as Sensors*. PhD thesis, Johannes-Gutenberg Universität in Mainz.

[Becker et al., 2007] Becker, J., Schubert, O., & Sonnichsen, C. (2007). Gold nanoparticle growth monitored in situ using a novel fast optical single-particle spectroscopy method. *Nano Letters*, 7(6), 1664–1669.

[Becker et al., 2010] Becker, J., Trugler, A., Jakab, A., Hohenester, U., & Sonnichsen, C. (2010). The optimal aspect ratio of gold nanorods for plasmonic bio-sensing. *Plasmonics*, 5(2), 161–167. Times Cited: 1 Cited Reference Count: 35 English Article PLASMONICS 597WQ.

[Becker et al., 2008] Becker, J., Zins, I., Jakab, A., Khalavka, Y., Schubert, O., & Sonnichsen, C. (2008). Plasmonic focusing reduces ensemble linewidth of silver-coated gold nanorods. *Nano Letters*, 8(6), 1719–1723.

[Bingham et al., 2009] Bingham, J. M., Willets, K. A., Shah, N. C., Andrews, D. Q., & Van Duyne, R. P. (2009). Localized surface plasmon resonance imaging: Simultaneous single nanoparticle spectroscopy and diffusional dynamics. *Journal of Physical Chemistry C*, 113(39), 16839–16842.

[Blaber et al., 2009] Blaber, M. G., Arnold, M. D., & Ford, M. J. (2009). Search for the ideal plasmonic nanoshell: The effects of surface scattering and alternatives to gold and silver. *JOURNAL OF PHYSICAL CHEMISTRY C*, 113(8), 3041–3045.

[Bohren & Huffman, 1983] Bohren, C. & Huffman, D. R. (1983). *Absorption and Scattering of Light by Small Particles*. New York: Wiley-Interscience.

[Boyer et al., 2002] Boyer, D., Tamarat, P., Maali, A., Lounis, B., & Orrit, M. (2002). Photothermal imaging of nanometer-sized metal particles among scatterers. *SCIENCE*, 297(5584), 1160–1163.

[Brigger et al., 2002] Brigger, I., Dubernet, C., & Couvreur, P. (2002). Nanoparticles in cancer therapy and diagnosis. *Advanced Drug Delivery Reviews*, 54(5), 631–651.

[Bruchez et al., 1998] Bruchez, M., Moronne, M., Gin, P., Weiss, S., & Alivisatos, A. (1998). Semiconductor nanocrystals as fluorescent biological labels. *SCIENCE*, 281(5385), 2013–2016.

[Bryant et al., 2008] Bryant, G. W., De Abajo, F. J. G., & Aizpurua, J. (2008). Mapping the plasmon resonances of metallic nanoantennas. *Nano Letters*, 8(2), 631–636.

[Buonsanti et al., 2006] Buonsanti, R., Grillo, V., Carlino, E., Giannini, C., Curri, M. L., Innocenti, C., Sangregorio, C., Achterhold, K., Parak, F. G., Agostiano, A., & Cozzoli, P. D. (2006). Seeded growth of asymmetric binary nanocrystals made of a semiconductor tio2 rodlike section and a magnetic y-fe2o3 spherical domain. *Journal of the American Chemical Society*, 128(51), 16953.

[Burgin et al., 2008] Burgin, J., Liu, M. Z., & Guyot-Sionnest, P. (2008). Dielectric sensing with deposited gold bipyramids. *Journal of Physical Chemistry C*, 112(49), 19279–19282.

[Calza et al., 1997] Calza, P., Minero, C., & Pelizzetti, E. (1997). Photocatalytic transformations of chlorinated methanes in the presence of electron and hole scavengers. *Journal of the Chemical Society-Faraday Transactions*, 93(21), 3765–3771.

[Campion & Kambhampati, 1998] Campion, A. & Kambhampati, P. (1998). Surface-enhanced raman scattering. *Chemical Society Reviews*, 27(4), 241–250.

[Cao et al., 2009] Cao, M., Wang, M., & Gu, N. (2009). Optimized surface plasmon resonance sensitivity of gold nanoboxes for sensing applications. *Journal of Physical Chemistry C*, 113(4), 1217–1221.

[Carbone et al., 2009] Carbone, L., Jakab, A., Khalavka, Y., & Soennichsen, C. (2009). Light-controlled one-sided growth of large plasmonic gold domains on quantum rods observed on the single particle level. *NANO LETTERS*, 9(11), 3710–3714.

[Carbone et al., 2006] Carbone, L., Kudera, S., Giannini, C., Ciccarella, G., Cingolani, R., Cozzoli, P. D., & Manna, L. (2006). Selective reactions on the tips of colloidal semiconductor nanorods. *Journal of Materials Chemistry*, 16(40), 3952–3956.

[Carbone et al., 2007] Carbone, L., Nobile, C., DeGiorgi, M., Sala, F., Morello, G., Pompa, P., Hytch, M., Snoeck, E., Fiore, A., Franchini, I., Nadasan, M., Silvestre, A., Chiodo, L., Kudera, S., Cingolani, R., Krahne, R., & Manna, L. (2007). Synthesis and micrometer-scale assembly of colloidal cdse/cds nanorods prepared by a seeded growth approach. *Nano Lett.*, 7(10), 2942–2950.

[Casavola et al., 2007] Casavola, M., Grillo, V., Carlino, E., Giannini, C., Gozzo, F., Fernandez Pinel, E., Garcia, M. A., Manna, L., Cingolani, R., & Cozzoli, P. D. (2007). Topologically controlled growth of magnetic-metal-functionalized semiconductor oxide nanorods. *Nano Letters*, 7(5), 1386–1395.

[Cathcart et al., 2009] Cathcart, N., Frank, A. J., & Kitaev, V. (2009). Silver nanoparticles with planar twinned defects: effect of halides for precise tuning of plasmon resonance maxima from 400 to > 900 nm. *Chemical Communications*, (46), 7170–7172. Times Cited: 1 Cited Reference Count: 27 English Article CHEM COMMUN 521FY.

[Choi & Hoffmann, 1997] Choi, W. Y. & Hoffmann, M. R. (1997). Novel photocatalytic mechanisms for chcl3, chbr3, and ccl3co2- degradation and the fate of photogenerated trihalomethyl radicals on tio2. *Environmental Science & Technology*, 31(1), 89–95.

[Costi et al., 2008] Costi, R., Saunders, A. E., Elmalem, E., Salant, A., & Banin, U. (2008). Visible light-induced charge retention and photocatalysis with hybrid cdse-au nanodumbbells. *Nano Letters*, 8(2), 637–641.

[Cozzoli et al., 2004] Cozzoli, P. D., Comparelli, R., Fanizza, E., Curri, M. L., Agostiano, A., & Laub, D. (2004). Photocatalytic synthesis of silver nanoparticles stabilized by tio2 nanorods: A semiconductor/metal nanocomposite in homogeneous nonpolar solution. *Journal of the American Chemical Society*, 126(12), 3868–3879.

[Cozzoli et al., 2005] Cozzoli, P. D., Curri, M. L., & Agostiano, A. (2005). Efficient charge storage in photoexcited tio2 nanorod-noble metal nanoparticle composite systems. *Chemical Communications*, (25), 3186–3188.

[Dalpian & Chelikowsky, 2006] Dalpian, G. M. & Chelikowsky, J. R. (2006). Self-purification in semiconductor nanocrystals. *Physical Review Letters*, 96(22), 226802.

[de Abajo & Howie, 2002] de Abajo, F. J. G. & Howie, A. (2002). Retarded field calculation of electron energy loss in inhomogeneous dielectrics. *Physical Review B*, 65(11).

[DRAINE & FLATAU, 1994] DRAINE, B. & FLATAU, P. (1994). Discrete-dipole approximation for scattering calculations. *JOURNAL OF THE OPTICAL SOCIETY OF AMERICA A-OPTICS IMAGE SCIENCE AND VISION*, 11(4), 1491–1499.

[Ebbesen et al., 1998] Ebbesen, T., Lezec, H., Ghaemi, H., Thio, T., & Wolff, P. (1998). Extraordinary optical transmission through sub-wavelength hole arrays. *NATURE*, 391(6668), 667–669.

[Elghanian et al., 1997] Elghanian, R., Storhoff, J. J., Mucic, R. C., Letsinger, R. L., & Mirkin, C. A. (1997). Selective colorimetric detection of polynucleotides based on the distance-dependent optical properties of gold nanoparticles. *Science*, 277(5329), 1078–1081.

[Elmalem et al., 2008] Elmalem, E., Saunders, A. E., Costi, R., Salant, A., & Banin, U. (2008). Growth of photocatalytic cdse-pt nanorods and nanonets. *Advanced Materials*, 20(22), 4312–4317.

[Eustis & El-Sayed, 2006] Eustis, S. & El-Sayed, M. A. (2006). Why gold nanoparticles are more precious than pretty gold: Noble metal surface plasmon resonance and its enhancement of the radiative and nonradiative properties of nanocrystals of different shapes. *Chemical Society Reviews*, 35(3), 209–217.

[Fedutik et al., 2007] Fedutik, Y., Temnov, V., Woggon, U., Ustinovich, E., & Artemyev, M. (2007). Exciton-plasmon interaction in a composite metal-insulator-semiconductor nanowire system. *Journal of the American Chemical Society*, 129(48), 14939–14945.

[Figuerola et al., 2009] Figuerola, A., Franchini, I. R., Fiore, A., Mastria, R., Falqui, A., Bertoni, G., Bals, S., Van Tendeloo, G., Kudera, S., Cingolani, R., & Manna, L. (2009). End-to-end assembly of shape-controlled nanocrystals via a nanowelding approach mediated by gold domains. *Advanced Materials*, 21(5), 550–554.

[Freestone et al., 2007] Freestone, I., Meeks, N., Sax, M., & Higgitt, C. (2007). The lycurgus cup - a roman nanotechnology. *Gold Bulletin*, 40(4), 270–277.

[Funston et al., 2009] Funston, A. M., Novo, C., Davis, T. J., & Mulvaney, P. (2009). Plasmon coupling of gold nanorods at short distances and in different geometries. *NANO LETTERS*, 9(4), 1651–1658.

[Gomez et al., 2010] Gomez, D. E., Vernon, K. C., Mulvaney, P., & Davis, T. J. (2010). Surface plasmon mediated strong exciton-photon coupling in semiconductor nanocrystals. *NANO LETTERS*, 10(1), 274–278.

[Haes & Van Duyne, 2004] Haes, A. & Van Duyne, R. (2004). Preliminary studies and potential applications of localized surface plasmon resonance spectroscopy in medical diagnostics. *EXPERT REVIEW OF MOLECULAR DIAGNOSTICS*, 4(4), 527–537.

[Henkel et al., 2009] Henkel, A., Jakab, A., Brunklaus, G., & Soennichsen, C. (2009). Tuning plasmonic properties by alloying copper into gold nanorods. *JOURNAL OF PHYSICAL CHEMISTRY C*, 113(6), 2200–2204.

[Hirakawa & Kamat, 2004] Hirakawa, T. & Kamat, P. (2004). Photoinduced electron storage and surface plasmon modulation in ag@tio2 clusters. *Langmuir*, 20(14), 5645–5647.

[Hirsch et al., 2003] Hirsch, L. R., Stafford, R. J., Bankson, J. A., Sershen, S. R., Rivera, B., Price, R. E., Hazle, J. D., Halas, N. J., & West, J. L. (2003). Nanoshell-mediated near-infrared thermal therapy of tumors under magnetic resonance guidance. *Proceedings of the National Academy of Sciences of the United States of America*, 100(23), 13549–13554.

[Hohenester & Krenn, 2005] Hohenester, U. & Krenn, J. (2005). Surface plasmon resonances of single and coupled metallic nanoparticles: A boundary integral method approach. *Physical Review B*, 72(19).

[Homola et al., 1999] Homola, J., Yee, S. S., & Gauglitz, G. (1999). Surface plasmon resonance sensors: review. *Sensors and Actuators B-Chemical*, 54(1-2), 3–15.

[Hopkins & Barham, 1950] Hopkins, H. H. & Barham, P. M. (1950). The influence of the condenser on microscopic resolution. *Proceedings of the Physical Society. Section B*, 63(10), 737.

[Hu et al., 2001] Hu, J., Li, L., Yang, W., Manna, L., Wang, L., & Alivisatos, A. (2001). Linearly polarized emission from colloidal semiconductor quantum rods. *SCIENCE*, 292(5524), 2060–2063.

[Hu et al., 2008] Hu, M., Novo, C., Funston, A., Wang, H. N., Staleva, H., Zou, S. L., Mulvaney, P., Xia, Y. N., & Hartland, G. V. (2008). Dark-field microscopy studies of single metal nanoparticles: understanding the factors that influence the linewidth of the localized surface plasmon resonance. *Journal of Materials Chemistry*, 18(17), 1949–1960.

[Huang et al., 2009] Huang, C.-p., Yin, X.-g., Huang, H., & Zhu, Y.-y. (2009). Study of plasmon resonance in a gold nanorod with an lc circuit model. *OPTICS EXPRESS*, 17(8), 6407–6413.

[Huang et al., 2008] Huang, X. H., Jain, P. K., El-Sayed, I. H., & El-Sayed, M. A. (2008). Plasmonic photothermal therapy (pptt) using gold nanoparticles. *Lasers in Medical Science*, 23(3), 217–228.

[Jain & El-Sayed, 2008] Jain, P. K. & El-Sayed, M. A. (2008). Noble metal nanoparticle pairs: Effect of medium for enhanced nanosensing. *Nano Letters*, 8(12), 4347–4352. Times Cited: 33 Cited Reference Count: 58 English Article NANO LETT 382UK.

[Jain et al., 2007] Jain, P. K., Huang, W. Y., & El-Sayed, M. A. (2007). On the universal scaling behavior of the distance decay of plasmon coupling in metal nanoparticle pairs: A plasmon ruler equation. *Nano Letters*, 7(7), 2080–2088.

[Jana et al., 2001] Jana, N. R., Gearheart, L., & Murphy, C. J. (2001). Seed-mediated growth approach for shape-controlled synthesis of spheroidal and rod-like gold nanoparticles using a surfactant template. *Advanced Materials*, 13(18), 1389–1393.

[Jiang & Yu, 2008] Jiang, X. C. & Yu, A. B. (2008). Silver nanoplates: A highly sensitive material toward inorganic anions. *Langmuir*, 24(8), 4300–4309. Times Cited: 16 Cited Reference Count: 60 English Article LANGMUIR 283PB.

[Johnson & Christy, 1972] Johnson, P. B. & Christy, R. W. (1972). Optical-constants of noble-metals. *Physical Review B*, 6(12), 4370–4379.

[Kalkbrenner et al., 2004] Kalkbrenner, T., Hakanson, U., & Sandoghdar, V. (2004). Tomographic plasmon spectroscopy of a single gold nanoparticle. *NANO LETTERS*, 4(12), 2309–2314.

[Kasap & Capper, 2006] Kasap, S. & Capper, P. (2006). *Handbook of Electronic and Photonic Materials*. Springer Science+Media, Inc.

[Kelly et al., 2003] Kelly, K. L., Coronado, E., Zhao, L. L., & Schatz, G. C. (2003). The optical properties of metal nanoparticles: The influence of size, shape, and dielectric environment. *Journal of Physical Chemistry B*, 107(3), 668–677. Times Cited: 1541 Cited Reference Count: 64 English Article J PHYS CHEM B 638AE.

[Khalavka et al., 2009] Khalavka, Y., Becker, J., & Sönnichsen, C. (2009). Synthesis of rod-shaped gold nanorattles with improved plasmon sensitivity and catalytic activity. *Journal of the American Chemical Society*, 131(5), 1871–1875.

[Khalavka & Sönnichsen, 2008] Khalavka, Y. & Sönnichsen, C. (2008). Growth of gold tips onto hyperbranched cdte nanostructures. *Advanced Materials*, 20(3), 588.

[Klimov et al., 2000] Klimov, V., Mikhailovsky, A., Xu, S., Malko, A., Hollingsworth, J., Leatherdale, C., Eisler, H., & Bawendi, M. (2000). Optical gain and stimulated emission in nanocrystal quantum dots. *SCIENCE*, 290(5490), 314–317.

[Kneipp et al., 1997] Kneipp, K., Wang, Y., Kneipp, H., Perelman, L. T., Itzkan, I., Dasari, R., & Feld, M. S. (1997). Single molecule detection using surface-enhanced raman scattering (sers). *Physical Review Letters*, 78(9), 1667–1670.

[Kopitzki, 1993] Kopitzki, K. (1993). *Einführung in die Festkörperphysik*. Teubner, Stuttgart.

[Köster & Stahl, 1967] Köster, W. & Stahl, R. (1967). Über den einfluß von legierungsbildung, verformung und rekristallisation sowi von nah- und fernordnung auf optische konstanten der edelmetalle und ihrer legierungen. *Zeitschrift für Metallkunde*, 58, 768.

[Lambrecht et al., 2007] Lambrecht, A., Pirozhenko, I., Duraffourg, L., & Andreucci, P. (2007). The casimir effect for silicon and gold slabs. *Epl*, 77(4).

[Lee & El-Sayed, 2006] Lee, K. S. & El-Sayed, M. A. (2006). Gold and silver nanoparticles in sensing and imaging: Sensitivity of plasmon response to size, shape, and metal composition. *Journal of Physical Chemistry B*, 110(39), 19220–19225.

[Lide, 1993] Lide, D. (1993). *Handbook of chemistry and physics*. CRC Press.

[Lin et al., 2006] Lin, H. Y., Chen, Y. F., Wu, J. G., Wang, D. I., & Chen, C. C. (2006). Carrier transfer induced photoluminescence change in metal-semiconductor core-shell nanostructures. *Applied Physics Letters*, 88(16).

[Linde & J.O., 1936] Linde, C. J. & J.O. (1936). Röntgenographische uns elektrische untersuchungen des cuau-systems. *Annalen Der Physik*, 25(1), 1–48.

[Link et al., 2005] Link, S., El-Sayed, M., & Mohamed, M. (2005). Simulation of the optical absorption spectra of gold nanorods as a function of their aspect ratio and the effect of the medium dielectric constant (vol 103b, pg 3073, 1999). *JOURNAL OF PHYSICAL CHEMISTRY B*, 109(20), 10531–10532.

[Lithography, 2010] Lithography (NaturePublishing2010). Lithography roadmap on track. *Nature Publishing Group*, 4, 20.

[Liu & Alivisatos, 2004] Liu, H. & Alivisatos, A. P. (2004). Preparation of asymmetric nanostructures through site selective modification of tetrapods doi:10.1021/nl048523i. *Nano Letters*, 4(12), 2397–2401.

[Liu & Guyot-Sionnest, 2004] Liu, M. Z. & Guyot-Sionnest, P. (2004). Synthesis and optical characterization of au/ag core/shell nanorods. *Journal of Physical Chemistry B*, 108(19), 5882–5888.

[Liu et al., 2009] Liu, N., Weiss, T., Mesch, M., Langguth, L., Eigenthaler, U., Hirscher, M., Sönnichsen, C., & Giessen, H. (2009). Planar metamaterial analogue of electromagnetically induced transparency for plasmonic sensing. *Nano Letters*.

[Liz-Marzan, 2006] Liz-Marzan, L. M. (2006). Tailoring surface plasmons through the morphology and assembly of metal nanoparticles. *Langmuir*, 22(1), 32–41. Times Cited: 298 Cited Reference Count: 111 English Review LANGMUIR 999SH.

[Lukas Novotny, 2007] Lukas Novotny, B. H. (2007). *Principles of Nano-Optics*. Cambridge University Press.

[Mahmoud & El-Sayed, 2010] Mahmoud, M. A. & El-Sayed, M. A. (2010). Gold nanoframes: Very high surface plasmon fields and excellent near-infrared sensors. *Journal of the American Chemical Society*, 132(36), 12704–12710. Times Cited: 0 Cited Reference Count: 42 English Article J AM CHEM SOC 653FP.

[Maier et al., 2001] Maier, S. A., Brongersman, M. L., Kik, P. G., Meltzer, S., Requicha, A. A. G., & Atwater, H. A. (2001). Plasmonics - a route to nanoscale optical devices. *Advanced Materials*, 13(19), 1501–1505.

[Malinsky et al., 2001] Malinsky, M. D., Kelly, K. L., Schatz, G. C., & Van Duyne, R. P. (2001). Nanosphere lithography: Effect of substrate on the localized surface plasmon resonance spectrum of silver nanoparticles. *Journal of Physical Chemistry B*, 105(12), 2343–2350. Times Cited: 146 Cited Reference Count: 39 English Article J PHYS CHEM B 416CW.

[MANSFIELD & KINO, 1990] MANSFIELD, S. & KINO, G. (1990). Solid immersion microscope. *APPLIED PHYSICS LETTERS*, 57(24), 2615–2616.

[Mayer et al., 2010] Mayer, K. M., Hao, F., Lee, S., Nordlander, P., & Hafner, J. H. (2010). A single molecule immunoassay by localized surface plasmon resonance. *Nanotechnology*, 21(25). Times Cited: 3 Cited Reference Count: 28 English Article NANOTECHNOL 605AP.

[McFarland & Van Duyne, 2003] McFarland, A. D. & Van Duyne, R. P. (2003). Single silver nanoparticles as real-time optical sensors with zeptomole sensitivity. *Nano Letters*, 3(8), 1057–1062.

[Medintz et al., 2003] Medintz, I., Clapp, A., Mattoussi, H., Goldman, E., Fisher, B., & Mauro, J. (2003). Self-assembled nanoscale biosensors based on quantum dot fret donors. *NATURE MATERIALS*, 2(9), 630–638.

[MEIER & WOKAUN, 1983] MEIER, M. & WOKAUN, A. (1983). Enhanced fields on large metal particles - dynamic depolarization. *OPTICS LETTERS*, 8(11), 581–583.

[Menagen et al., 2009] Menagen, G., Shemesh, Y., Macdonald, J. E., Popov, I., & Banin, U. (2009). Au growth on cds nanorods; photo-induced versus thermal growth mechanisms. *submitted to J.Chem.Mat.*

[Michler et al., 2000] Michler, P., Imamoglu, A., Mason, M., Carson, P., Strouse, G., & Buratto, S. (2000). Quantum correlation among photons from a single quantum dot at room temperature. *NATURE*, 406(6799), 968–970.

[Miller & Lazarides, 2005] Miller, M. & Lazarides, A. (2005). Sensitivity of metal nanoparticle surface plasmon resonance to the dielectric environment. *JOURNAL OF PHYSICAL CHEMISTRY B*, 109(46), 21556–21565.

[Mokari et al., 2006] Mokari, T., Costi, R., Sztrum, C. G., Rabani, E., & Banin, U. (2006). Formation of symmetric and asymmetric metal-semiconductor hybrid nanoparticles. *physica status solidi (b)*, 243(15), 3952–3958.

[Mokari et al., 2004] Mokari, T., Rothenberg, E., Popov, I., Costi, R., & Banin, U. (2004). Selective growth of metal tips onto semiconductor quantum rods and tetrapods. *Science*, 304(5678), 1787–1790.

[Mokari et al., 2005] Mokari, T., Sztrum, C. G., Salant, A., Rabani, E., & Banin, U. (2005). Formation of asymmetric one-sided metal-tipped semiconductor nanocrystal dots and rods. *Nature Materials*, 4(11), 855–863.

[Muller et al., 2005] Muller, J., Lupton, J., Lagoudakis, P., Schindler, F., Koeppe, R., Rogach, A., Feldmann, J., Talapin, D., & Weller, H. (2005). Wave function engineering in elongated semiconductor nanocrystals with heterogeneous carrier confinement. *NANO LETTERS*, 5(10), 2044–2049.

[Muller et al., 2002] Muller, J., Sonnichsen, C., von Poschinger, H., von Plessen, G., Klar, T., & Feldmann, J. (2002). Electrically controlled light scattering with single metal nanoparticles. *APPLIED PHYSICS LETTERS*, 81(1), 171–173.

[Mulvaney, 1996] Mulvaney, P. (1996). Surface plasmon spectroscopy of nanosized metal particles. *Langmuir*, 12(3), 788–800.

[Mulvaney et al., 2006] Mulvaney, P., Perez-Juste, J., Giersig, M., Liz-Marzan, L. M., & Pecharroman, C. (2006). Drastic surface plasmon mode shifts in gold nanorods due to electron charging. *Plasmonics*, 1(1), 61.

[Murphy et al., 2008] Murphy, C. J., Gole, A. M., Hunyadi, S. E., Stone, J. W., Sisco, P. N., Alkilany, A., Kinard, B. E., & Hankins, P. (2008). Chemical sensing and imaging with metallic nanorods. *Chemical Communications*, (5), 544–557.

[Ni et al., 2008] Ni, W., Kou, X., Yang, Z., & Wang, J. (2008). Tailoring longitudinal surface plasmon wavelengths, scattering and absorption cross sections of gold nanorods. *ACS NANO*, 2(4), 677–686.

[Nie & Emory, 1997] Nie, S. & Emory, S. R. (1997). Probing single molecules and single nanoparticles by surface-enhanced raman scattering. *Science*, 275, 1102–1106.

[Nikolajsen et al., 2004] Nikolajsen, T., Leosson, K., & Bozhevolnyi, S. (2004). Surface plasmon polariton based modulators and switches operating at telecom wavelengths. *APPLIED PHYSICS LETTERS*, 85(24), 5833–5835.

[Nikoobakht & El-Sayed, 2003] Nikoobakht, B. & El-Sayed, M. A. (2003). Preparation and growth mechanism of gold nanorods (nrs) using seed-mediated growth method. *Chemistry of Materials*, 15(10), 1957–1962.

[Nirmal et al., 1996] Nirmal, M., Dabbousi, B., Bawendi, M., Macklin, J., Trautman, J., Harris, T., & Brus, L. (1996). Fluorescence intermittency in single cadmium selenide nanocrystals. *NATURE*, 383(6603), 802–804.

[Norris et al., 2008] Norris, D. J., Efros, A. L., & Erwin, S. C. (2008). Doped nanocrystals. *Science*, 319(5871), 1776–1779.

[Novo et al., 2008] Novo, C., Funston, A. M., & Mulvaney, P. (2008). Direct observation of chemical reactions on single gold nanocrystals using surface plasmon spectroscopy. *Nature Nanotechnology*, 3(10), 598–602.

[Osborn, 1945] Osborn, J. A. (1945). Demagnetizing factors of the general ellipsoid. *Physical Review*, 67(11-1), 351–357.

[O'Sullivan et al., 2008] O'Sullivan, C., Ahmed, S., & Ryan, K. M. (2008). Gold tip formation on perpendicularly aligned semiconductor nanorod assemblies. *Journal of Materials Chemistry*, 18(43), 5218.

[Otte et al., 2010] Otte, M. A., Sepulveda, B., Ni, W., Perez Juste, J., Liz-Marzan, L. M., & Lechuga, L. M. (2010). Identification of the optimal spectral region for plasmonic and nanoplasmonic sensing. *ACS NANO*, 4(1), 349–357.

[Pacifici et al., 2007] Pacifici, D., Lezec, H. J., & Atwater, H. A. (2007). All-optical modulation by plasmonic excitation of cdse quantum dots. *NATURE PHOTONICS*, 1(7), 402–406.

[Pala et al., 2008] Pala, R. A., Shimizu, K. T., Melosh, N. A., & Brongersma, M. L. (2008). A nonvolatile plasmonic switch employing photochromic molecules. *NANO LETTERS*, 8(5), 1506–1510.

[Pazos-Perez et al., 2007] Pazos-Perez, N., Gao, Y., Hilgendorff, M., Irsen, S., Perez-Juste, J., Spasova, M., Farle, M., Liz-Marzan, L. M., & Giersig, M. (2007). Magnetic-noble metal nanocomposites with morphology-dependent optical response. *Chemistry of Materials*, 19(18), 4415–4422.

[Pendry, 2000] Pendry, J. (2000). Negative refraction makes a perfect lens. *PHYSICAL REVIEW LETTERS*, 85(18), 3966–3969.

[Peng et al., 1997] Peng, X., Schlamp, M. C., Kadavanich, A. V., & Alivisatos, A. P. (1997). Epitaxial growth of highly luminescent cdse/cds core/shell nanocrystals with photostability and electronic accessibility. *Journal of the American Chemical Society*, 119(30), 7019–7029.

[Peng et al., 1998] Peng, X., Wickham, J., & Alivisatos, A. (1998). Kinetics of ii-vi and iii-v colloidal semiconductor nanocrystal growth: "focusing" of size distributions. *Journal of the American Chemical Society*, 120, 5343–5344.

[Perez-Juste et al., 2005] Perez-Juste, J., Pastoriza-Santos, I., Liz-Marzan, L. M., & Mulvaney, P. (2005). Gold nanorods: Synthesis, characterization and applications. *Coordination Chemistry Reviews*, 249(17-18), 1870–1901.

[Phala & van Steen, 2007] Phala, N. S. & van Steen, E. (2007). Intrinsic reactivity of gold nanoparticles: Classical, semi-empirical and dft studies. *Gold Bulletin*, 40(2), 150–153.

[Pierrat et al., 2009] Pierrat, S., Hartinger, E., Faiss, S., Janshoff, A., & Sonnichsen, C. (2009). Rotational dynamics of laterally frozen nanoparticles specifically attached to biomembranes. *Journal of Physical Chemistry C*, 113(26), 11179–11183.

[Pierrat et al., 2007] Pierrat, S., Zins, I., Breivogel, A., & Sonnichsen, C. (2007). Self-assembly of small gold colloids with functionalized gold nanorods. *Nano Letters*, 7(2), 259–263.

[Pietrobon et al., 2009] Pietrobon, B., McEachran, M., & Kitaev, V. (2009). Synthesis of size-controlled faceted pentagonal silver nanorrods with tunable plasmonic properties and self-assembly of these nanorods. *Acs Nano*, 3(1), 21–26. Times Cited: 18 Cited Reference Count: 35 English Article ACS NANO 401PH.

[Pinchuk et al., 2004] Pinchuk, A., von Plessen, G., & Kreibig, U. (2004). Influence of interband electronic transitions on the optical absorption in metallic nanoparticles. *Journal of Physics D-Applied Physics*, 37(22), 3133–3139.

[Prescott & Mulvaney, 2006] Prescott, S. W. & Mulvaney, P. (2006). Gold nanorod extinction spectra. *Journal of Applied Physics*, 99(12).

[Prescott & Mulvaney, 2008] Prescott, S. W. & Mulvaney, P. (2008). Gold nanorod extinction spectra (vol 99, art no 1235047, 2006). *Journal of Applied Physics*, 103(11), 123504.

[Quinten et al., 1998] Quinten, M., Leitner, A., Krenn, J. R., & Aussenegg, F. R. (1998). Electromagnetic energy transport via linear chains of silver nanoparticles. *Optics Letters*, 23(17), 1331–1333.

[Raschke et al., 2003] Raschke, G., Kowarik, S., Franzl, T., Sönnichsen, C., Klar, T. A., Feldmann, J., Nichtl, A., & Kurzinger, K. (2003). Biomolecular recognition based on single gold nanoparticle light scattering. *Nano Letters*, 3(7), 935–938.

[Reiss, 1951] Reiss, H. (1951). The growth of uniform colloidal dispersions. *Journal of Chemical Physics*, 19(4), 482–487.

[Ringe et al., 2010] Ringe, E., McMahon, J. M., Sohn, K., Cobley, C., Xia, Y. N., Huang, J. X., Schatz, G. C., Marks, L. D., & Van Duyne, R. P. (2010). Unraveling the effects of size, composition, and substrate on the localized surface plasmon resonance frequencies of gold and silver

nanocubes: A systematic single-particle approach. *Journal of Physical Chemistry C*, 114(29), 12511–12516. Times Cited: 0 Cited Reference Count: 38 English Article J PHYS CHEM C 627VE.

[Salant et al., 2006] Salant, A., Amitay-Sadovsky, E., & Banin, U. (2006). Directed self-assembly of gold-tipped cdse nanorods. *Journal of the American Chemical Society*, 128(31), 10006.

[Saunders et al., 2006] Saunders, A., Popov, I., & Banin, U. (2006). Synthesis of hybrid cds-au colloidal nanostructures. *J. Phys. Chem. B*, 110(50), 25421–25429.

[Schaak et al., 2005] Schaak, R. E., Sra, A. K., Leonard, B. M., Cable, R. E., Bauer, J. C., Han, Y. F., Means, J., Teizer, W., Vasquez, Y., & Funck, E. S. (2005). Metallurgy in a beaker: Nanoparticle toolkit for the rapid low-temperature solution synthesis of functional multimetallic solid-state materials. *Journal of the American Chemical Society*, 127(10), 3506–3515.

[Schubert et al., 2008] Schubert, O., Becker, J., Carbone, L., Khalavka, Y., Provalska, T., Zins, I., & Sönnichsen, C. (2008). Mapping the polarization pattern of plasmon modes reveals nanoparticle symmetry. *Nano Letters*, 8(8), 2345–2350.

[Schultz et al., 2000] Schultz, S., Smith, D. R., Mock, J. J., & Schultz, D. A. (2000). Single-target molecule detection with nonbleaching multicolor optical immunolabels. *Proceedings of the National Academy of Sciences of the United States of America*, 97(3), 996–1001.

[Sherry et al., 2005] Sherry, L. J., Chang, S. H., Schatz, G. C., Van Duyne, R. P., Wiley, B. J., & Xia, Y. N. (2005). Localized surface plasmon resonance spectroscopy of single silver nanocubes. *Nano Letters*, 5(10), 2034–2038.

[Shieh et al., 2005] Shieh, F., Saunders, A. E., & Korgel, B. A. (2005). General shape control of colloidal cds, cdse, cdte quantum rods and quantum rod heterostructures. *The Journal of Physical Chemistry B*, 109(18), 8538–8542.

[Slaughter et al., 2010] Slaughter, L. S., Wu, Y., Willingham, B. A., Nordlander, P., & Link, S. (2010). Effects of symmetry breaking and conductive contact on the plasmon coupling in gold nanorod dimers. *ACS NANO*, 4(8), 4657–4666.

[Sönnichsen, 2001] Sönnichsen, C. (2001). *Plasmons in metal nanostructures*. München: Cuvillier Verlag Göttingen.

[Sönnichsen & Alivisatos, 2005] Sönnichsen, C. & Alivisatos, A. P. (2005). Gold nanorods as novel non-bleaching plasmon based orientation sensors. *Biophysical Journal*, 88(1), 364A–365A.

[Sönnichsen et al., 2002] Sönnichsen, C., Franzl, T., Wilk, T., von Plessen, G., Feldmann, J., Wilson, O., & Mulvaney, P. (2002). Drastic reduction of plasmon damping in gold nanorods. *Physical Review Letters*, 88(7), 077402.

[Sönnichsen et al., 2000] Sönnichsen, C., Geier, S., Hecker, N. E., von Plessen, G., Feldmann, J., Ditlbacher, H., Lamprecht, B., Krenn, J. R., Aussenegg, F. R., Chan, V. Z. H., Spatz, J. P., & Moller, M. (2000). Spectroscopy of single metallic nanoparticles using total internal reflection microscopy. *Applied Physics Letters*, 77(19), 2949–2951.

[Sra et al., 2005] Sra, A. K., Ewers, T. D., & Schaak, R. E. (2005). Direct solution synthesis of intermetallic aucu and aucu3 nanocrystals and nanowire networks. *Chemistry of Materials*, 17(4), 758–766.

[Sra & Schaak, 2004] Sra, A. K. & Schaak, R. E. (2004). Synthesis of atomically ordered aucu and aucu3 nanocrystals from bimetallic nanoparticle precursors. *Journal of the American Chemical Society*, 126(21), 6667–6672.

[Subramanian et al., 2004] Subramanian, V., Wolf, E., & Kamat, P. (2004). Catalysis with tio2/gold nanocomposites. effect of metal particle size on the fermi level equilibration. *J. Am. Chem. Soc.*, 126(15), 4943–4950.

[Tang et al., 2006] Tang, D., Yuan, R., & Chai, Y. (2006). Ligand-functionalized core/shell ag@au nanoparticles label-free amperometric immun-biosensor. *Biotechnology and Bioengineering*, 94(5), 996–1004.

[The LyX Team, 2009] The LyX Team (2009). LyX 1.6.1 - The Document Processor [Computer software and manual]. Internet: http://www.lyx.org. Retrieved February 16, 2009, from http://www.lyx.org.

[Tsuji et al., 2006] Tsuji, M., Miyamae, N., Lim, S., Kimura, K., Zhang, X., Hikino, S., & Nishio, M. (2006). Crystal structures and growth mechanisms of au@ag core-shell nanoparticles prepared by the microwave-polyol method. *Crystal Growth & Design*, 6(8), 1801–1807.

[Unger & Kreiter, 2009] Unger, A. & Kreiter, M. (2009). Analyzing the performance of plasmonic resonators for dielectric sensing. *Journal of Physical Chemistry C*, 113(28), 12243–12251. Times Cited: 4 Cited Reference Count: 27 English Article J PHYS CHEM C 472NT.

[Villars et al., 1985] Villars, P., Calvert, L. D., & Pearson, W. B. (1985). *Pearson's handbook of crystallographic data for intermetallic phases*. Metals Park, Oh: American Society for Metals.

[Wang & Reinhard, 2009] Wang, H. Y. & Reinhard, B. M. (2009). Monitoring simultaneous distance and orientation changes in discrete dimers of dna linked gold nanoparticles. *Journal of Physical Chemistry C*, 113(26), 11215–11222.

[Wang & Pedersen, 2009] Wang, S. L. & Pedersen, D. B. (2009). Effect of medium for enhanced nanosensing: Dda theory vs experimental studies of ag nanoparticle assemblies. *Journal of Physical Chemistry C*, 114(7), 2861–2866. Times Cited: 0.

[Wang et al., 2005] Wang, X., Zhang, Z. Y., & Hartland, G. V. (2005). Electronic dephasing in bimetallic gold-silver nanoparticles examined by single particle spectroscopy. *Journal of Physical Chemistry B*, 109(43), 20324–20330.

[Wei et al., 2010] Wei, H., Reyes-Coronado, A., Nordlander, P., Aizpurua, J., & Xu, H. X. (2010). Multipolar plasmon resonances in individual ag nanorice. *Acs Nano*, 4(5), 2649–2654. Times Cited: 2 Cited Reference Count: 40 English Article ACS NANO 600HU.

[Weissleder, 2001] Weissleder, R. (2001). A clearer vision for in vivo imaging. *Nat Biotech*, 19(4), 316–317.

[Wood et al., 2001] Wood, A., Giersig, M., & Mulvaney, P. (2001). Fermi level equilibration in quantum dot-metal nanojunctions. *The Journal of Physical Chemistry B*, 105(37), 8810–8815.

[Wu & Xu, 2009] Wu, C. L. & Xu, Q. H. (2009). Stable and functionable mesoporous silica-coated gold nanorods as sensitive localized surface plasmon resonance (lspr) nanosensors. *Langmuir*, 25(16), 9441–9446. Times Cited: 11 Cited Reference Count: 37 English Article LANGMUIR 480GG.

[Yang, 2006] Yang, H. (2006). Growth of au nanocrystals on cds nanorods. *Metals and Materials International*, 12(4), 351–355.

[YEE, 1966] YEE, K. (1966). Numerical solution of initial boundary value problems involving maxwells equations in isotropic media. *IEEE TRANSACTIONS ON ANTENNAS AND PROPAGATION*, AP14(3), 302–&.

[Yin & Alivisatos, 2005] Yin, Y. & Alivisatos, A. P. (2005). Colloidal nanocrystal synthesis and the organic-inorganic interface. *Nature*, 437, 664–670.

[Zeman & Schatz, 1987] Zeman, E. J. & Schatz, G. C. (1987). An accurate electromagnetic theory study of surface enhancement factors for silver, gold, copper, lithium, sodium, aluminum, gallium, indium, zinc, and cadmium. *The Journal of Physical Chemistry*, 91(3), 634–643.